Université du Québec
Institut National de la Recherche Scientifique
Centre Énergie, Matériaux Télécommunications

Growth, Optimization and Characterization of co-substituted Cerium and Bismuth Garnet films for Integrated Magneto-optical Applications

By

Chandra Sekhar Manda

Thesis submitted in partial fulfillment of the requirements for the degree of
Master of Science

Evaluation Jury

Examinateur interne (et président du jury)	Prof. Guy G. Ross INRS-Énergie, Matériaux Télécommunications
Examinateur externe	Prof. G. Mohan Rao Indian Institute of Science, India
Directeur de recherche	Prof. A. Pignolet INRS-Énergie, Matériaux Télécommunications
Co-directeur de recherche	Prof. R. Morandotti INRS-Énergie, Matériaux Télécommunications

This page is left blank

This page is left blank

Contents

Dedication

To my family, Chinmayi (daughter), Pramatt (son), and Mamatha (wife) for their love and support

Abstract

The miniaturization of device dimensions is essential to the development of a new generation of ultra-comprehensive integrated optoelectronic circuits (ICs) that are based on magneto-optical (MO) materials. Epitaxial films of bismuth substituted iron garnets are among the most promising materials for the realization of such devices, thanks to their very high Faraday Rotation (FR). Garnet films have a wide operation frequency range in both the visible and infrared wavelengths making them ideal in many applications.

The idea explored in the present work is to combine the improved magneto-optic properties induced by Cerium substitution in YIG with the structural stability granted by the ions of Bismuth when substituting for Yttrium, preventing the structural instability usually associated with high Ce doping levels. In view of future integration, the new remarkable material to be developed has to be also compatible with standard thin film technology.

In this investigation, high-quality $Ce_{2.2}Bi_{0.8}Fe_5O_{12}$ (CeBiIG) films, whose composition was selected to produce the highest MO response at communication wavelengths, were synthesized. High-quality $Ce_{2.2}Bi_{0.8}Fe_5O_{12}$ films were grown by Pulsed Laser Deposition (PLD) on paramagnetic substrates of Gadolinium Gallium Garnet (GGG). Various growth parameters of the films were evaluated, including modification of the atmospheric conditions such as oxygen, argon, and a mixture of argon and hydrogen, in order to optimize the quality of the deposited films. The optimal deposition conditions were established. In particular, the best thin films were produced in an argon atmosphere.

The CeBiIG films deposited on (111) –oriented GGG substrates and treated in an argon atmosphere exhibits narrow mosaicity, suggest a good crystalline quality. In addition, morphological studies show a low roughness values within the range of 0.8-2 nm. Despite the volatile nature of the bismuth constituent in the grown films, the correct Bi composition has been confirmed by X-ray photoelectron spectroscopy (XPS). The Faraday rotation (FR) and the influence of film thickness on the performance of CeBiIG

magneto optical films have been studied. A value of the FR of 0.55 degrees/μm at a wavelength of 1.5 μm has been reached, which is comparably higher than the FR values measured for other garnet films. The increased Faraday rotation coefficient in these films is most probably the result of the Bismuth ion doping into the dodecahedral sites of the CeBiIG garnet. In addition, these excellent MO film properties can be reproduced under the optimized conditions established.

Acknowledgements

My work at the Institut National de la Recherche Scientifique, Énergie Matériaux and Télécommunications (INRS-EMT), Varennes, would not have been possible without the support of my academic advisers, Prof. Alain Pignolet and Prof. Roberto Morandotti. I would like to thank the Magneto-optical group, including Marcello Ferrera, Dr. Luca Razzari, Dr. M. Zaezjev, Dr. Marco Peccianti, as well as Dr. Catalin Harnagea, for their help. I particularly appreciated Marcello for engaging me in meaningful and beneficial discussions. This work would also not have been feasible without support from a NSERC (Natural Sciences and Engineering Research Council of Canada) fellowship.

The proposed CeBiIG compositions were sent to Praxair for the fabrication of PLD targets with the desired composition. Thanks to PRAXAIR, USA, for delivering the targets in a timely fashion.

I would like to express my sincere thanks to Prof. Guy G. Ross, for his useful suggestions about the course work on RBS analysis; to Prof. R. Paynter, for discussions on XPS measurements, and to Prof. M. Chaker, for discussions on course work (PLD).

The surface characterization was done with the substantial collaboration of members of the Western University.

I would like to thank Prof. Francois Vidal, for suggesting effective course work and Prof. T. Ozaki for his valuable advice.

I wish to recognize the indispensable support of Gargi, KP, Francisco, David, Shalaby, and Dr. Alessia whose sense of humor kept me in good spirits. I would like to thank my friends, colleagues, and collaborators from the University of Montreal and Sherbrooke for assisting me at various stages of my life in Canada.

Also, I would like to acknowledge Professors Morandotti and Chaker, for obtaining a grant to purchase the magnet used to measure Faraday rotation, and a special thank goes to Brian Richter and his associates at GMW-USA for their timely delivery of the magnet and useful tips. I would like to thank Christophe Chabanier, for helpful discussions about some of the techniques used in the project.

I would like to thank the jury, Prof. Guy G. Ross (INRS-EMT), Prof Mohan Rao, Indian Institute of science for accepting to evaluate my thesis and for their useful comments.

I would like to thank Professors C.N.R. Rao, FRS and S.B. Krupanidhi (IISc) for introducing me to thin films and Prof.S.V.Suryanarayana for bulk (doctoral program-OU) research.

I have an unflinching faith in the Almighty and will continue my journey in science with confidence. Finally, I must acknowledge my children Chinmayi, Pramatt, and my wife Mamatha who were always there to provide unconditional love, care, and support. I also acknowledge Dr. Sai Pinnepalli, Louisiana State University, USA for his feedback during the final review of my thesis.

Publications & conferences

1. M. Chandra Sekhar, J. Y, Hwang, M. Ferrera, M. Zaezjev, L. Razzari, Y. Linzon, A. Pignolet, and R. Morandotti, Strong enhancement of the Faraday rotation in Ce and Bi modified epitaxial iron garnet thin films, Appl. Phy. Lett. 94, 181916, (2009).

2. M. Ferrera, M. Chandra Sekhar, J. Y. Hwang, L. Razzari, C. Harnagea, M. Zaezjev, Y. Linzon, A. Pignolet, and R. Morandotti, Conference on Lasers and Electro-Optics/International Quantum Electronics Conference, OSA Technical Digest (CD) (Optical Society of America, 2009), paper CTuEE2.

3. M. Ferrera, M. Chandra Sekhar, J. Y. Hwang, L. Razzari, C. Harnagea, M. Zaezjev, Y. Linzon, A. Pignolet and R. Morandotti, Large Faraday Effect in Ce:BiIG Epitaxial Thin Films, IEEE photonics society, Belek-Antalia, 22nd annual meeting, Oral presentation+proceeding (2009).

4. M. Chandra Sekhar, M. Zaezjev, M. Ferrera, L. Razzari, A. Pignolet and R. Morandotti, Fabrication and structural investigation of CeBiIG epitaxial thin films for Magneto-optical Application by Pulsed laser deposition, Materials Research Society Symposium Boston MA, USA, (2008). Oral presentation.

5. M. Zaezjev, M. Chandra Sekhar, M. Ferrera, L. Razzari, A. Pignolet, R. Morandotti, B. M. Holmes, M. Sorel, D.C. Hutchings, Effects of the foreign phases on the crystallization and growth of magneto optic garnets films, conference on Lasers and Electro-Optics, conference on Quantum Electronics and Laser Science, CLEO/QELS, San Jose, California (2008).

6. M. Zaezjev, M. Chandra Sekhar, M. Ferrera, L. Razzari, A. Pignolet, R. Morandotti, B. M. Holmes, M. Sorel and D. C. Hutchings, Effect of the Foreign Phases on the crystallization and Growth of Magnetooptic garnet Films, in conference on Lasers and Electro-Optics/Quantum Electronics and Laser science Conference and Photonic Applications Systems Technologies, OSA technical digest (CD) (optical Society of America, 2008) paper CThM5.
   http://www.opticsinfobase.org/abstract.cfm?URI=CLEO-2008-CThM5

7. M. Zaezjev, M. Chandra Sekhar, M. Ferrera, L. Razzari, B. M. Holmes, M. Sorel, D.C. Hutchings, A. Pignolet, and R. Morandotti, Crystallization of yttrium –iron garnet (YIG) in thin films: nucleation and growth aspect, in Proceedings of Materials and Hyperintegration Challenges in Next-Generation Interconnect technology, MRS proceedings 1036-M04-19 (2007).

8. M. Chandra Sekhar, M. Zaezjev, M. Ferrera, L.Razzari, R. Morandotti, Growth and structure of CeBIG thin films for Magneto Optical Applications, 19th Canadian Materials Science Conference, McMaster University, Hamilton, Canada (2007). Oral presentation.

9. M. Zaezjev, M. Chandra Sekhar, M. Ferrera, L. Razzari, G.G. Ross, B. M. Holmes, M. Sorel, D. C. Hutchings, S. Roorda, and R. Morandotti, Magneto-optic iron-garnet thin films for integrated optical applications" SPIE Newsroom (2007), on-line publication http://spie.org/documents/Newsroom/Imported/513/2007010513.pdf

10. M. Chandra Sekhar, M. Zaezjev, M. Ferrera, L. Razzari, R. Morandotti, Croissance et propriétés structurales de couches minces épitaxiales du nouveau matériau Ce-BiIG pour des applications magnéto-optiques, 75^{e} congres de l'ACFAS, Université du Québec, Trois rivières, Québec, Canada (2007), Poster Présentation.

11. Michael Zaezjev, M. Chandra Sekhar, M. Ferrera, L. Razzari, G. G. Ross, B. M. Holmes, M. Sorel, D.C. Hutchings, S. Roorda and R. Morandotti, Oxygen Effect on the Pulsed Laser Déposition and Post-déposition Heat Treatment for Yttrium Iron Garnet Thin Films, Symposium M: Materials and Hyper integration Challenges in Next-Generation Interconnect Technology, Boston, USA (2007), Oral présentation.

12. M. Zaezjev, M. Chandra Sekhar, M. Ferrera, L. Razzari, G. G. Ross, B. M. Holmes, M. Sorel, D.C. Hutchings, S. Roorda, and R. Morandotti, Fabrication of YIG thin films for Magneto-optical applications, Optical Design & Engineering, SPIE (2007) proceeding.

13. M. Zaezjev, M. Chandra Sekhar, M. Ferrera, L. Razzari, G. G. Ross, B. M. Holmes, M. Sorel, D. C. Hutchings, S. Roorda, and R. Morandotti, Magneto optic iron garnet thin films for integrated optical applications; International conference on applications of photonic technology, No 8, 1981, vol. 6343 (2), 63433W, Canada (2006).

14. M. Zaezjev, M. Chandra Sekhar, M. Ferrera, L. Razzari, R. Morandotti, B. M. Holmes, M. Sore, D. C. Hutchings, and S. Roorda, Magnetoptic garnets - possible solution for integrated full-optical circuits, 18th Canadian Materials Science meeting at McGill, Montreal (2006). Oral presentation.

Figure Captions

Préface

This document summarizes the research activities carried out during my master's programme at INRS-EMT. The magneto optical investigation of a new compound ($Ce_{2.2}Bi_{0.8}Fe_5O_{12}$), synthesized for the first time in the Ultrafast Optical Processing (UOP) group at INRS-EMT Varennes is presented. This compound belongs to the class of iron garnets, which are well known for such properties as a strong Faraday response, low optical losses in the near infra-red, and ease of fabrication. For these reasons iron garnets are the first-choice materials for the fabrication of today's bulk optical isolators. In this thesis, we describe the PLD deposition conditions needed for the fabrication of CeBiIG thin films, and the techniques used for their characterization, including their magneto optical properties.

Introduction

One of the greatest technological innovations of the twentieth century was the development of electronic integrated circuits (IC). Immediately after the first integrated silicon chip developed by Jack Kilby of Texas Instruments Laboratory in 1958, the benefits of this revolutionary technology to the electronics industry has been apparent, and the silicon technology has produced one of the fastest growing markets. The enormous growth of the electronics industry was predicted by Gordon E. Moore in 1965. Moore predicted a doubling of the empirical density of transistors on a chip every two years and he believed that this trend would last at least a decade [1].

Moore's law is accurate even today, with the annual production of transistors exceeding the total number of transistors built so far and only the physical limitations imposed by the electron-electron interactions at subnanometer level may prove to be the ceiling for Moore's law [2].

Optics is a promising alternative to electronics to process and especially to transmit information that offers flexibility and compatibility with silicon technology, especially in telecommunication networks. However, today's silicon technology is still able to provide the same benefits as optics at lower cost. Although optoelectronics has

recently become reality, "all-optical" technology is expensive, complicated and provides limited functionality. Despite ICs being cost-effective and efficient to process information, there is a rapid growth in the development of optical telecommunications networks. Over the past 30 years, conventional copper wires are replaced by more efficient optical fibers, particularly for long-distance communications. Today, optical networks are efficiently used in the telephone industry, cable TV services and provide the foundation for many other networks [3].

This preeminence of the optical transmission of information in communication systems is primarily due to the benefits of optical communications over their electrical counterparts. Fiber optic systems' operational bandwidth is much higher than that of copper cables and the optical signal can be transmitted over hundreds of kilometers without significant attenuation.

The transition from electronic to photonic technology will be governed by various factors such as the need for more reliable and faster data transmission, the various technologies available, and the development of solution such as photonic integrated circuits (PICs). When the three key elements of a photonic system, namely the optical source, the waveguide and the detector, are all built on a single substrate, the resultant device is called a 'monolithic optical incorporated circuit' (MOIC). When these three major constituents are obtained by using distinct component stages, the result is called a "hybrid optical incorporated circuit ". Although MOIC is the ultimate device due to its reliability and future high scale of integration, its implementation is extremely difficult, especially when multifunctionality is required. Optical-hybrid circuits, on the other hand, are relatively easy to build despite some compatibility issues between their key components (For example, if two materials have different thermal expansion coefficients, it might be required that they should be functioning at different temperatures and require dedicated thermoelectric coolers, which increases the complexity of packaging and cost, while reducing the reliability of the system) [4].

Currently, materials used for fabricating optical components include indium phosphide (InP), gallium arsenide (GaAs), lithium niobate ($LiNbO_3$), and Silicon (Si). Most successful implementations of MOIC use indium phosphide and gallium arsenide stages. Silicon on insulator (SOI) technology is also gaining increasing steam.

Micro-electronics uses a small number of key components such as transistors, resistors and capacitors to implement a range of features. The technology, which supports integration of these fundamental components, can be used for a wide variety of applications. Although photonic integration has much in common with integrating micro-electronics, the main difference lies in the different devices and physical processes that are used in the design of optoelectronics. It is also appealing to note that for photonic systems, the miniaturization process provides specific functional benefits, as was the case of electronic components. Reducing the physical dimensions in electronic devices may cause the corresponding decrease in capacitive effects, thus reducing time and energy, while the integration of optical elements (couplers, filters, multiplexers, lasers, detectors, modulators) would reduce losses and dispersion problems. However, as it is the case for integrated electronics, the physical limitations imposed by factors such as effective wavelength may also limit the miniaturization of photonic components. The integration of optical constituents or optical and electronic components on a single substrate has been the holy grail of the optical R & D community over the past 30 years. There are several reasons for the delay in the practical realization of fully integrated multifunctional optical devices. These include technological barriers related to accomplishing high-process consistency, replication, and manufacturing, as well as physical limitations linked to the nature of photons. Although photonic integration is still in its infancy, it has already established itself as a revolutionary technology that can provide significant benefits and improve people's daily lives. The impact of photonics in the telecommunications sector may be, as significant as that of microelectronics, especially if demand for communications systems and broadband fiber continues to increase in the future [5]. Large-scale photonic integrated circuits (PICs) represent an innovative technology that simplifies optical design conception, lowers space and energy consumption, and increases reliability of the device.

In conclusion, it is extremely important to develop a new series of functionalities which will finally make use of PICs and optical technology universal. In this context we believe that the thin films described in this thesis, and their fascinating magneto-optical properties, may finally find application in the realization of a new generation of non-reciprocal integrated optoelectronics devices.

Chapter 1

Synthesis, characterization and magneto optical properties of CeBiIG epitaxial films

Our interest in magneto-optical thin films stems from the study of the magneto-optical properties of the new compound $Ce_{2.2}Bi_{0.8}Fe_5O_{12}$ (CeBiIG proposed, synthesized and characterized during this work) whose Faraday Rotation has been proven to be the highest ever reported in the class of iron garnet materials [6-8]. In this chapter the motivation of this work, calculation of crystal structure and some basic principle of Faraday rotator are presented. The last part of this chapter focuses on the Faraday Effect and its use in fabrication of optical isolators.

1.1 Motivation

New technologies, based on magneto-optic materials have stimulated the research in the field and directed them towards the study of iron garnet thin films. Epitaxial garnet films have low optical absorption in the near-infrared, high refractive index, high Neel temperature[1] (450-500 K), and consistently exhibit a large magneto-optical effect, which makes them promising for magneto optical applications [9]. The properties listed have been crucial to applications such as temperature-independent optical isolators [10], (for removing undesired reflection in active laser systems), and magneto-optic visualizers [11] in which the use of Bi substituted iron garnet plays a prominent role. Doping or substitution of various aliovalent ions in YIG ($Y_3Fe_5O_{12}$), cerium-YIG ($Ce_xY_{3-x}Fe_5O_{12}$), and bismuth-YIG ($Bi_xY_{3-x}Fe_5O_{12}$) are among the most investigated approaches to increase the Faraday rotation of these compounds [12]. Comparative studies aimed at understanding the exact effect of the doping or substituted ions and to establish the nature of the ion that is most effective to enhance the Faraday Effect reveal that Cerium (Ce) is able to provide the highest magneto-optical induced rotation at infrared wavelengths (see Figure 1.1) [13]. However, the Ce content in the garnet structure is physically limited by

[1]The Néel temperature is the temperature at which an antiferromagnetic material becomes paramagnetic – that is, the thermal energy becomes large enough to destroy the macroscopic magnetic ordering within the material.

the crystallographic stability of the garnet structure (this is the reason why Ce related plot in Figure 1.1 stops before reaching the whole substitution for x = 3) [13].

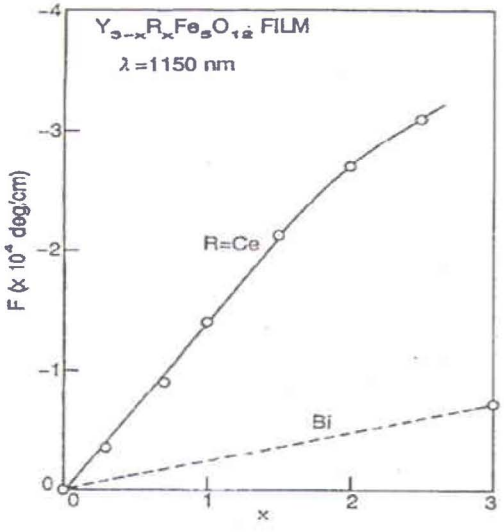

Figure 1.1 Faraday rotation (@ λ=1150nm) for $Y_{3-x}R_xFe_5O_{12}$ films as a function of the atomic concentration of "R" (where R = Ce and Bi). The plots refer to both Ce (solid line) and Bi (dashed line) substitution. Notice that Ce cannot be fully substituted because of its solubility limit in the garnet structure. (The image is taken from reference [13]).

In other words, an increase in the concentration of Ce in a garnet compound, promotes a larger Faraday Effect. However, beyond a certain concentration, the crystal will inevitably degrade into another structure that is no longer magneto-optic. On the other hand, if we use ions of Bismuth, full substitution can be achieved without compromising the desired crystal phase. Unfortunately, in this case, the results will be poorer in terms of magneto-optical activity [11]. The idea explored in our work is to combine the increase in magneto-optic properties, induced by Cerium substitution, with the stability granted by the substitution by ions of Bismuth, resulting in a remarkable magneto-optical material compatible with thin film technology.

1.2 The Crystal structure

Most of the physical properties of materials in the solid state are related to their crystal structures and symmetry [14-16]. One of the most notable garnet properties is its crystallographic compatibility with the addition and substitution of various lanthanide metal ions at specific sites in the parent garnet structure. The garnet structures are members of the cubic system - Ia 3d O^{10}_h, space group (230), which has a body-centered Bravais lattice belonging to the m3m group (see Figure 1.2 a) [14-16].

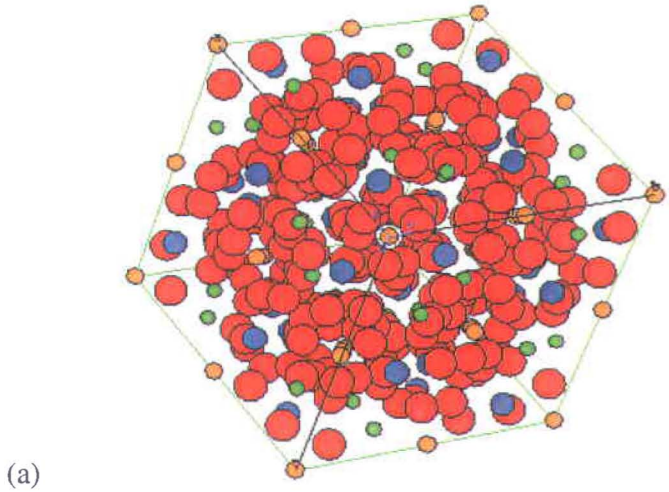

(a)

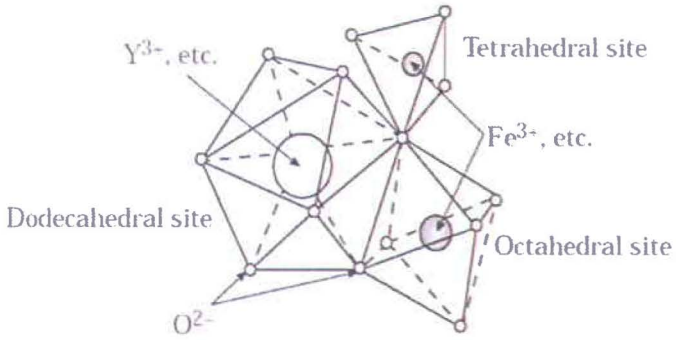

(b)

Figure 1.2 a) Unit cell of a typical structure of iron garnets, where the orange, green, red and blue spheres represent Fe^{2+}, Fe^{3+}, O^{2-} and Y^{3+} ions, respectively (the structure is calculated using CarIne software) b) Detail of the cation arrangement and local symmetries in the garnet structure and after references [16, 17].

The cubic unit cell consists of 8 formula units (containing 20 atoms each) with a total of 160 atoms: $\{c_3\}[a_2]\ (d_3)O_{12}$, where the individual brackets denote three different cation sites characterized by their coordination to oxygen, (h site): the c sites represented by "{ }" correspond to the dodecahedral sublattice; the 'a' sites indicated by "[ ]" relate to the octahedral sublattice, and the 'd' sites embedded in "( )" correspond to the tetrahedral sublattices [16]. The calculated structure is given in Figure 1.2 (a).

From Figure 1.2(b), it is apparent that each oxygen ion is part of two dodecahedrons, one octahedra, and one tetrahedra. This multiplicity of symmetries and coordination is the reason why an enormous variety of cations can be easily incorporated into garnet crystals. In CeBiIG, $Ce^{3+}$and Bi^{3+} ions occupy the dodecahedral sites.

1.3. The magneto-optical control of light

The Magneto-optical effect studied in this investigation is a nonreciprocal effect. In the Faraday Effect the direction of the rotation of the linearly polarized light depends only on the direction of the electron precession, which is solely determined by the direction of the applied magnetic field and not by the direction of propagation of the light. For certain applications, such as optical isolators and circulators, we need to utilize such a nonreciprocal phenomenon as it breaks the symmetry of the dielectric tensor. The Faraday Effect is further detailed in the following section.

1.3.1 Light propagation in magneto-optical materials

Magneto-optic materials are largely optically isotropic in the absence of an external magnetic field. However, when we induce a magnetic stimulation along the main crystallographic axis of a uniaxial material (generally the magnetic easy axis) the corresponding dielectric tensor becomes asymmetric, and it can be represented (for a uniaxial material) by the matrix:

$$\varepsilon = \begin{pmatrix} \varepsilon_x & -j\delta\varepsilon & 0 \\ j\delta\varepsilon & \varepsilon_x & 0 \\ 0 & 0 & \varepsilon_z \end{pmatrix} \tag{1.1}$$

Where, ± jδε are the components of the dielectric tensor affected by the magnetic field, μ (magnetic permeability in vacuum) is assumed to be unitary (over the light frequency range), and the "z" direction corresponds to the easy axis. When a linearly polarized beam propagates inside a magnetized material along its easy axis (say z-axis) and parallel to the magnetization vector M, it can be studied as the superposition of two orthogonal modes which are circularly polarized. If we describe these two modes as $\mathbf{E}_+$ (clockwise polarization) and $\mathbf{E}_-$ (counterclockwise polarization) and we identify E_x and E_y as their projections on "x" and the "y" axis respectively, we can write the following relations:

$$E_{\pm} = E_x \pm jE_y \tag{1.2-a}$$

$$|E| = E_0 = |E_+| + |E_-| \tag{1.2-b}$$

$$E_x = \frac{E_0}{2}\cos(\omega t); \quad E_y = \frac{E_0}{2}\sin(\omega t) \tag{1.2-c}$$

$$E_{\pm} = (E_0/2)e^{\pm j\omega t} \tag{1.2-d}$$

By using the equation $\mathbf{D} = \varepsilon_0 [\varepsilon] \mathbf{E}$ we can evaluate the electric flux density vector for both the left-handed and right-handed polarized beams as:

$$D_+ = \varepsilon_0 \varepsilon_+ E_+ \tag{1.3-a}$$

$$D_- = \varepsilon_0 \varepsilon_- E_- \tag{1.3-b}$$

where $\varepsilon_{\pm} = \varepsilon_x \mp \delta\varepsilon$

The two propagation constants related to the two circular polarized modes, with an obvious notation, are:

$$\beta_+ = \omega\sqrt{\varepsilon_0 \mu_0 \varepsilon_+} \tag{1.4-a}$$

$$\beta_- = \omega\sqrt{\varepsilon_0 \mu_0 \varepsilon_-} \tag{1.4-b}$$

The physical meaning of these two relations is that in a magnetic material, magnetized along the direction of the light propagation, the right and the left circularly polarized beams have two different propagation constants. This phenomenon is intrinsically nonreciprocal (since the forward and the reverse propagating beams are affected differently with respect to the light propagation). By exploiting this asymmetry

of the dielectric tensor, it is possible to produce fundamental optical components such as rotators, and isolators.

1.3.2 Basic operating principle of a Faraday isolator

Consider a linearly polarized light beam that is propagating along "z" where the "x" and "y" components are $E_x=E_0\cos\omega t$ and $E_y=0$ respectively, at z=0. Further, assume that the electromagnetic wave is incident on a magneto-optic material placed in a uniform magnetic field directed along "z" as shown in Figure 1.3, where "z" is the easy axis of the magnetic crystal.

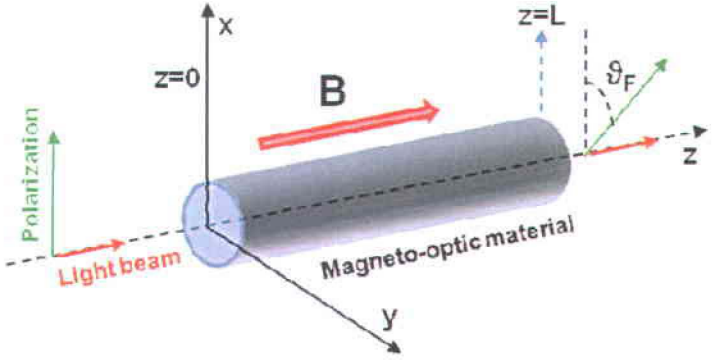

Figure 1.3 Faraday Effect in a magneto-optic material. The image depicts the Faraday rotation that occurs on the linear polarization of a beam which propagates along a magneto-optic medium immersed in a uniform magnetic field.

At z=0, the incident wave can be studied as the superposition of two circular components E_{+in} and E_{-in}:

$$E = E_{+in} + E_{-in} = (E_0/2)e^{j\omega t} + (E_0/2)e^{-j\omega t} \tag{1.5}$$

While the output wave, at z=L can be represented as:

$$E = E_{+out} + E_{-out} = (E_0/2)e^{j(\omega t-\beta_+ L)} + (E_0/2)e^{-j(\omega t-\beta_- L)} = E_0\cos\{\omega t - \frac{1}{2}(\beta_+ - \beta_-)L\}e^{j\frac{1}{2}(\beta_+-\beta_-)L} \tag{1.6}$$

This represents a linear polarized wave, whose polarization is rotated by 45° with respect to the input beam [18],

$$\vartheta_F = \frac{1}{2}(\beta_+ - \beta_-)L \tag{1.7}$$

By using the Equations (1.4-a) and (1.4-b), and under the condition that $\varepsilon_x >> \delta\varepsilon$, it is possible to rewrite the magnetically induced rotation angle as:

$$\vartheta_F = \frac{\omega}{2}\sqrt{\frac{\mu_0\varepsilon_0}{\varepsilon_x}} \cdot \delta\varepsilon \cdot L \tag{1.8}$$

If the magnitude of the applied magnetic field "H" does not exceed the limit of the linear proportionality with $\delta\varepsilon$, the rotation angle can be expressed by:

$$\vartheta_F = VHL \tag{1.9}$$

where V is the Verdet constant, a characteristic parameter of materials and whose value depends on the material, wavelength and temperature [19]. Thus, the crystal in Figure 1.3 is nothing but a Faraday Rotator.

If a Faraday Rotator works in synergy with two polarizer's rotated at 45° with respect to each other, as sketched in Figure 1.4, it results in another fundamental optical component - the optical isolator [20]. This device is an important component in optical systems since it blocks undesired reflections that cause, for instance, instability in the optical cavities of the laser sources. The working principle is simple: the forward propagating beam is rotated 45° by the Faraday rotator to match the optic axis of the output analyzer and passed through it without any attenuation. Due to the nonreciprocal nature of the Faraday Effect, the back reflected beam is further rotated another 45° and has thus a polarization which is crossed (at 90°) with the input polarizer, and cannot reach the laser source (not shown in the scheme). The heart of the optical isolator is the Faraday Rotator and its rotation per unit length is provided under saturation conditions. The latter is defined, from the hysteresis curve of the Faraday rotation, as a function of the magnetic field "H" where further increase in a magnetic field strength will result in no further change in the Faraday rotation. A material that could provide a sufficiently high Faraday Effect at communication wavelengths – making an integrated optical isolator possible - does not yet exist, despite the benefits it could provide to the field of integrated photonics for example ring resonator which is recently demonstrated by MIT researchers [21].

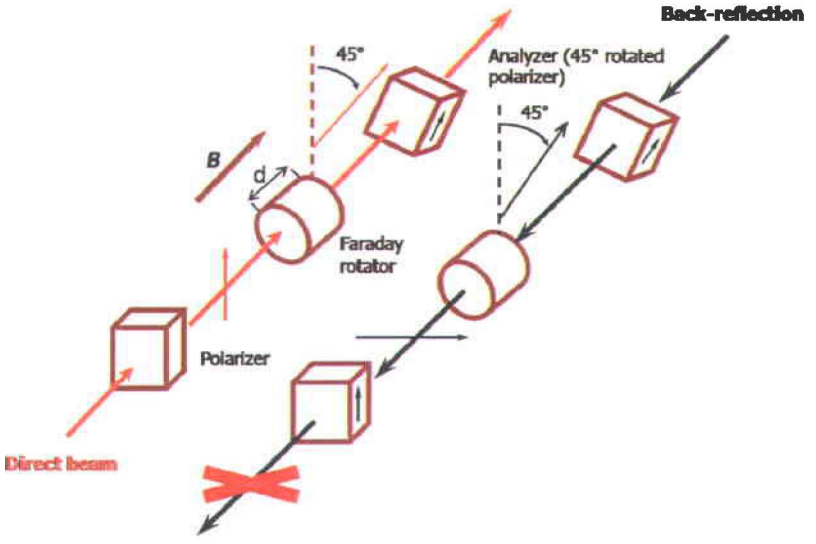

Figure 1.4 Working principle of an optical isolator based on the Faraday rotation. The Faraday rotator, placed in a saturation magnetic field, rotates the linear polarization of the forward propagating beam that has crossed the first polarizer by 45° in such a way that it can pass through the output analyzer without any attenuation (forward path: red arrow). The back reflected light instead, because of the nonreciprocal nature of the rotation induced by the magneto optic material, is further rotated another 45° and is blocked by the input polarizer (now a cross-polarizer), preventing any back-reflection damage to the laser cavity.

In this context, the present research is focused on $Ce_{2.2}Bi_{0.8}Fe_5O_{12}$ (CeBiIG) films, a new magneto-optic material with a very high Faraday rotation per unit length acquires its full significance, and further characterization details are presented in Chapter 4.

Chapter 2

Growth of semiconductor CeBiIG -epitaxial thin films

In this chapter, it is discussed about the importance and history of deposition by laser ablation, which has been employed to develop novel magneto-optic $Ce_{2.2}Bi_{0.8}Fe_5O_{12}$ (CeBiIG) thin films. The concept is summarized in a short section, while paying attention to the key parameters that control the Pulsed Laser Deposition (PLD). In addition, techniques such as thermocouple calibration, annealing and profilometry are also described in detail.

2.1 Brief comparison between critical growth processes

There is currently a keen interest in developing thin films of novel magneto-optic materials. Several physical and chemical deposition techniques can be used to produce thin films [22, 23]. Physical methods can be divided into vacuum evaporation (which includes laser ablation) and sputtering, while chemical methods include vapor phase and liquid phase based depositions.

To produce the samples described in this work, it is considered mainly two techniques widely described in the literature. The first method is known as PLD (Pulsed Laser Deposition), which is a physical process based on the local ablation of the chosen material by powerful laser pulses forming a ionized plasma, followed by its rapid expansion; the second is the so-called sol-gel technique (chemical method) based on liquid-phase deposition. PLD generally produces films with the same stoichiometry as that of the target material, while the sol-gel technique involves the hydrolysis and condensation of organometallic precursors on a given substrate.

Both techniques have advantages and disadvantages. For instance, during PLD deposition some aggregates can appear on the film surface, while after the sol-gel process, the deposited film can show some undesired porosity, both of which may lead to light scattering and other optical losses in the film [24, 25]. Because PLD [25-29] gives the best results for semiconductor and magneto-optical materials, we chose to employ this versatile and yet powerful deposition process in the present investigation.

2.2 Brief history of laser deposition

Albert Einstein postulated the stimulated emission process in 1916. However, the first optical maser using a ruby crystal as the lasing medium was designed 44 years later (1960) by Theodore H. Maiman at Hughes Research Labs. In 1962, Breech and Cross used a laser to ablate a ceramic material with a ruby laser; they vaporized and excited atoms from a solid surface. Three years later Smith and Turner were able to obtain, for the first time, a thin film using a laser ablation technique. This marked the birth of pulsed laser deposition as a technique to produce high quality thin films. However, research and development of PLD system did not initially gain much momentum. Immature laser technology, the instability of the output beam and the low repetition rate did not allow for appreciable film growth in a reasonable time. Thanks to a rapid growth in photonics technology (resulting, for example, in the design and manufacture of reliable Q-switched laser sources), the PLD deposition technique became competitive with the other film deposition techniques. Later, the development of lasers with high efficient harmonic generation, such as excimer lasers, delivering powerful UV radiation, helped PLD to become an attractive and widespread deposition technique. During the last decade, pulsed laser deposition (also called plasma laser deposition or laser ablation) has been widely employed to produce crystalline (and epitaxial) thin films of materials with complex chemical compositions [29-31].

2.3 Basic principles on Pulsed laser deposition

The first functioning laser was assembled in 1960, and since then it has been developed into one of the most influential and powerful tools in modern science. Today, its distinctive properties such as a narrow frequency bandwidth, unique coherence and high-power density make it an extremely useful tool for material processing, through laser ablation. In particular, the advantages of PLD over other deposition techniques (such as sputtering) include i) a small target size; ii) the possibility of reproducing the stoichiometry (i.e. the composition) of the initial target material, even if the stoichiometry of the latter is complex and iii) since the energy source is located outside the vacuum chamber, the possibility of using a smaller deposition chamber, allowing for a complete vacuum system with a simplified framework for deposition. As for other film deposition

techniques, multilayer structure can also be obtained using consecutive depositions, which is faster and less tedious with PLD when compared to sputtering [32-34].

The principles underlying PLD are fairly straightforward. Laser ablation requires a source of laser radiation such as an excimer laser which generates a strong-pulsed laser beam in the UV range. This laser is focused onto the surface of a ceramic target, where the strong absorption of the electromagnetic radiation by the surface leads to rapid ablation of the target material (Figure 2.1), resulting in an atomic cloud or ionized plasma, also called plume, that contains the same elements in the same proportion as the composition of the target.

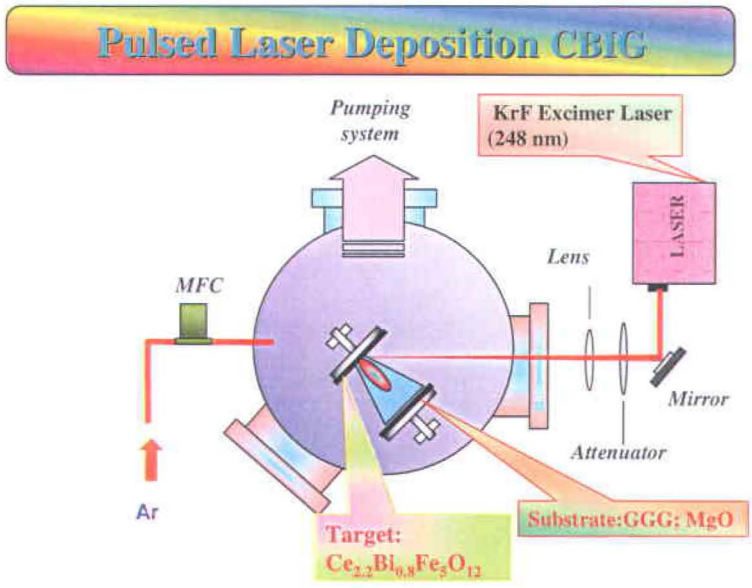

Figure 2.1 Schematic diagram of the PLD system at INRS.

The exact shape of the plume depends on the angle φ formed between the normal to the target surface and the laser direction, as shown in Figures 2.2. a) and b). The plume shape also varies when changing the fluency of the laser, which is the energy per unit area and time, delivered by the incident beam on the target measured in $\left[J/(cm^2 \cdot \sec)\right]$. The different shapes that plasma assumes when changing the incident angle φ are described by the formula $\cos^n \vartheta$, where ϑ is the angle between the direction of the flight

particles and the target surface normal, and 'n' is an empirical coefficient dependent on both the material and the incidence angle φ [34-37]. It is to be noted that the energy delivered to the target by the laser beam must be in a suitable range.

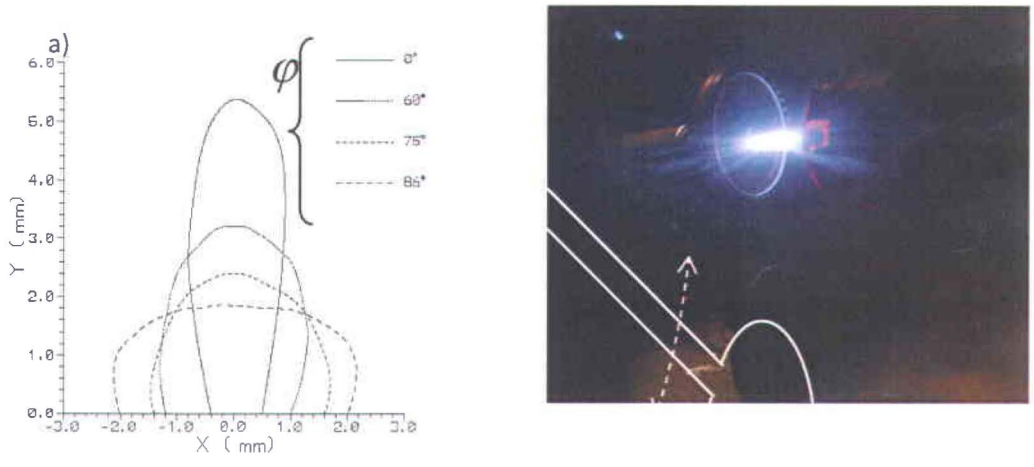

Figure 2.2 a) Plume shape with respect to the incident angle b) Photo taken during a deposition.

The lower limit of this range is the minimum value of energy below which no local ablation can occur. The upper limit is the largest energy value above which the ablation process cannot be controlled. A great advantage of the PLD technique is the small number of parameters that need to be controlled before and during the deposition. The main deposition parameters are as following:

1) The temperature of the substrate.
2) The pressure inside the deposition chamber (and nature of the gas atmosphere).
3) The target to substrate distance.
4) The laser fluency (related to both repetition rate, power of the laser and wavelength).
5) The deposition time.
6) The temperature rate during the substrate cooling, after the deposition.

The substrate temperature is a key parameter because the thermal energy at the growing sample's surface allows the particles, which travel from the plasma cloud to the substrate surface, to reorganize themselves into an ordered layer. The substrate

temperature is a critical parameter for producing epitaxial films with a preferred orientation. In addition, the nature of the substrate (crystalline) and the atomic properties of its surface play also a prominent role for a good epitaxial growth. The interaction between the impinging atomic species and the substrate surface are quite complex and the different mathematical models still leave some questions unanswered. It is now well established that depending on the interaction between substrate and plume, the film formation can occur in distinct growth regimes as explained in the following paragraphs on epitaxial growth modes.

The first mode is called the Frank -Van der Merwe or layer-by-layer growth mode (Figure 2.3), in which the atoms of the deposited material are attracted to a greater degree by the substrate than by each other. This is the deposition regime which allows for the highest quality epitaxial films. This growth is favored when the ablated atom-substrate binding energy, ΔE_{as}, exceeds the cohesive energy between ablated atoms ΔE_{aa} [38]. In

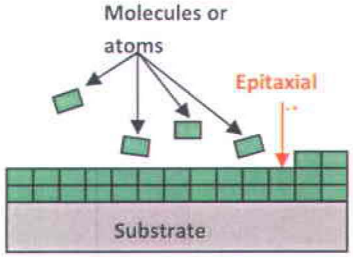

Figure 2.3 Frank - Van der Merwe or layer-by-layer growth mode.

the second mode (Figure 2.4), the Volmer - Weber or island growth mode, the atoms inclined to generate spontaneous aggregates or isles over the substrate surface. The Volmer – Weber mode is favored when the cohesive energy between ablated atoms ΔE_{aa}, exceeds the ablated atom-substrate binding energy, ΔE_{as} [38].

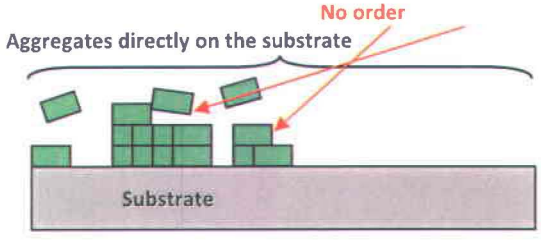

Figure 2.4 Volmer – Weber or island growth mode.

In the third regime (Figure 2.5), the first few atomic layers of a thin film usually grow as layer by layer of the depositing material centered on nucleation sites (Volmer –Weber mechanism) and high substrate temperature favors the growth of 3D islands either directly on the substrate or on one or several stable ad-layers of the deposit. This method of deposition is known as the Stranski-Krastanov or mixed growth mode [26-29, 39, 40].

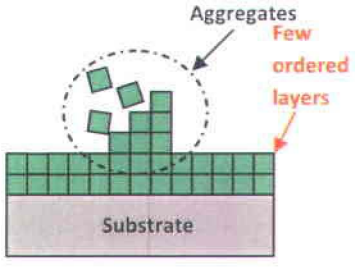

Figure 2.5 Stranski-Krastanov or mixed growth mode.

In any deposition technique, the pressure inside the vacuum chamber is the most important physical variable to be controlled in order to produce a film with significant structural and magneto-optical characteristics [41, 42]. Therefore, we decided to focus on the study of this parameter, which varied in a range from 50 to 500 mTorr (while all the other parameters were constant). The pressure significantly affects the shape of the plume during the deposition [37, 42, 43]. When the pressure increases, the plume tends to collide with a larger quantity of gas particles and it will become shorter. By maintaining the dynamic equilibrium in the PLD chamber with a continuous mechanical pumping during the deposition, it is possible to obtain the required conditions for the deposition of high quality films. The pressure range inside the chamber to obtain the desired CeBiIG phase depends on the nature of the substrate (amorphous, polycrystalline or single crystalline) and to the composition of the target ablated, while the gas employed during the ablation process can be either inert (e.g. Ar) or reactive (e.g. oxygen for oxide films). In many cases, nitrogen may be used to control the properties of the plume. An other influential parameter is the target-substrate distance, which not only affects the growth rate but also influences the quality of the film, affecting the uniformity of the film composition and thickness. Another decisive parameter is the fluency, which can be

varied by either changing the laser pulse energy or by adjusting the laser spot size. Finally, by changing the deposition time it is possible to control the thickness of the film. Ultrathin films show a high degree of crystallinity, although deposition time is an extremely critical parameter in the epitaxial growth of any thin film. It is also monitored the temperature during the deposition, which is a critical parameter in epitaxial process, where the kinetic energy of the particles has to be controlled to allow the particles to arrange themselves into a complete lattice [38].

As stated earlier, it is easy to understand that epitaxial processes need more time, attention, and is more difficult to translate into industrial processes. In our investigation, more attention was paid to the production of high quality films with optimal magneto-optical properties than to a process easy to upscale for a possible industrial production. Accordingly, a procedure using PLD on single crystal substrates was adopted for the synthesis of our CeBiIG films.

The PLD system offers several advantages in forming multicomponent thin films. The most significant advantage is the congruent transfer (i.e. the film has the same stoichiometry as the target) from a complex multicomponent ceramic target to the substrate. These features provide an easy preparation of films with complex stoichiometry. With proper laser energy and wavelength, almost all materials can be ablated to produce the finest quality thin films. Note that relatively high deposition rates can be easily achieved with PLD by performing in-situ or post annealing either in Argon or Oxygen. The disadvantages with the PLD process include possible formation of droplets and the lack of uniformity over large areas resulting from the narrow angular distribution of the plume. The plume will not only carry atoms, ions and molecules, but could also carry small droplets that can result in rough films and can lead to scattering and absorption, which is detrimental in optical applications [35, 44]. Several methods have been developed to reduce this effect: for instance, rotation of the target and scanning the laser beam do reduce droplet formation. Also by using dense-smooth targets [28, 45], and a dual beam ablation procedure, it is possible to minimize the number and density of droplets which are frequently encountered in the PLD technique [46].

2.3.1 Pulsed laser deposition setup

A schematic of the functional setup (including alignment and focusing of the laser beam) of the PLD system, shown in Figure 2.6, is described below. The laser source was a KrF excimer laser (GSI Lumonics, wavelength 248 nm, pulse length 17 ns, pulse energy up to 350 mJ, beam size up to 2.5 cm x 1 cm). A spherical lens was placed at the entrance of the vacuum chamber to focus the beam into a small spot size ($0.045\ cm^2$), reducing the elliptical aberration of the laser waist.

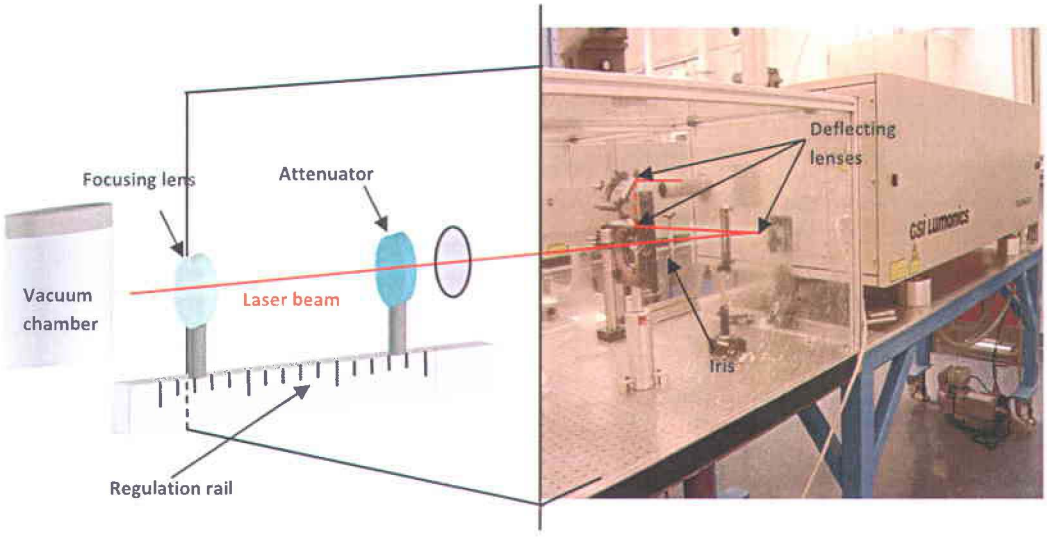

Figure 2.6 From left to right: alignment and focusing optics, excimer laser with deflecting lenses.

Changing the lens position on the regulation rail alters the desired energy density on the sample surface. A beam attenuator (OPTEC AT-4030) is placed in the beam path before the spherical lens and after the line up system (comprised of three additional lenses), to adjust the laser pulse energy (and the fluency) without altering the laser's working conditions or the focusing optics. The attenuator is used to regulate the energy of the irradiating pulse between zero and its maximum value, as the gases inside the laser need a minimum of energy to be excited, in turn resulting in a nonzero minimum for the irradiation energy.

Next, the discussion is focused on the vacuum chamber (Figure 2.7). The vacuum chamber is characterized by a metallic arm connected from one side to a motor and on the other side to the target. The sample holder is connected in series to both heater and

motor. The motor connected to the sample holder gives it a rotating movement; the second motor fixed to the metallic arm provides roto-translation to uniformly ablate the target.

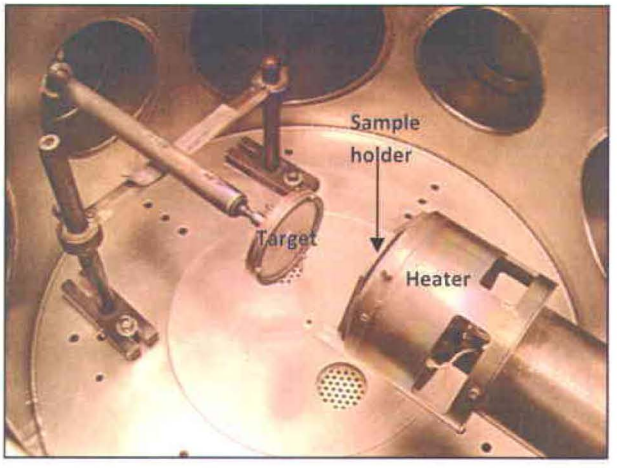

Figure 2.7 Inner part of the vacuum chamber.

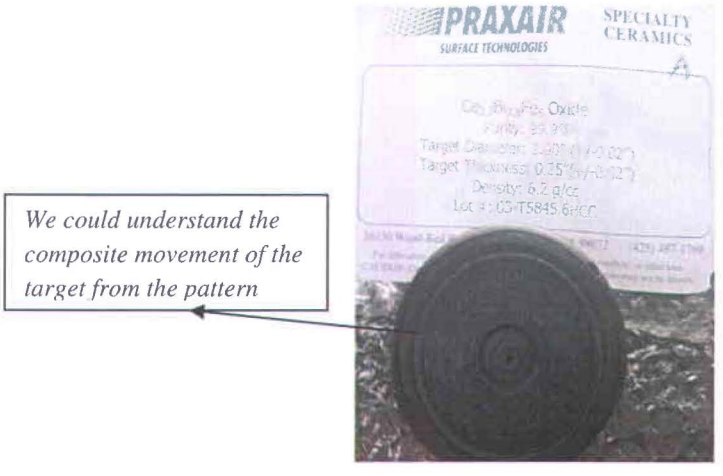

Figure 2.8 Pattern burned on the CeBiIG target surface by the laser beam.

The quality of the laser exposition on the target can be checked by looking at the pattern "burned" on the target surface (Figure 2.8). In the chamber, the shutter is placed between the target and the sample, which can be removed during the deposition. The purpose is to protect the substrate during the first minute of the ablation, needed to clean

the target surface. Located outside the deposition chamber is a pumping system comprised of two pumps in series, a mechanical roughing pump (on the floor) connected to a turbo-molecular pump (connected directly to the vacuum chamber). With the combined use of the two pumps and the inlet of a chosen ambient gas, one can obtain the necessary conditions to reach the viscous regime- $5x\ 10^{-1}$ cm –torr. In this regime, the collisions of molecules with themselves overcome those between the molecules and the walls (the opposite is true for the molecular regime-5×10^{-3} cm-torr). At the border between the two regimes is the mean free path, which is the statistic average of the distances covered by the molecules in their chaotic motion. This value is about 0.1mm in our conditions.

By controlling the pressure in the deposition chamber, it is possible to control the mean free path of the ambient gas in the chamber and therefore the interactions between the particle in the chamber and in the plume. This permits to workout on the optimal deposition condition, and in particular to achieve a uniform deposition. Prior to these measurements we performed a thermocouple calibration that is mentioned in the following section.

2.4 Thermocouple-calibration

For precise temperature measurements, the thermocouples must be calibrated. Calibration is performed by comparing a device or the output of an instrument to standard having known measurement characteristics. Calibration is an essential method to monitor and improve the measurement accuracy of the equipment. Calibration procedure consists of measuring the thermocouple emf at a series of almost uniformly spaced temperatures, as established by standard instruments [47, 48]. Once the relationship of the temperature gauge to the standard is known and accepted, the new temperature gauge can be used to determine the temperature of other equipment or systems. In order to interpolate between calibration points, the coefficients of a polynomial equation are determined to express the difference of the emfs from an accepted temperature versus emf table from the standard. Thermocouples are based on Seebeck effect. A thermocouple consists of two dissimilar materials which are joined at their ends to form a circuit. An emf is developed when they are at different temperatures. One junction is kept at fixed temperature called as reference

junction usually at 0°C. The other junction is the probe junction and emf depends on this junction. The current will be proportional to the difference in temperature between the junctions and the metals used. The higher the temperature difference, the higher is the electromotive force (emf) and the current flow in the loop. The magnitude of the emf is in the order of few millivolts. Tables are usually employed for the conversion of emf (milli volts) to temperature [47-49]. High temperature platinum resistance thermometers are

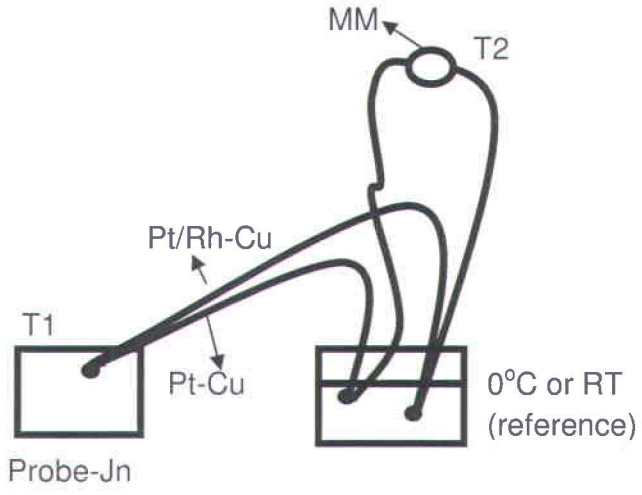

Figure 2.9. Basic Thermocouple circuit.

much more precise, stable and are remarkably useful for improved calibration. At higher temperature in the range of 400-800°C, thermocouples employing platinum-copper and platinum rhodium- copper alloys for their thermo elements are more resistant to oxidation, have higher melting points. Therefore, in this case the two metals and alloys with Pt-Cu and Pt-Rh-Cu are made with two main junctions that are kept at 0°C as shown in Figure 2.9. The emf is measured between two copper leads and whose junctions are at 0 and T°C. The details of the measurement are given below [49].

Data for a particular probe (test) thermocouple is obtained by measuring the emf of the reference thermocouple and the emf of the test thermocouple simultaneously. From these data, values for the temperature of the common measuring junction and the emf of

the test thermocouple are determined and some of the measurement details are mentioned in the following.

2.4.1 Measurement details

The test assembly (as shown in the Figure 2.9) is immersed into the test temperature medium and provides sufficient time for the test assembly to stabilize. Once the test assembly is stable the EMF generated between the test specimen and the reference standard is recorded [47]. Once the reading is taken, the test temperature will be raised to the next higher temperature, by removing the test assembly from the temperature source, or advance the test assembly to the next temperature source. We allowed the temperature source and the test assembly to stabilize as before, and get a second set of readings at the new temperature. In all cases we found the readings in sequence from the lowest to the highest temperature cited in the following table 2.1.

Table 2.1-Thermocouple calibration –parameters

Furnace/Bath Temperature, T_{Fur} [° C]	Multimeter reading, MM(mV)	Total emf $E = E_{MM} + E_{RM}$ [mV]	Temperature corresponding to E, $T_{Thermo\text{-}C}$ [° C]
30	0.361	1.179	29.4
35	0.579	1.397	34.8
40	0.788	1.606	39.9
45	0.995	1.813	44.9
50	1.202	2.020	49.9

From the theory of thermocouples [47], the multimeter reading corresponds to the difference in temperature between the surroundings (room) and bath. To calibrate the thermocouple, we have to take the room temperature into consideration to get the absolute value of temperature measured. After finding the corresponding millivolt value for the room temperature from the corresponding thermocouple table (E_{RM}), we need to add that millivolt value, corresponding to the room temperature, to every multimeter reading (E_{MM}). Tabulated the values and finally plot the measured bath temperatures values (T_{Fur}) on y-axis against the corresponding thermocouple emf (millivolt) values (E)

on x-axis. We found the slope, intercept and the correlation coefficient of the curve-fitted line by fitting (polynomial) methods. The parameters related to calibration are given in the table that serves as example and sample readings with room temperature, 20.5°C and corresponding mV reading from tables E_{RM} = 0.818 mV are displayed [47-49].

In the present case, we slightly modified the above procedure and described in the following.

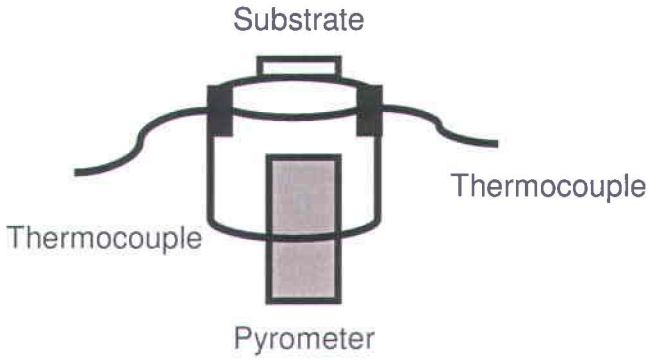

Figure 2.10 Schematic diagram of thermocouple calibration where one thermocouple is grooved on the substrate holder, another one in contact at the other side, and a standard Pyrometer has been used.

The temperature was estimated from the reading of the temperature by a thermocouple positioned on the substrate holder which is kept in the groove as shown in the Figure 2.10, that is specially made for the thermocouple. The actual temperature to be measured is the temperature of the substrate which has been measured using an optical pyrometer and denoted with T_{pyro}. The temperature measured by thermocouple is different from the temperature of the substrate. Since the thermocouple is positioned on the substrate holder side (Figure 2.10) that is away from the substrate, where the heat flow is lower compared to that transmitted to the substrate.

Precisely, the value of the synthesis temperature T was estimated from the value of the temperature measured by thermocouple T_{thermo} and extrapolation of the gap at high temperature (i.e. for T> 752°C). It can be seen from Figure 2.11 that ΔT is calculated

from the temperature measured by the thermocouple and the temperature measured with the pyrometer.

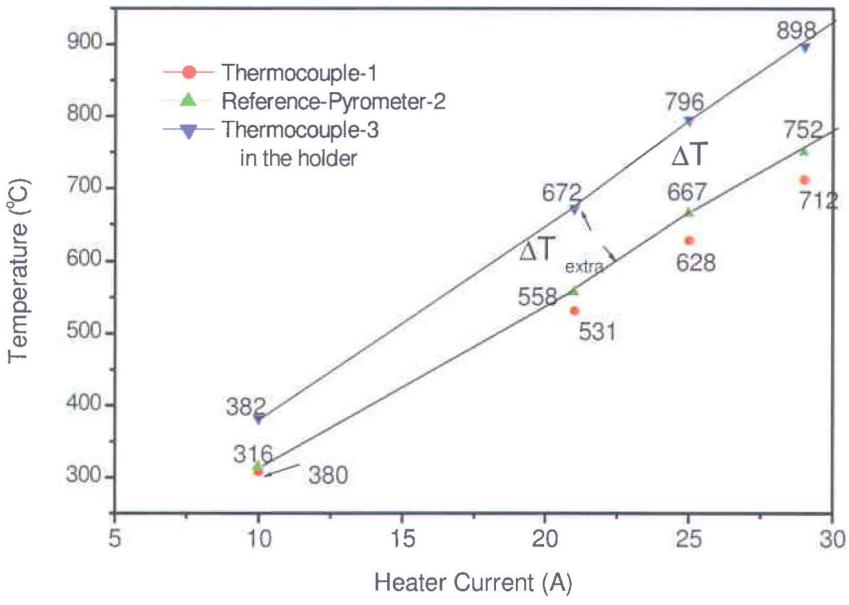

Figure 2.11 The calibration chart of the two thermocouples (one is grooved in the susbtrate holder and the other one kept at the side of the substrate holder) against the reference thermometer T_{pyro}.

Here the values given by the thermocouples and the pyrometer (T_{pyro}) are compared after a second order polynomial fit for estimating the exact temperature ($T > 752^{o}C$, $T=T_{pyro}$) of the substrate.

2.5 Annealing

In metallurgy, the annealing procedure is used for heating and controlled cooling of a material, to increase the grain size of its crystalline domains, and to remove any defects. The heat causes the atoms to move from their initial position (a local minimum of the internal energy), and randomly pass through states of higher energy. Subsequently, when the crystal is slowly cooled, the atoms have the option of finding arrangements with lower internal energy than the initial one, which leads to an arrangement with increased order and reduced internal stress. Accordingly, the control of two main parameters, i.e.

the annealing temperature and annealing time in addition to the time dependence of the temperature, is required to achieve an ideal annealing process.

In general, the annealed films are polycrystalline and their grain size is dependent on the annealing temperature, annealing time, as well as on the ambient during annealing, for instance the percentage of oxygen/argon inside the oven for oxide films [42, 50, 51]. An annealing time of 30-45 minutes is commonly used after the PLD deposition of oxides. As observed in our experiments, longer annealing time (up to 60-80 minutes) may affect the outcome of the thermal processing. However, the temperature during film growth and annealing temperature are arguably the most influential and critical parameters for any crystalline film growth [52]. A fine adjustment of the temperature is thus required for each deposition and annealing. However, it must be noted that too low temperatures will not be effective in annealing the sample. On the other hand, exceedingly high temperatures will damage the samples. Besides from using a proper temperature control, it is possible to optimize the composition and quality of the films by depositing/annealing in the presence of reactive gases such as oxygen. Indeed, in the case of oxides (depending on the specific material), it may be useful to expose the target and growing film to oxygen while depositing/annealing in order to fill the oxygen vacancies inevitably produced in the film during the PLD deposition.

One of the advantages of the laser ablation technique is that the annealing process can be performed "*in situ*". In other words, it is possible to exploit the controlled and slow decrease of the temperature of the sample holder to have a process remarkably close to an "*ex situ*" annealing that would be carried out in an oven after the deposition is complete. The annealing is performed inside the vacuum chamber and without opening the system.

However, for some materials, we had experimental evidence that the thermal energy on the substrate surface alone is too small to start the nucleation process and get crystalline films. Post annealing of films gives yet another option to control the composition and the crystal structure of the film.

Figure 2.12 a) Details of the triple temperature controller; b) annealing oven.

To develop CeBiIG films with the desired crystal structure, a subsequent annealing process at temperatures 680±20°C is required. It was performed both in situ and *ex situ* using the PLD chamber and oven to verify the crystalline structure of CeBiIG films. The *ex situ* system is composed of a Lindberg annealing oven (Wet Chem. Lab), with a triple temperature controller, a quartz tube which constitutes the chamber, a quartz crucible that also works as a trolley to transport the samples in and out of the oven. Primarily this system allows various gases, such as argon or oxygen, to flow in the tube. The system is shown in Figure 2.12, where we can also see the triple thermal controller.

There are three controllers on the oven in order to manage three heaters inside the quartz tube and maintain a uniform gradient of temperature inside the oven. Of great significance to our experiment are the annealing parameters used to produce the final set of samples: an annealing time of 45 min and a temperature of 680°±20°C in an argon atmosphere are crucial for producing the highest quality CeBiIG epitaxial films.

Chapter 3

Characterization techniques used for the study of the CeBiIG epitaxial thin films

In this chapter, we provide the theory behind the characterization tools employed in the present investigation. It is also described about setup and practical importance for each technique. In the current scientific literature, it has been observed that most physical and chemical properties of solid materials change when their size is decreased down to the nanometer range or if the atomic aggregates modify their dimensions [53-56]. These changes can be attributed to quantum size effects, surface-interface effects, variations in the cell parameter and lattice perfection and symmetry. Also, most of the macroscopic properties of nanocrystalline materials are strongly related to their morphological and micro structural properties. To describe the microstructure, chemical composition and magneto optic performance of CeBiIG thin films, the following techniques are employed such as Profilometry, Scanning Electron Microscopy (SEM-EDX), X-Ray Diffraction (XRD), Atomic Force Microscopy (AFM), Magnetic Force Microscopy (MFM), X-ray Photoelectron Spectroscopy (XPS) and Faraday rotation.

3.1 Thickness measurements-Profilometry

The two methods used to determine the thickness of the samples are ellipsometry and profilometry. The primary tasks of ellipsometry are the measurement of the optical constants and thickness of thin films. Ellipsometry measures the change in polarization state of the light reflected from the surface of a given sample, and this variation is strictly related to the optical characteristics of the material and to its thickness. Difficulties associated to this technique (especially related to the control of the growth rate of CeBiIG thin films and this is to determine the film thickness) lead us to employ profilometry, a technique used to find the surface characteristics of a given film. The main issues using ellipsometry are; i) Depolarization (generation of different polarizations upon light reflection) effects in the samples increasing measurement errors, ii) surface light

scattering due to large surface roughness of the CeBiIG films, and iii) thickness in-homogeneity in the PLD grown CeBiIG thin films on GGG substrates.

Profilometry is the fastest and simplest method for measuring film thicknesses. A sharp needle in contact with the sample is moved along a straight line. The vertical movement of the needle is measured by the reflected laser light, and the trace is recorded with high accuracy. To measure the thickness of a thin film via this method, part of the substrate has to be protected during growth. This was easily arranged because the corners of the substrate were always covered with a metal mask formed by the sample holder. The film thickness is then evaluated by recording a height profile and measuring the step height in the profile between the bare substrate and the film coated substrate. Most of the deposited oxide films are pretty hard, so the possibility of scratching the films with the needle is small, as the contact force is quite weak. One disadvantage with this method is that it relies on the thickness measured in a corner of the sample, and not in the center, where the uniformity of the material is higher. In our experiments, a SLOAN DEKTAK 3030 surface profiler was used (see Figure 3.1). The setup can also be used to determine surface roughness and infer the quality of the deposition.

The measured thickness and the corresponding deposition times are used to calculate the deposition rate or film growth rate related to the deposition conditions used (substrate temperature, pressure, substrate-target distance, etc.).

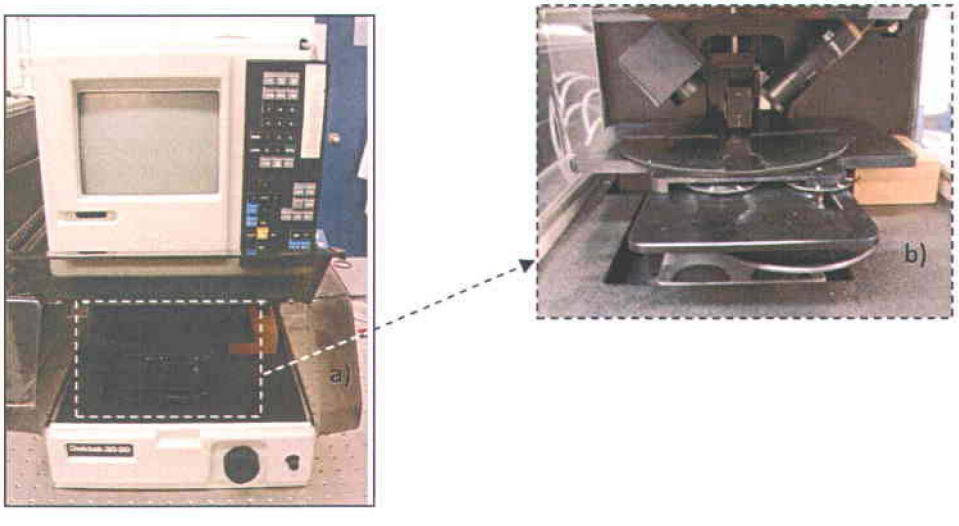

Figure 3.1 a) Profilometer; b) Zoom on the analysis plate.

3.2 Scanning Electron Microscopy

3.2.1 Quality surface control after deposition

The Scanning Electron Microscope (SEM) is used to evaluate the surface topography of a material with a two-dimensional image. This characterization is remarkably fast, easy to use, does not damage the sample and it permits to quickly check the quality and reproducibility of the deposited layers. Next, the theory behind this technique and its practical applications are described.

3.2.2 Principle of operation of the scanning electron microscope

The invention of the electron microscopy takes advantage of the properties of rapidly moving electrons (Louis De Broglie, 1924). It is well known that quantum particles such as electrons have both particle-like and wave-like features, even though no experiment can see both particles and wave properties simultaneously, as revealed by the complementary principle [57]. An optical microscope has a resolution expressed by $K\lambda/NA$, where K is a constant dependant on instrument and NA is the numerical aperture (equal to "$n\sin\alpha$", where n is a refractive index and α is one half of the angular aperture of the lens). According to the wave particle dualism, an electron can be associated to a wave whose wavelength is $\lambda = h/mv$, where h is Planck's constant and mv is the momentum of the particle. Therefore by accelerating a flux of electrons we can increase the resolution well over that of normal light. Visible light has wavelengths from 4,000 to 7,000 Å, while electrons accelerated to 10,000 keV have a wavelength of 0.12 Å. Optical microscopes have their resolution limited by the diffraction of light to a magnification of about 1,000. Electron microscopes are limited to a magnification of approximately 1,000,000 due to spherical and chromatic aberrations [58, 59]. Scanning electron microscopes have resolutions as high as 25 Å.

We observe that a scanning electron microscope produces an electron beam in a vacuum tube. This beam is collimated by electromagnetic "condenser" lenses, focused by an objective lens, and scanned across the surface of the sample by electromagnetic deflection coils as seen in Figure 3.2 [60]. The electron beam comes from a filament, made of various types of materials. The most common is the Tungsten hairpin gun which

operates as a cathode [60]. Voltage applied to the loop results in the filament heating up. Attractive forces which accelerate the electrons toward the sample. The imaging system consists of collecting the secondary electrons released by the sample. These secondary electrons are detected by a scintillating collector. The quanta of light generated by interacting electrons with the scintillator are then detected and amplified by a photomultiplier tube. Hence, it is possible to display an image with a better resolution than the one obtained with an optical microscope.

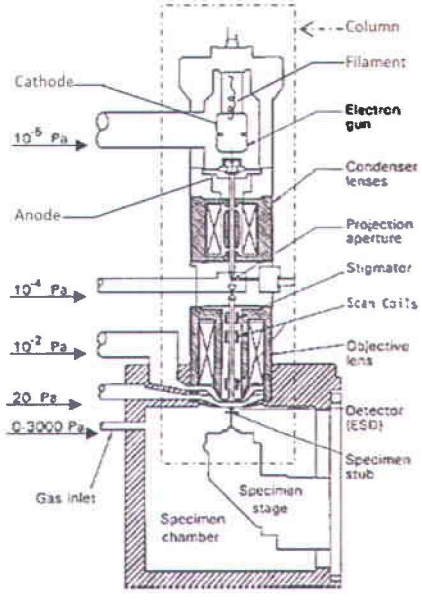

Figure 3.2 Schematic diagram of the Scanning Electron Microscope (SEM).

There are other imaging modes which are available in the SEM [61], for example, the specimen current imaging technique uses the intensity of the electrical current, induced in the specimen by the illuminating electron beam, to create an image. It is often used to detect subsurface defects. Back scatter imaging uses high-energy electrons that appear almost 180° away from the illuminating beam direction [58]. The back scatter electron yield is a function of the average atomic number of each point on the sample and backscattered electron images therefore carry information on the chemical composition. Scanning electron microscopes are often coupled with an x-ray analyzer. The energetic

electron beam interactions with the sample are often complex and may produce x-rays whose spectra are characteristic of the elements present in the sample. This characterization of the composition is called electron dispersive x-ray analysis or EDX. Processing in different ways the radiation emitted by the stimulated material (Figure 3.3) gives rise to several other imaging modes [58].

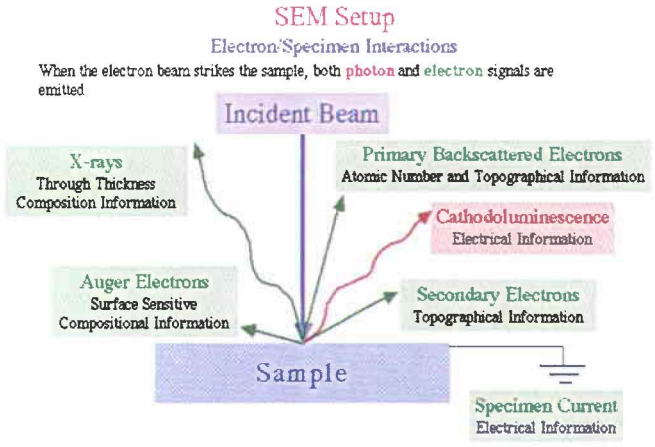

Figure 3.3 Sketch of the electron-specimen interactions.

3.2.3 Sample preparation for SEM

When a sample is not conducting or exhibits low conductivity, it is preferable to deposit a conductive layer on its surface. It involves depositing a thin layer of carbon, or of gold, with the objective of reducing charging as to maximize the resolution and to reduce the noise associated with SEM image formation. Since SEM uses electrons to create an image, conventional SEM requires samples which are electrically conducting. All metals are conductive and require no additional preparation [62]. The coating required to prevent charging on insulators must be continuous, electrically conducting, thin, and stable and have a high secondary emission coefficient. For imaging in the medium –high magnification range of 10, 000-50,000 X thin amorphous carbon or thin metal coatings of finer grain size are used to improve the surface contrast and to provide sufficient electrical conductivity. When charging is still an issue, we reduced the SEM accelerating voltage rather than increasing the coating thicknesses because the metal coating morphology may contribute to the image.

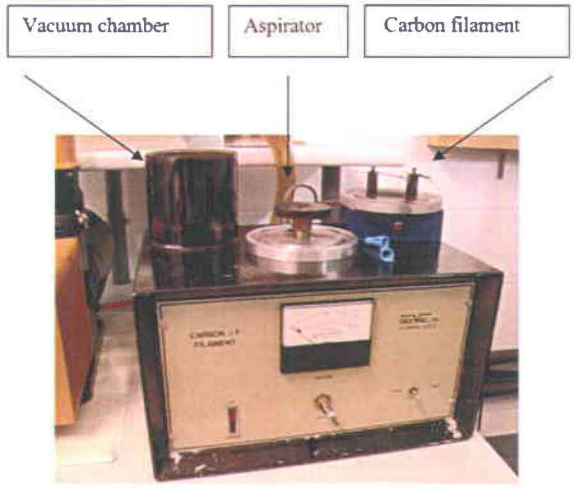

Figure 3.4 Sputter coater and its details.

Thin layers of a conducting material can be deposited by using a small device called a sputter coater. The sputter coater is a small vacuum chamber positioned with two electrodes, and a sample holder for carbonizing (Figure 3.4) that is fixed to a thin wire of carbon as a conductor between two electrodes. A vacuum is created in the chamber, to promote a current flow along the carbon wire. As a result, the wire sublimes into a carbon cloud which induces the deposition of a conductive layer on the sample surface (alternatively a very thin layer of gold could be deposited as well).

3.2.4 Setup and procedure for SEM

For the SEM analysis described in this work, we used a JEOL JSM-6300 Scanning Electron Microscope. The JSM-6300 basic unit (Figure 3.5) consists of an electron optical column (Figure 3.5.a); a main console (Figure 3.5.b), a control system, a power supply unit and a pump box. The main console incorporates a vacuum gauge, and the system consists of the control panel, the keyboard, and a display system. The power supply unit is located at the back of control and display [58]. The basic SEM is connected to an EDX unit, which displays the characteristic X-ray spectrum. Auxiliary elements, such as a cathodoluminescence (CL) detector, allowed us to use the full spectrum of light produced by the material. As soon as the removal of air is completed, and the column

reaches the required pressure (about 10^{-5} Torr for image observation) the emission of an electron starts. The specimen chamber can be viewed on the camera display located

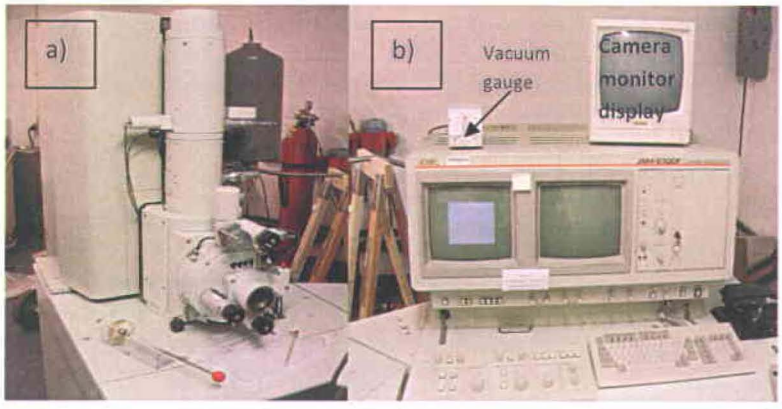

Figure 3.5 a) Electron optical column; b) Main control unit.

beside the vacuum gauge (Figure 3.5.b). The sample is fixed to a metallic base which is mounted on the specimen exchange rod (Figure 3.6). The latter is also introduced inside the specimen exchange chamber. The vacuum (low-pressure condition) required to operate the SEM is reached in about a minute.

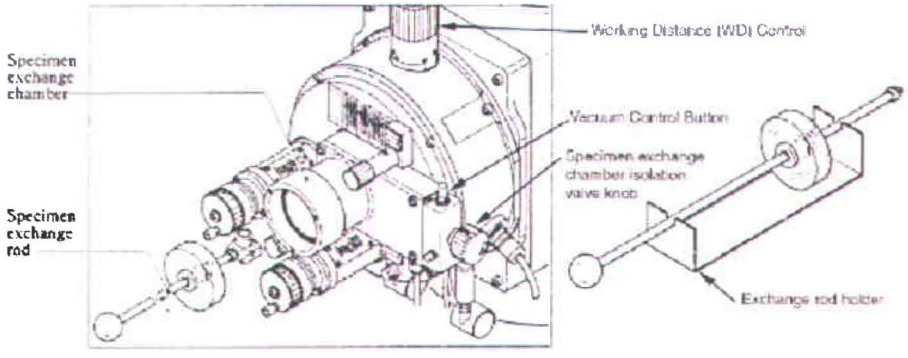

Figure 3.6 Details of the load-lock system for specimen insertion into the microscope.

Before starting the image acquisition, it is necessary to adjust the parameters, such as the accelerating voltage and filament heating current needed to image the topography, which are critical for optimal resolution. The accelerating voltage could be selected in 0.1 kV steps from 0.2 to 5 kV and in 1 kV steps from 5 to 30 kV respectively [58]. The filament discharge is usually found at 8 mA. After performing a gun alignment and an astigmatism correction, it is ready to acquire the image from the CeBiIG specimens. The most useful acquisition process is the secondary electron emission, which is the topography of the specimen.

3.3 X-ray diffractometry

3.3.1 Introduction to Crystallographic Studies

An important breakthrough in the study of the structure of matter followed the discovery of X-ray diffractometry (XRD). From basic research to industrial production and engineering, XRD is an indispensable tool for material characterization and quality control. Specifically, X-ray diffraction is a nondestructive method to get information about the crystalline structures of single crystals, ceramics, and thin films. X-ray diffraction can be applied to any crystalline and polycrystalline material, but the process is most sensitive to high-Z elements, since the diffracted X-ray intensity is stronger for heavier nuclei. The power of XRD lies in the enormous amount of information that can be extracted from the collected data. It can easily be used with a resolution in the angstrom range. However, the disadvantage is that the data has to be analyzed carefully, and the analysis is not always easy.

3.3.2 A brief history of X-ray analysis

For a longtime, mineralogists and crystallographers accumulated information about crystals and their internal structure with chemical analysis or by an indirect measurement of their physical properties. Such analysis revealed limited information about the real structure of crystal lattices. Significant progress came from the discovery that crystals have periodicity of about 1 to 2 Å, and that X-rays being electromagnetic waves with a wavelength of the order of 1Å could be used to investigate them. In the beginning of the 20^{th} century, the phenomenon of diffraction was finally understood by

the German physicist Von Laue (1879-1960) who identified how X-rays, and whose wavelength is comparable to the lattice spacing, are diffracted by the crystals. Following his intuition, the wave nature of X-rays and the periodicity of the atomic arrangement were soon confirmed. Two other physicists who analyzed his results made important contributions to the field, namely W. H. Bragg (1862-1942) and W. L. Bragg (1890-1971). The latter successfully interpreted the Laue experiments and identified the relationship between the X-ray radiation wavelength and the space periodicity of the atomic planes. Using X-ray diffraction, Bragg identified, for the first time, the structure of NaCl, KCl, KBr and KI. These were the first full crystal structures ever described [63].

3.3.3 Basic theory of diffraction

Diffraction occurs due to the existence of certain phase relationship between two or more waves, whereas interference results of the interaction of two electromagnetic waves with a fixed phase relationship between them. In interference, superimposition occurs between two different wave fronts coming from coherent sources while in diffraction, the superimposition of waves take place between the secondary wavelets from different points of the same wave front [64]. Interference is the fundamental process that causes diffraction. To understand this phenomenon, we introduce the "Young's experiment" (Thomas Young, ~1805) [64]. This study was originally arranged in an attempt to resolve whether light was composed of particles (the "corpuscular" theory) or consisted of various waves traveling together, as in sound. To answer this question, Young used a "double slit" arrangement (Figure 3.7). In this geometry a planar wave, created by a source of coherent light that impact a board with two slits. According to Huygens principle, if the width of the slits is small compared to the distance from the detector screen, we can consider the slits as two spherical light sources emitting in phase.

According to the above description, and considering only a one-dimensional problem for associating a field for each source, we have for the first slit,

$$E_1 = E_{01} \sin(\omega t - kz + \varphi_1) \tag{3.1}$$

and for the second one,

$$E_2 = E_{02}\sin(\omega t - kz + \varphi_2) \tag{3.2}$$

Using vectoriall sum of the two fields, then we have,

$$E_T = E_0\sin(\omega t - kz + \varphi) \tag{3.3}$$

where

$$E_0 = \sqrt{E^2{}_{01} + E_{02}^2 + 2E_{01}E_{02}\cos\Delta\varphi} \tag{3.4}$$

and

$$\varphi = arctg\frac{E_{01}\sin\varphi_1 + E_{02}\sin\varphi_2}{E_{01}\cos\varphi_1 + E_{02}\cos\varphi_2} \tag{3.5}$$

The phase and the amplitude of the resulting field are easily obtained from the basic rules of Vector algebra. As we know, the intensity is proportional to the square of the field amplitude. In Young's experiment, due to symmetry $E_{01} = E_{02}$, we can derive the following expression for the intensity: $I \propto |E_0|^2 = 4E_{01}^2\cos^2(\Delta\varphi/2)$, which describes the fringes observed on the detector screen.

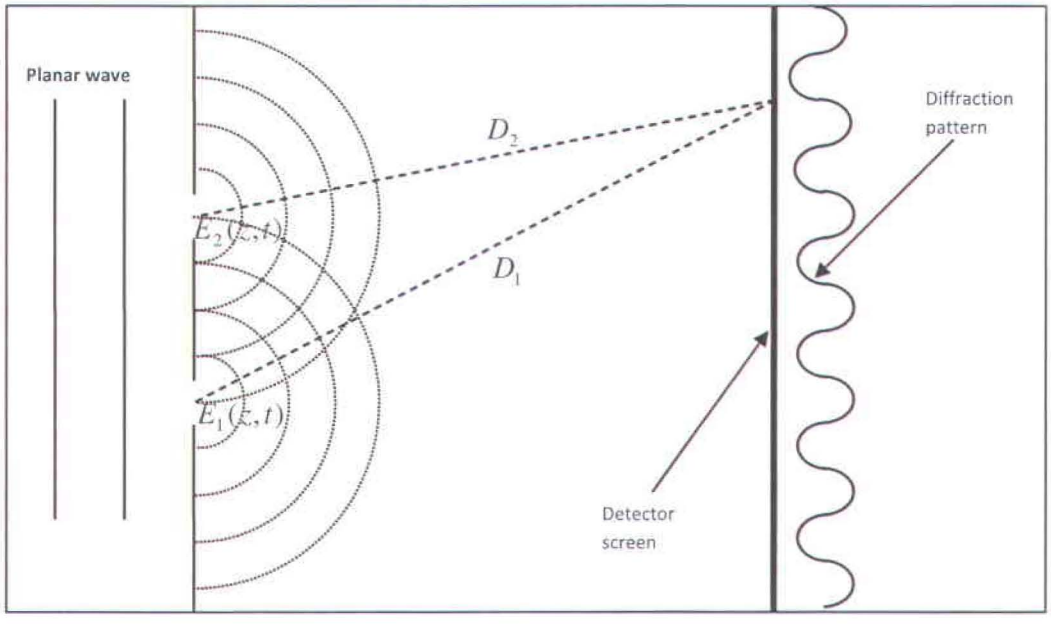

Figure 3.7 Schematic diagram of double slit experiment.

This nonuniform light pattern is due to the path difference between the two beams coming from the slits. The path difference can be clearly related to the phase shift by the relation:

$$\Delta\varphi = \frac{2\pi}{\lambda}(D_1 - D_2) \tag{3.6}$$

Where D_1 and D_2 are known as the distances from the first and the second source to a point fixed on the screen, and λ is the wavelength of the coherent light source.

It is possible to rightly infer from Eq, 3.6, if the path difference is equal to an integer multiple of the wavelength, the two beams will constructively interfere giving an intensity maximum on the screen. The opposite is true for a half wavelength distance. In an alternative experiment, where the two slits kept and are separated with a small aperture, in order to observe a pattern which resembles a *Sinc* function. In general, the diffraction pattern on the screen is mathematically related to the 'pattern' of the diffracting object by Fourier transform. For a crystal, the lattice structure can be determined through the X-ray analysis [63, 65].

3.3.4 X-ray diffraction and Bragg law

Information detailed so far may be concisely listed as:

a) A difference in the path length between two waves leads to a difference in phase.

b) Introducing the phase differences produces a change in amplitude.

c) A diffracted beam may be defined as a beam composed by various mutually interfering scattered rays.

The rules above can be applied to the X-rays scattered by a crystal lattice. As shown in Figure 3.8, we find two conditions related to the diffraction from a crystal lattice, The first one implies that constructive interference exists between the rays scattered from the same crystallographic plane. Consider rays 1 and 1a of the incident beam.

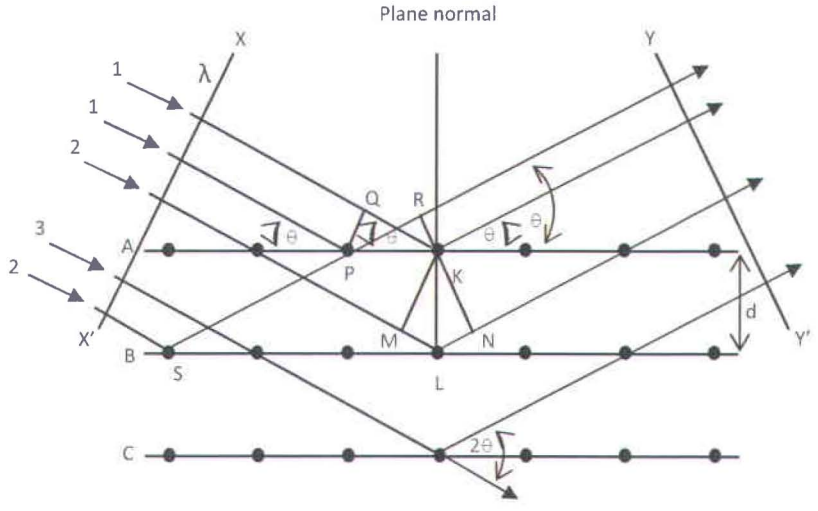

Figure 3.8 X-Ray diffraction by a crystal.

Atoms K and P scatter the rays in all directions, but constructive interference take place only along the θ direction, because of the path difference which is:

$$QK - PR = PK\cos\theta - PK\cos\theta = 0 \tag{3.7}$$

We find a similar relation for all the rays scattered by the atoms of the same plane in the same direction. The second and fundamental relationship of the diffraction among the rays scattered from different planes (Figure 3.8), can be written as:

$$n\lambda = 2d\sin\theta \tag{3.8}$$

Where, "n" is the order of diffraction and "d" is the distance between two crystallographic planes. This relationship was first formulated by W. L. Bragg and is known as Bragg's law. It states the first condition required to obtain diffraction. From the last formula, it can be seen that for fixed values of "λ" and "d", there may be several angles of incidence $\theta_1, \theta_2, ...\theta_n$ related to each order of diffraction [66].

The diffracted beam seems to be similar to the reflected one, with some fundamental differences:

a) For a reflective material, incident and reflected beams have similar energies and the diffracted beam is always stronger than a scattered ray, while it is considerably weaker than the incident beam.

b) Reflection occurs for each incident angle while diffraction occurs only for certain directions, which satisfy the Bragg law.

c) The reflection involves only the superficial atoms. Diffraction is built up of rays scattered by all the atoms of the crystal [64, 67, 68].

3.3.5 X-Ray Diffractometer Setup

The main part of the X-ray investigations is carried out with a Panalytical advanced diffractometer (Xpert Pro MRD -3040/60), using a Cu-K_α radiation source with λCu-$K_{\alpha 1}$ = 1.54056 Å, λCu-$K_{\alpha 2}$=1.5444 Å and λCu-K_β =1.3922 Å, operating at 45 kV and 40 mA. In a Panalytical X-ray diffractometer (Figure 3.9.a) and following issues are to be noted, a) prefix optics allows the configuration to be changed quickly to accommodate a wide range of data collection strategies. b) The diffractometer can be configured in the X-ray powder diffraction mode, grazing incidence X-ray diffraction mode, X-ray reflectometry mode, as well set in order to get information on the residual stress and texture. c) A 4-circle Euler Cradle is used in such a way that the sample always lies flat and does not move (the sample sizes can be as large as 60 mm in diameter with a thickness of 3-12 mm, which is sufficient to accommodate the CeBiIG samples).

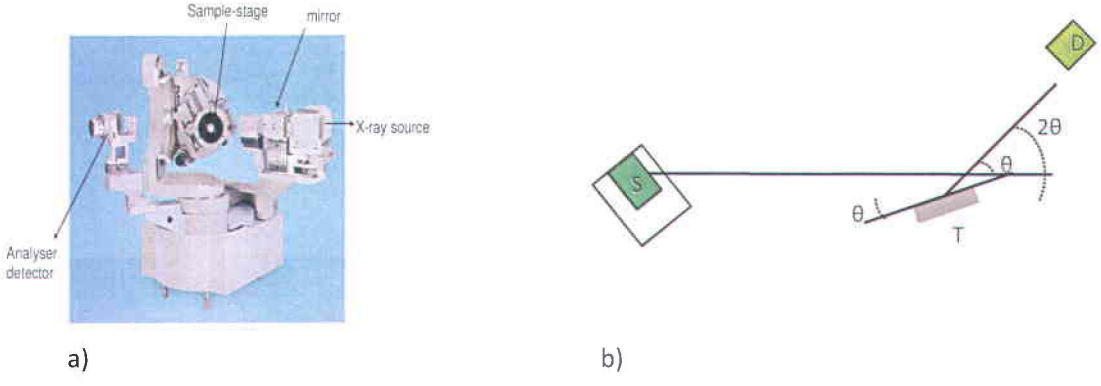

Figure 3.9 XRD a) Xpert Pro extended MRD system b) Bragg Brentano θ-2θ geometry.

We use a Bragg-Brentano θ-2θ measurement geometry (Figure 3.9.b) that can provide information about the crystalline orientation of the material in the growth direction (also called "out-of-plane" direction). It gives information about the inter-planar distances of the lattice planes parallel to the film surface. In our configuration, the incident angle θ is varied, and the detector angle for the diffracted beam varies simultaneously by an angle 2θ in a coupled manner.

A θ-2θ scan is usually performed over a wide angular range for obtaining the structural information. We choose a wide range 20°< 2θ<120°. Other relevant parameters are the angular step and the measurement time step which are fixed to 0.020° and 0.5 sec, respectively.

When a powerful electron (or ion) beam hits a Cu target and excites the Cu atoms to higher energy levels, the Cu atoms return to the fundamental state, and producing an X-ray radiation whose spectrum is shown in Figure 3.10(a). This radiation is diffracted by the sample and collected by a suitable detector, and finally analyzed by a computer. The Cu emission spectrum is formed by sharp peaks. The desired quasi-monochromatic collimated radiation for the XRD analysis can be obtained by using a suitable filtering system. The filter system is composed by two different slits as shown in Figure 3.10(b).

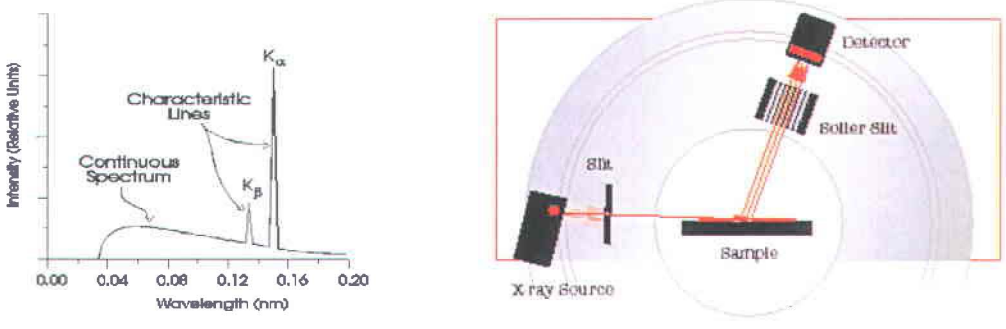

Figure 3.10(a) Spectrum of Cu emission *(b) Position of filter slits.*

The first slit is placed at the exit of the X-ray source. Its main purpose is to minimize the angular aberration. The second slit (Soller) is fixed in front of the detector to determine the intensity and shape of the peaks measured in the diffraction pattern.

Narrow Soller slits reduce the magnitude and also provide sharper peaks. Two typical spectrograms obtained with this configuration are shown in Figure 3.11 using an amorphous-SiO_2 material (a) and a quartz crystal (b).

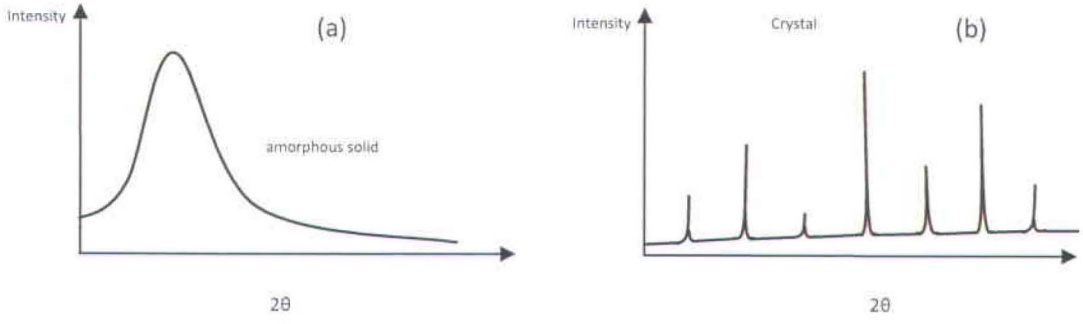

Figure 3.11 Comparison between X-ray scattered by an (a) amorphous solid SiO_2, and (b) a quartz crystal.

As stated earlier, an enormous amount of information can be gathered from a graph such as Figure 3.11.b. In particular, the three main characteristics of each peak, namely its position, width, and amplitude are discussed further below.

3.3.6 The angular position of the peak

From the angular position of a peak on the diffractogram, the crystal plane relates to a direction of diffraction can be identified. Therefore, we need to correlate the diffraction angle to a number of planes. This precise mathematical relation is obtained by combining the Bragg's law and the plane-spacing equation referred to as the hypothetical structure of a material. For example, by considering the simplest crystal structure, i.e. the cubic cell, we have the following two relations:

$$n\lambda = 2d\sin\theta \quad (n = 1 \text{ for first order diffraction}) \tag{3.9}$$

Eq. 3.9 represents the Bragg law for the first order of diffraction and

$$\frac{1}{d^2} = \frac{(h^2 + k^2 + l^2)}{a^2} \tag{3.10}$$

Eq. 3.10 represents the plane-spacing formula in a cubic lattice. Here, "d" is the distance between two adjacent atomic planes, 'a' is the lattice spacing, while 'h', 'k' and 'l" are

the Miller indices of the plane. Miller index is defined as the reciprocal of the fractional intercept formed by the plane with the crystallographic axis [64, 68].

Combining the above two formulae once can obtain the following relation:

$$\sin^2\theta = \frac{\lambda^2}{4a^2}(h^2 + k^2 + l^2) \tag{3.11}$$

Eq. 3.11 allows us to consider the plane associated to a specific direction of diffraction for the simple case of a cubic cell. The same principle applies to more complex structures, even though the plane-spacing equation gets more complex. Also, the XRD software can provide a theoretical spectrum for each known structure and relate the actual crystallographic plane to a given peak [69].

3.3.7 The angular width of the peak

The angular width of a diffraction peak increases as the thickness of the crystal decreases. For example, a small angular variation causes a path difference, and thus a phase shift, between the waves A and A' from two parallel planes at a distance $t = m \cdot d$ from each other. Here, 'm' is the number of atomic planes, and θ is the diffraction angle as shown in Figure 3.12. If 'm' has a high value, as it is for a thin film, the path difference can increase up to half integers of the wavelength, and the two waves can destructively interfere. On the other hand, this is not the case if 'm' has a small value: Although the diffracted waves differ from each other, for a small angle difference, they may not interfere destructively resulting in an increase in the angular width of the peaks. Hence, if the dimension of the crystal is too small, the angular width of the peak increases. Additionally we can notice a decrease of their amplitude due to diminution of the numbers of the diffracting planes.

In the worst case, if a grain size lies in the order of few nanometers it is difficult to obtain information from XRD technique. From the results we obtained with XRD and AFM, the order of the dimension of the grains in the current films is large enough to detect a noticeable diffraction using XRD.

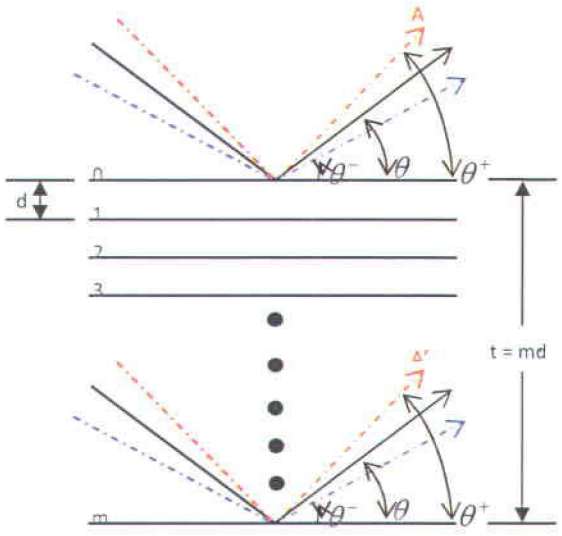

Figure 3.12 Effect of crystal size on diffraction.

Other causes can increase the width of the peak, (for instance, X-ray sources are not perfectly monochromatic, or the different crystal grains may have a slightly different orientation) making it hard to deduce significant information from the angular width. The following empirical equation is known as the Scherer formula,

$$t = \frac{0.9\lambda}{\Delta\theta \cdot \cos\theta} \tag{3.12}$$

where t is the crystallite size, λ is the incident wavelength, Δ is the full width at half maximum and θ is the position of the maximum of the peak. The Eq. 3.12 can be used to determine the particle size of extremely small crystals from the measured width of their diffraction curves [63, 65]. In addition, coherence lengths below 100 nm can be evaluated by the broadening of the peaks in θ-2θ.

3.3.8 The amplitude of the peak

Inferring all the possible information from the peak amplitude of a diffractogram is beyond the scope of this thesis. However, to complete the theoretical overview on XRD, we briefly explain the properties associated to peak amplitude. Consider two orthorhombic cells as shown in Figure 3.13; the cell on the left is base-centered, while the

cell on the right is body-centered. Consider the reflection from the (001) plane shown in the lower part of Figure 3.13.

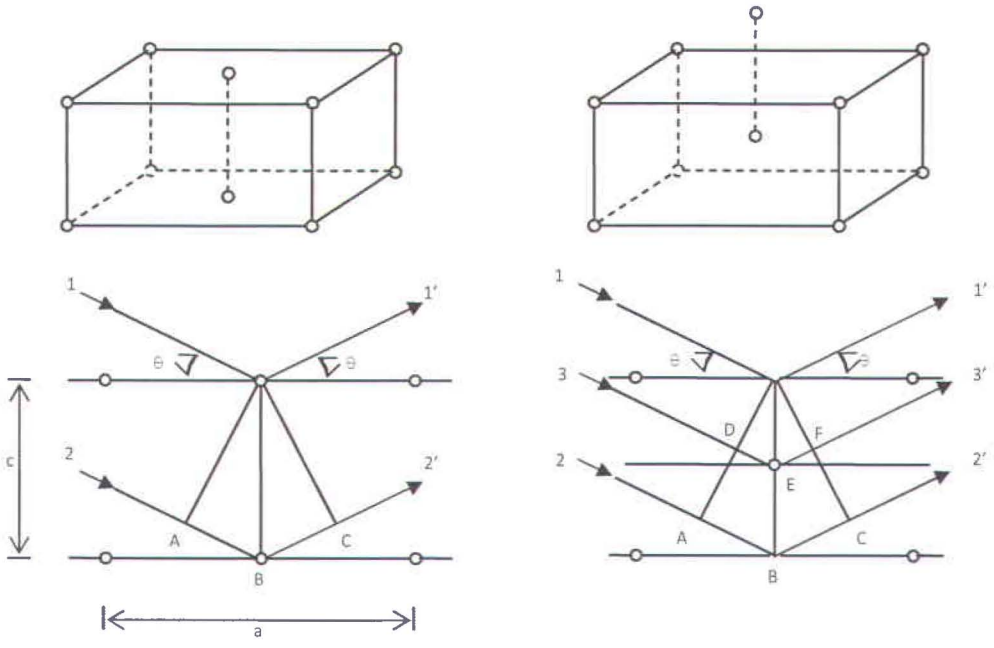

Figure 3.13 Sketch of base centered (on the left) and body centered (on the right) orthorhombic cells and their diffraction from the (001) plane.

The position of the atoms in the unit cell does not affect the diffracted beam. Also, if the Bragg's law is satisfied for the base centered lattice, we can formulate following interesting features:

i) The ray (1-1') is in phase with the ray (2-2') in the base centered case,

ii) The path difference DEF between ray (1-1') and ray (3-3'), in the body centered cell, is one-half wavelength, and leads to destructive interference.

From this example, it is clear that even a small change in the atomic arrangement can eliminate reflection from a crystal.

The intensity of a diffracted beam can be changed by varying the atomic positions, and vice versa. We can in principle determine atomic position and composition by observing diffraction peak intensities. However, to establish an accurate relationship between atom position and intensity is a complex problem. To solve this problem, we need to consider how X-rays are scattered by a single electron, as well as by an atom, and finally by all the atoms in the unit cell [63, 65].

3.4 Atomic force microscopy (AFM)

3.4.1 Introduction to AFM analysis

Microscopes are classified into two main categories: optical and electron microscopes. These microscopes are based on producing a magnified image of an object by focusing radiation on its surface. The magnification depth of two-dimensional image varies from 1,000 X for optical to 100,000 X for electron microscopes. However; they do not explore vertical dimensions of an object, nor its height and depth [70].

The atomic force microscope (AFM) uses a sharp probe to magnify surface features. With the AFM, it is possible to image the surface topography with an extremely high magnification, up to 1,000,000 X.

3.4.2 Brief history of the atomic force microscope

Atomic force microscopy (AFM) is part of a scientific discipline called scanning probe microscopy. AFM was invented by Gerd Karl Binnig, Christoph Gerber and Calvin Quate in 1986 [71]. The first AFM performed only in contact mode. In contact mode, the tip mounted at the end of a flexible cantilever, raster scans the surface of the sample [71]. The deflection of the cantilever, due to tip-surface interaction, reveals valuable information on the sample surface, most importantly its topography. Non-contact procedure, introduced in 1987, is used to examine soft material samples because they are difficult to examine using contact mode. In non contact mode the cantilever oscillates, close to its resonant frequency at a small distance (1-10 nm) above the surface [71]. Because the forces on the sample are much lower than in contact mode, even the ultra soft samples can be imaged without damage.

Another important step in the development of AFM came in 1991 when micro fabricated tips were developed. Smaller cantilevers were produced in 1996, allowing higher resolution and smaller scanning times. Cantilevers range in lengths from 9 to 40 nm with high resonant frequencies [72, 73]. New models also include an integrated illumination source, essentially combining an optical microscope and an atomic force microscope in the same piece of equipment. Today scientists are studying the super-microscopic structures, e.g. of living cells, using AFM [71, 74, 75].

3.4.3 General theory of AFM

In the AFM system a sharp tip, (Figure 3.14) located at the free end of a cantilever, probes the surface of a sample. The force applied to the cantilever varies depending on the tip-sample distance. The sample-tip interaction can be measured by various ways, the most common being an optical system. A repulsive force dominates at small interatomic distances, and it increases exponentially with decreasing tip-sample separation, while an attractive force (the Van der Walls force) dominates at larger separations [75, 76]. In AFM, the interaction of the tip and the sample surface can be classified as repulsive or contact mode, attractive or non-contact mode, and tapping mode.

3.4.4 AFM in contact mode

In contact mode of scanning, the AFM tip makes a soft touch with the sample which is connected to a piezoelectric positioning element. As the tip moves closer to the sample surface, the repulsive interatomic forces become particularly strong and dominant. Since the cantilever has a low-spring constant, the forces with a mean value of 10^{-9} N will cause the cantilever to bend, following the topography of the sample. Therefore, the detection of the position of the cantilever, typically made by an optical system, leads to a topographic map of the sample surface [75-78]. We advance the discussion in two parts. The AFM system can provide the topographic data operating in one of the following two modes:

a) Constant -force operation mode (Figure 3.14),
b) Constant –height operation mode (Figure 3.15),

In the constant-force operation mode, (Figure 3.14) the variation of the cantilever deflection can be used directly to generate the topographic data [75-77].

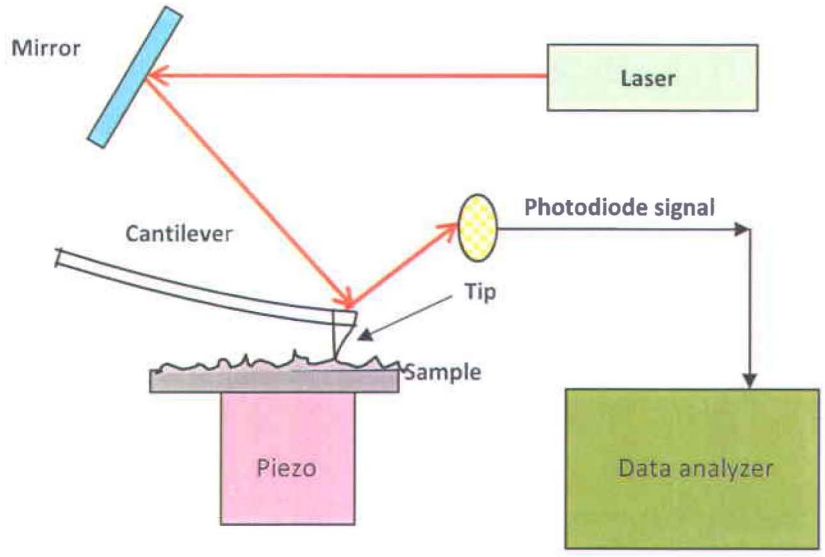

Figure 3.14 AFM contact mode (constant-force setting).

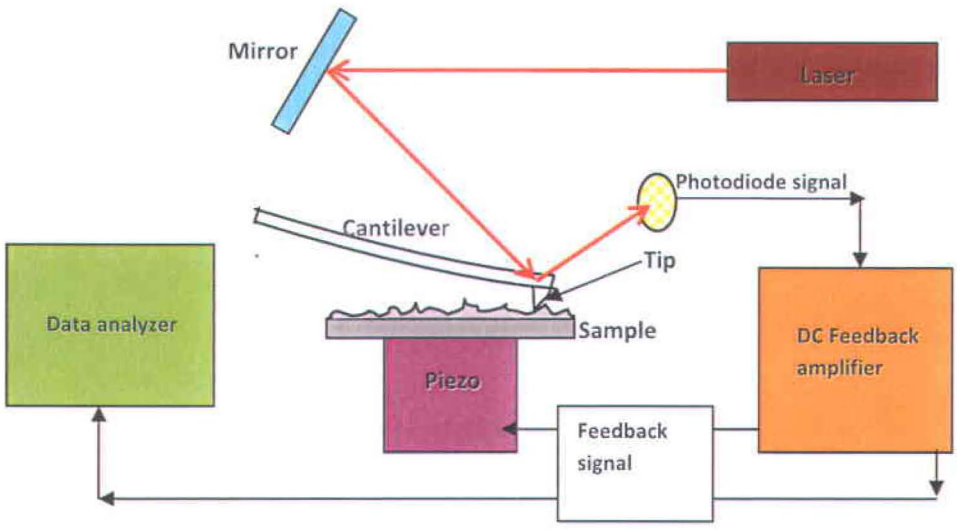

Figure 3.15 AFM contact mode (constant-height setting).

In constant -height setting, (Figure 3.15) the deflection of the cantilever is detected and compared in a DC feedback amplifier to some desired value of deflection (corresponding to a determined height). If the measured deflection is different from the desired value, the feedback amplifier applies a voltage to the piezo control to raise or lower the sample relative to the cantilever and the desired value of deflection (constant height). In this operation mode, the voltage applied by the feedback amplifier to the piezo is a measure of the topography of the features on the sample surface. Constant-height mode is preferred for those applications where the softness of the sample imposes a small constant pressure of the cantilever on the sample surface [75].

3.4.5 AFM in non contact mode

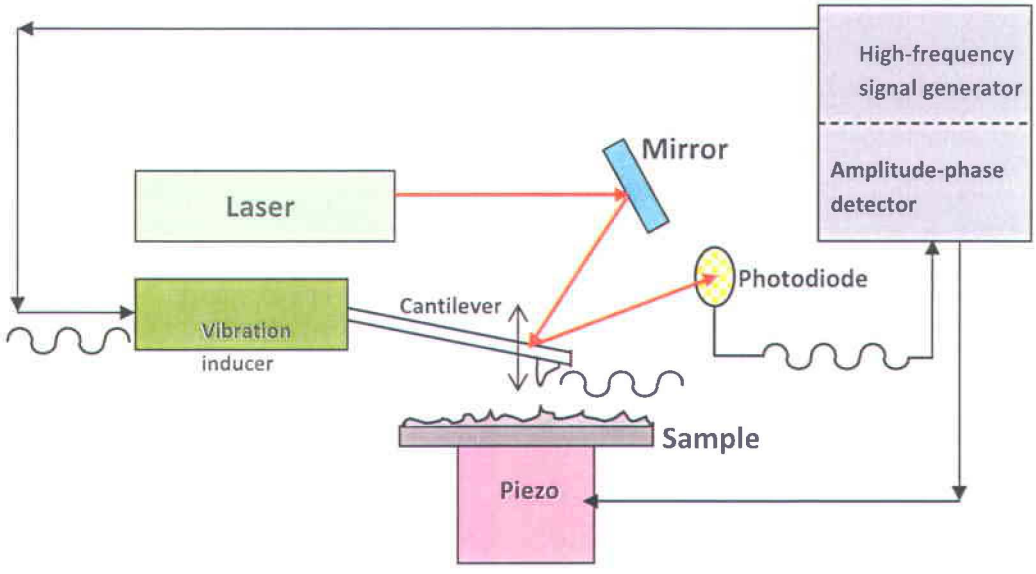

Figure 3.16 AFM non contact mode setup.

In non contact mode, (Figure 3.16) the cantilever, under the action of an alternating voltage, vibrates close to the surface of the sample. The distance between the tip and the sample is of the order of tens of nanometer. The non-contact mode is used to study ultra-soft or elastic samples like biomolecules [75-79]. The system vibrates a stiff cantilever near its resonant frequency (typically in a range of 40 to 280 kHz) with

amplitude of a few tens of nanometer. When the tip-sample distance varies, small changes in the resonant frequency or vibration amplitude are detected, because of the variation of the tip-sample interaction, more precisely of the weak, attractive Van der Walls forces. In this scanning mode, we use a feedback system which keeps the resonant frequency or vibrational amplitude of the cantilever constant (therefore keeping the tip-to-sample separation constant) and the feedback signal is used to create the image.

The resonant frequency of the cantilever varies as the square root of its spring constant, and the spring constant varies with the force gradient applied to the cantilever, itself depending on the tip-sample distance. Therefore, the changes in the resonant frequency induce variations in tip-sample distance which can be used to measure the sample topography.

3.4.6 AFM in tapping mode

The tapping scanning mode (similar to Fig 3.16) alternately places the tip in contact with the surface and then lifts it off. This technique overcomes problems associated with friction, adhesion, electrostatic forces, and other difficulties by avoiding the tip dragging across the surface and still providing the high resolution associated with the contact mode. Note that the tapping mode is implemented in ambient air. The cantilever is set in oscillation at (or near) its resonant frequency, using a piezoelectric crystal. The piezo motion causes the cantilever to oscillate with a high amplitude (typically greater than 20 nm) when the tip is not in contact with the surface.

The Oscillating tip is then moved toward the surface until it begins to gently tap the surface. During scanning, the vertically oscillating tip alternately contacts the surface and then lifts off, at a frequency of 50 to 500 KHz. As the oscillating cantilever begins to contact the surface frequently, its oscillation amplitude is automatically reduced due to energy loss caused by the tip contacting the surface. The reduction in oscillation amplitude is used to identify and measure surface features [75-78]. During tapping mode operation, the cantilever oscillation amplitude is held constant by a feedback loop [75-78].

3.4.7 Magnetic Force Microscopy (MFM)

Magnetic force microscopy (MFM) is a versatile technique [80, 81] that images magnetization patterns with submicron resolution. It is used for imaging magnetic field gradient distribution and magnetic domains. Most importantly MFM images the spatial variation of magnetic forces on a sample surface. Usually MFM tips are coated with a Co-Cr, NiFe alloy or a ferromagnetic thin film. The principle of operation is based on non contact atomic force microscopy (NC-AFM). This is done by scanning a magnetized atomic-force-microscope (AFM) tip over the surface with the tip vibrating perpendicularly to the surface. In this method [80, 81], changes in the resonant frequency of the cantilever induced by the magnetic fields (depending on the tip to sample separation) will be detected by the laser/photo detector setup. The magnetic probe is a standard silicon cantilever (or silicon nitride cantilever) coated by magnetic thin film. A MFM image is obtained by recording local frequency variations as a function of tip position. In MFM, a two pass technique (Figure 3.17) is normally employed. In the first pass, the topography is determined in contact or semi contact mode. In the second pass, the cantilever is lifted to a selected height of 50-100 nm for each scan line (or after topography measurement by gently tapping the tip along the surface) and scanned using the stored topography. In the second pass measurement, the tip sample separation is kept constant for eliminating the Van der Waals forces. Therefore, using MFM, it is possible to measure both height image and the magnetic images [80, 81].

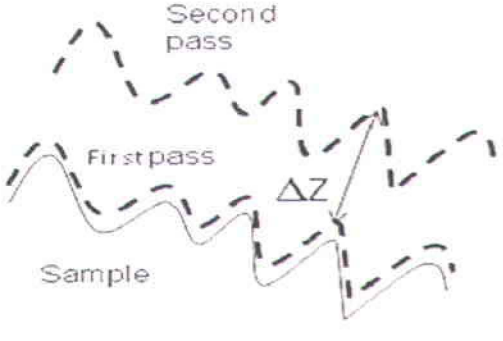

Fig 3.17 Schematic representations of a two pass technique using MFM.

The images taken with a magnetic tip contains information about both the topography and the magnetic properties of a surface. The dominating effect usually depends on the distance of the tip from the surface, because the interatomic magnetic forces persist for greater tip to sample separations than the Van der Walls force [80, 81]. If the tip is close to the surface, the image is topographic. With the increase in separation between the tip and sample, the magnetic effects become apparent. In order to separate magnetic nature from topographic effects, we need to procure a series of images at different tip heights. The magnetic images have a strong dependence on tip properties [80, 81].

One disadvantage with hard magnetic coating of the tip may affect [80, 81] the magnetic structure of the sample, and vice versa; sample magnetic field can reverse the magnetization of the tip. To avoid problems, we can exclude the first pass which can be achieved by measuring without feedback. Hence the measurements are executed with constant Z –coordinate of scanner. Following precautions should be exercised while using MFM; i) the data analysis of MFM images is not as straightforward as for other techniques. Since MFM probe generates magnetic stray fields, a determination of the sample magnetization (which is nonlocally related to the stray fields due to the long-range dipole-dipole interaction) may require calculations (ii) The magnetic field of the tip may alter the domain structure in magnetically soft materials, and (iii) an external magnetic field can change the magnetization state of the tip so that MFM would be operated in zero fields [80, 81].

3.5 Magneto optical characterization

The evaluation of the Faraday rotation in magneto-optic materials is extremely important, and in fact, the present thesis evolved from an earlier idea to synthesize a new garnet material whose properties could allow the fabrication of the first fully integrated optical isolator.

The Faraday Effect is usually responsible for the splitting of specific energy levels of the material under investigation. The different levels so obtained interact differently with the right-handed and left-handed polarizations of light. The clockwise and counterclockwise propagating waves experience a different refractive index (circular

birefringence). These physical effects can be detected by looking at the polarization rotation (the Faraday rotation) of a linearly polarized beam which passes through a stimulated magneto-optic medium. To estimate the magnetically induced rotation, an experiment in transmission geometry was configured as shown in Figure 3.18.

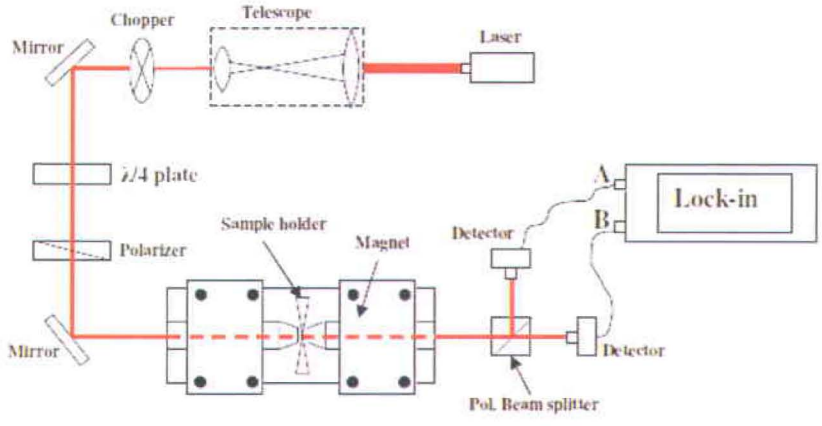

Figure 3.18 Schematic of the experimental framework for measuring the Faraday effect.

The experimental setup can be summarized as follows: A diode laser emits a beam at 1550 nm that first passes through a 45° polarizer and then through a magneto-optic sample which is placed between the two pole pieces of an electromagnet, in a steady magnetic field parallel to the beam itself. The beam emerging from the crystal is directed to a polarization cube splitter which separates the "s" and "p" components and directs them separately to two photodiodes. Finally, the differential signal sensed by the detectors is measured by a lock-in amplifier synchronized with the chopper that is located at the laser output. In the absence of magnetic field (Faraday Rotation = 0), the beam reaches the cube splitter still linearly polarized at 45°, producing a differential signal equal to zero, since the "s" and "p" components are equal in magnitude. When the magnet is activated, a rotation of the linear polarization is induced by the Faraday Effect, the "s" and "p" components are unbalanced, and a nonzero differential signal ΔV is detected by the lock-in amplifier. Finally, by using the following Eq (3.13) (where V_A+V_B is the sum of the voltage amplitudes as recorded at the lock-in channels) in

conjunction with Eq (1.9) it is possible to reconstruct the plot of the Faraday Rotation per unit length as a function of the applied magnetic field (Figure 3.18).

$$\frac{\Delta V}{V_A + V_B} = \sin(\vartheta_F) \tag{3.13}$$

The choice of the differential arrangement is due to the sensitivity desired in this measurement. From Eq (1.9) it is clear that the Faraday rotation is proportional to the film thickness, which in our experiments never exceeds 1μm. Thus, the magnetically induced rotations are extremely small, sometimes of the order of a few percents of a degree. The minimum rotation angle measurable by using our experimental setup is limited by the background noise (mostly because of laser instabilities), resulting in a resolution of 0.002°.

3.6 X-ray photoelectron spectroscopy (XPS)

The X-ray photoelectron spectroscopy (XPS), also known as ESCA (Electron Spectroscopy for Chemical Analysis) was developed by Kai Siegbahn [82] and his collaborators in Sweden. The principle of XPS operation is described in the following;

A material under vacuum is subjected to photo excitation by X-rays which cause electrons to be ejected from the core electronic levels of the atoms in the sample. When an X-ray of energy hω penetrates the surface of the sample and is absorbed by an electron of binding energy E_B, the electron is then emitted into the vacuum [82].

The kinetic energy of the emitted electron is E_{kin}, and the whole process can be expressed by the following Eq 3.14,

$$E_{kin} = h\omega - E_B - (E_{vac} - E_F) \tag{3.14}$$

where E_B is the binding energy of the electron in the atom (a function of the atom and its environment), hω is the photon energy of X-ray source, E_{vac} is the energy of an electron at an infinite distance in vacuum and E_{kin} is the kinetic energy of the emitted electron that is measured with XPS spectrometer.

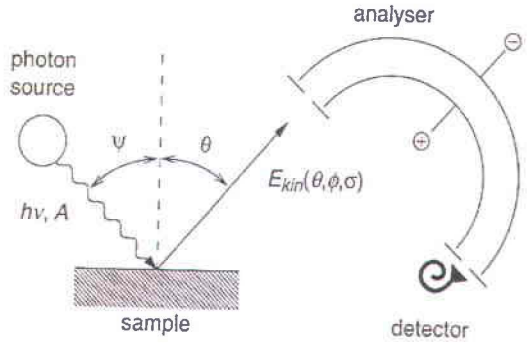

Figure 3.19. Sketch of photoelectron emission and detection. Photons with energy hν are emitted from a source (Al-Kα) and hit the sample surface at an angle ψ with the surface normal. Photoelectrons are generated in the sample and the kinetic energy of the emitted electrons E_{kin} is determined using an electrostatic analyzer [82].

The energy distribution of the photoelectrons depends on the energy distribution of the electron states in the solid surface. The process is influenced by other phenomena that may occur (plasmon excitations, electron excitations, electron correlation effects) and the photon absorption probabilities are not the same for all electron states. The binding energies are measured with respect to the (E_F) Fermi level. The energy of the X-rays from the source is known, and the kinetic energy of the emitted electrons can be measured; therefore, the binding energy E_B can be determined. Since the value of E_B for the core electrons of an element is typical to that element, XPS can provide an extensive, elemental analysis of the material under investigation. Since the elements of a compound are characterized by different binding energies in the electron shells, the chemical state of the sample constituents can also be determined. Typically, the XPS spectrum provides chemical information of the sample volume 20 to 100 Å below the surface, depending on the nature of the specimen and the incident angle of the X –ray beam [82].

Chapter 4

Results and discussion of magneto-optical CeBiIG epitaxial thin films

In this fourth chapter, it is described on the experimental results and discussion on optimization procedure, morphology, structural and magneto-optical properties of CeBiIG films, a new magneto-optical material synthesized and characterized during this study. This novel material (CeBiIG) is bismuth and cerium co-substituted iron garnet and its Faraday rotation per unit thickness has been estimated to be the highest in its category.

4.1 Sample preparation

The technique adopted for growing the CeBiIG thin films was Pulsed Laser deposition (PLD). The deposition processes was performed using a KrF-excimer laser operating at a wavelength of 248 nm (described in paragraph 2.3.1). The laser was set with a repetition rate of 20 Hz and focused onto a stoichiometric ceramic target for ablation. Before the deposition, the substrate was heated to 600°C for thermal cleaning of the surface and the temperature was kept at 680-700°C while the deposition was performed. During the film growth, a laser fluency of 3.5 J/cm^2 was maintained, and the target of $Ce_{2.2}Bi_{0.8}Fe_5O_{12}$ was set at a distance of 5.5 cm from the gadolinium gallium garnet (GGG-111) single crystal substrate (dimensions of 10 mm x 10 mm x 0.5mm).

The choice of GGG as a substrate was driven by the necessity to minimize both the lattice and thermal expansion mismatch, in order to enable epitaxial growth. For our deposition of films, the substrate to film lattice mismatch is ≈1.9% (Reference lattice constants: YIG = 12.377Å, GGG = 12.378Å, $Bi_3Fe_5O_{12}$ = 12.63A°) while the mismatch between the thermal expansion coefficients is below 10% (Reference thermal expansion constants: YIG = $10.4x10^{-6}$/°C, GGG = $9.2x\ 10^{-6}$/°C). In addition, GGG has excellent transparency and low Faraday rotation, which simplifies the magneto-optical characterization of the films [11, 27, 28].

After film deposition, the ramping process is completed in three steps. The whole process was carried out in an argon atmosphere (200-350 mTorr) with a deposition rate of

0.25-0.36 nm/s to achieve 0.9-1μm thick CeBiIG films at the end of the process. More details will be presented in the next section of optimization procedure.

4.2 Thickness Measurement

The physical thickness of the film was measured by a profilometer Decktak, Veeco Instruments Inc. In this measurement, a mechanical stylus probe made contact with the sample surface to detect the film profile. The profile is established by scanning the probe across an artificial sharp step, which is obtained by partially masking parts of the substrate surface during the deposition. The thickness is measured over the step. The accuracy of this instrument is ± 50 Å. In our analysis, the thickness of CeBiIG films ranged from 0.9 to 1.0 μm. While measuring thickness, caution should be exercised when probing rough surface samples because the Decktak obtains data with sensitive diamond tipped stylus. Sometimes the display line goes flat or the maximum vertical scan size is too low, in this case repositioning the sample and turning off the power switch (on/off) will minimize the problems associated with measuring thickness of the samples.

4.3 Details of the processing parameters and optimization procedure

In the present investigation three gas ambients were used in the deposition of CeBiIG samples namely oxygen, reduced atmosphere and argon and the pressure of these gases was varied in the range of 100-500 mTorr. The PLD method comprises the following steps for synthesizing CeBiIG thin films.

a) A KrF excimer pulsed laser (Lambda Physik, 248 nm wavelength 17 ns pulse width) operated at the energy density of 3-3.5 J/cm^2 and a repetition rate of 20-25 Hz has been utilized to ablate a stoichiometric target.

b) The deposition of film (sputtered by laser pulses) on the substrate in argon takes place and during the deposition the substrate was kept at 680 ±20°C.

c) A cooling with a rate of 10°C/min down to 400°C is utilized in order to achieve thin films of the right structural CeBiIG phase.

d) Subsequently, an in-situ annealing for 40 minutes (dwelling) at 400°C is performed. This annealing process was chosen (duration of 40 minutes and temperature ramp of 10°C/min) to crystallize the amorphous (as deposited) layers

into a high quality nanocrystalline garnet phase and obtained a grain size of 100-170 nm. The choice of the in-situ annealing was dictated by both, the need to prevent oxidation of cerium into the Ce^{4+} state, and to avoid loosing bismuth, an element which is extremely volatile, as experimentally observed during the ex-situ annealing. Therefore, in-situ method enables the formation of the right CeBiIG phase.

e) A last cooling down to room temperature at the same rate of 10°C/min is performed as shown in the Figure 4.1 and summary of the related processing parameters are given in table 4.1.

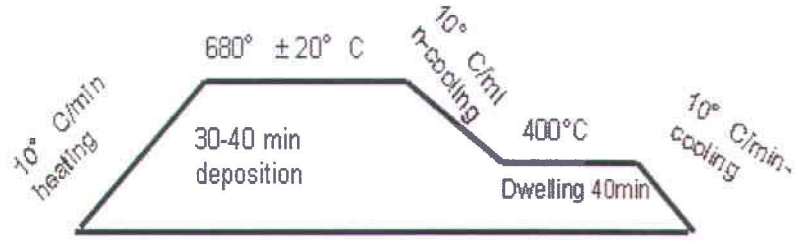

Figure 4.1 Schematic diagram for Epitaxial CeBiIG film growth and annealing procedure.

Table 4.1 Deposition Parameters of CeBiIG epitaxial films

S.No	Deposition-Parameters	Experimental condition
01	Substrates	GGG(111)
02	Atmosphere	O_2/Ar+H_2/Ar
03	Distance between substrate & target	5-5.5cm
04	Repetition rate	20-25Hz
05	Fluency	3J/cm^2
06	Pressure	100-500mTorr
07	Temperature	680°C
08	Deposition time	40-60 minutes
09	Deposition rate (nm/sec)	0.25-0.40

In the present studies, well controlled stoichiometry has been achieved for CeBiIG garnet films using PLD. This is not a trivial task because a wide range of physical properties were studied for the first time in this composition. In particular different treatments in various pressures on epitaxial nature were studied and a detailed explanation is given in the following and some of the processing parameters are given in table 4.1. In depositing epitaxial garnet films, we studied the role of substrate temperature and different partial pressure of gases for the formation of epitaxial films. First, we studied the role of the ambient gas.

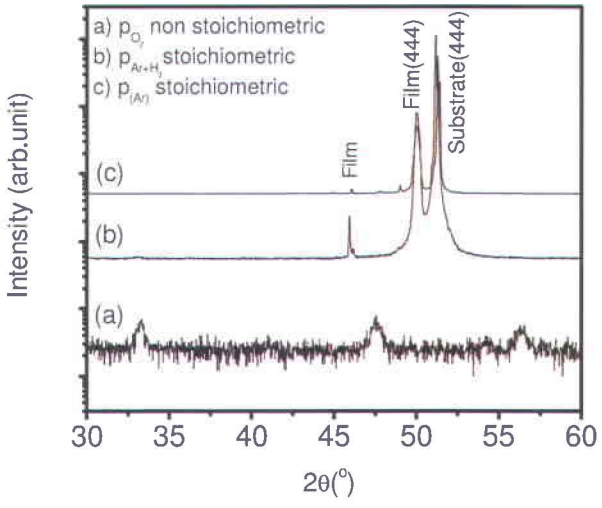

Figure 4.2 Out of plane X-ray diffraction spectra obtained for CeBiIG thin films deposited under an atmosphere a) 200 mTorr of oxygen, (the films deposited under oxygen CeBiIG contain several phases and are sometimes amorphous and spectra can not be indexed), b) 200 mTorr Ar + H_2, and c) 200 mTorr of Ar.

The nature and pressure of the ambient atmosphere has been varied in the range 50-500 mTorr. The substrate temperature was varied between (680±20)°C. The X- ray diffraction and energy dispersive X --ray spectroscopy were performed on these films. As shown in Fig 4.2, from these experiments, we found that these films are not single phase and suffer from oxygen deficiency in their stoichiometry. Subsequently we increased the oxygen partial pressure during the deposition of these films, which resulted in structural degradation (multiphase). Therefore, oxygen pressure is not useful in providing the

appropriate stoichiometry and crystal structure at those partial pressures. In the next step, the effect of reducing atmosphere was studied. The reducing ambient gas consisted of Ar+H_2 with a ratio of 1:5. The pressure was varied from 100-500 mTorr and the substrate temperature varied between 680 -700°C. The X-ray diffraction results are shown in Fig 4.2. Note that there are clearly resolved film and substrate peaks observed at $2\theta=50^{\circ}$ and 51° respectively. These peaks are representative of the crystallographic structure of epitaxial CeBiIG films.

The more prominent structures can be visualized with the increase in argon pressure from 300-350 m Torr as shown in the following Figure 4.3, where we can see a clear (111) orientation.

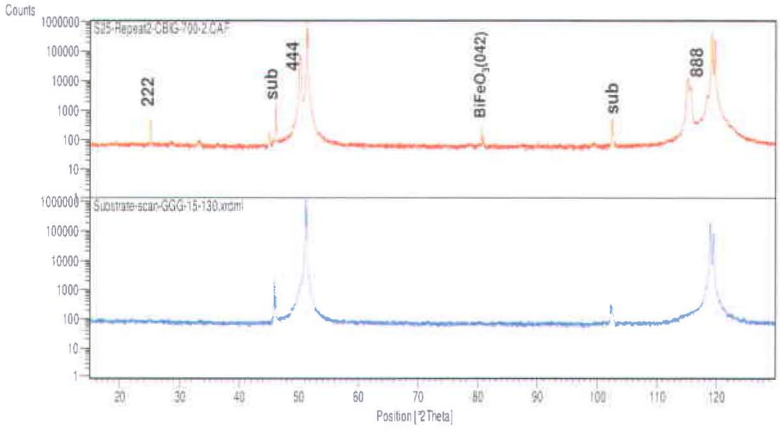

Figure 4.3 Out of plane X-ray diffraction spectra obtained for the layers deposited CeBiIG (under 300 mTorr of Ar) on substrates of GGG (111) (red) and one for the GGG substrate (blue).

The well resolved film and substrate peaks are presented in red and blue colours respectively in the same Figure. From energy dispersive X-ray spectroscopy, we confirmed the correct stoichiometry of these films (note that the film composition should conform to the target stoichiometry of bismuth 4%, cerium 11%, iron 25%, and oxygen to be 60% in all the deposited CeBiIG epitaxial films). The composition ratios CBi/CFe= 0.14, and CCe/CFe= 0.46 were both found to be close to the target stoichiometry.

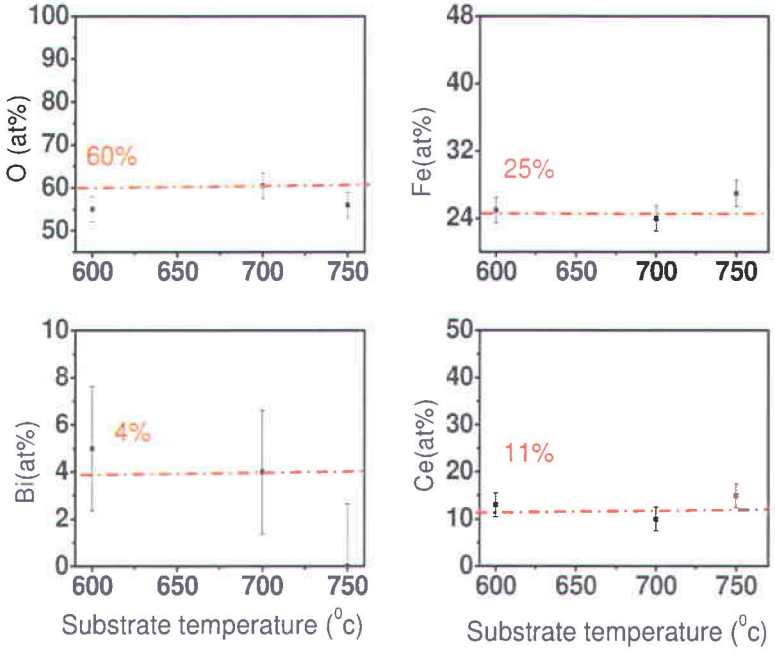

Figure 4.4 Atomic concentrations versus substrate temperature for CeBiIG films.

The PLD and post annealing procedures used in this investigation preserve the stoichiometric composition of the target in the deposited films. The crystalline state of the film is significantly related to the argon gas pressure used, since the latter controls the energy of the plasma particles. For instance, those films grown in a low argon pressures resulted in poor crystallinity. This might be because of the decrease in oxygen content in the film composition. It has been speculated that it is because of the different characteristics of the elements vapor pressures in the ablation plume and the different sticking coefficients that also influence the properties of the deposited films [26-28]. At higher Ar gas pressures gas phase collisions between the ablated species and background gas molecules reduce the kinetic energies, allowing to tune the energy distribution [26-28]. Additionally, to circumvent the bismuth evaporation problem, the samples were deposited in a high pressure of argon.

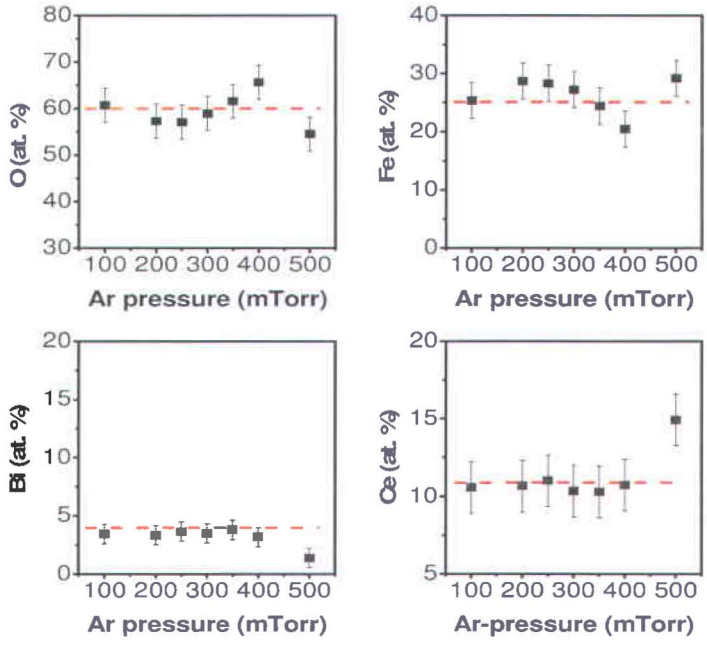

Figure 4.5. Atomic concentrations of the elements constituting the CeBiIG with Ar pressure during the growth of thin films.

The reactant gas required for phase formation depends in general on the thermodynamic stability of the desired phase. Therefore at low-pressure (less than 150 mTorr) for the different gas pressures, crystalline films were hardly obtained because of nonstoichiometric composition of the deposited films as shown in Figure 4.5. Significant differences have been recognized between the film and the target composition. Similarly at 400 m Torr of argon pressure, as well as increasing Ar pressure, a noticeable deviation from the desired stoichiometry is observed and this proves that beyond 400 mTorr, it is difficult to obtain a good microstructure of the CeBiIG films. This information has been graphically displayed in the Figure 4.5, where the red line showed the correct stoichiometry close to that of the target. Finally to conclude this section, it is revealed that, for films deposited at a temperature 750°C and above, a notable deviation from stoichiometry is revealed as shown in Figure 4.4. Same finding was observed for the films deposited at pressures exceeding 350 mTorr argon. This suggests that the choice of parameters is important to obtain good stoichiometry for the films as shown in Figure 4.5 (the red line indicates the expected stoichiometry for the target CeBiIG). The Bismuth

content was found to be particularly sensitive to deposition conditions and annealing temperature. All CeBiIG films dispalyed nearly stoichiometric composition. Prior to the structural characterization, the sample compositions were identified through EDX (Energy dispersive X-ray analysis) compositional analysis. An EDX spectrum normally displays peaks corresponding to the energy levels for which the most X-rays have been received. Each of these peaks is unique to an atom, and, therefore corresponds to a single element. The composition is shown in the following table 4.2 for four epitaxial CeBiIG films grown at different Ar pressure.

Table 4.2 Stoichiometric composition of BiCeIG films

Sample-Icode	Oxygen	Iron	Cerium	Bismuth	Deposition Pressure mT(Ar)
1	57.05	28.30	11.00	3.65	350
2	58.94	27.23	10.34	3.49	250
3	54.52	29.18	14.93	1.37	300
4	58.68	25.92	11.56	3.84	300

Furthermore, the films deposited in-situ were better crystallized than those annealed ex-situ. This is because the films grown in air were cracked and had a reddish brown colour where as the film deposited in an argon had greenish colour without cracks. When the annealing was performed ex-situ, the oxygen rich samples may take extra oxygen from the air and the samples possess excessive oxygen, which is not suitable in our case. Hence, we rely upon in-situ annealing only. Moreover, we didn't observe the cracks from the in-situ annealed films due to the high mobility of the evaporants on the film surface. When the argon gas was used as ambient gas, the oxygen that was released from ablated target played an important role in controlling the charge state of the cerium. The argon gas prevents premature oxidation, as shown from our studies on chemical analysis.

It should also be noted that different processes of sample synthesis in thin film form may lead to the fundamental differences in the way the oxygen and cation vacancies are created and hence may lead to change in the properties. The samples prepared at low $P_{O2}/P_{Ar+H2}/P_{Ar}$ < 100 m Torr have oxygen vacancies that must lead to the formation of multiphase samples as it is evident from XRD. Similarly samples grown higher than 100 mTorr of various gas pressures have shown the appropriate stocihiometry as presented in

Figure 4.5. The detailed morphology and structural analysis using argon ambient is presented in the next section.

4.4 Morphology and structure of CeBiIG epitaxial films

The sample preparation is done by mounting the object on a metal stub and gently placing it in an evacuated sample chamber. SEM images are collected (Figure 4.6 a-d) for CeBiIG thin films using an accelerating potential of 5 kV and a magnification factor of 50,000-100,000.

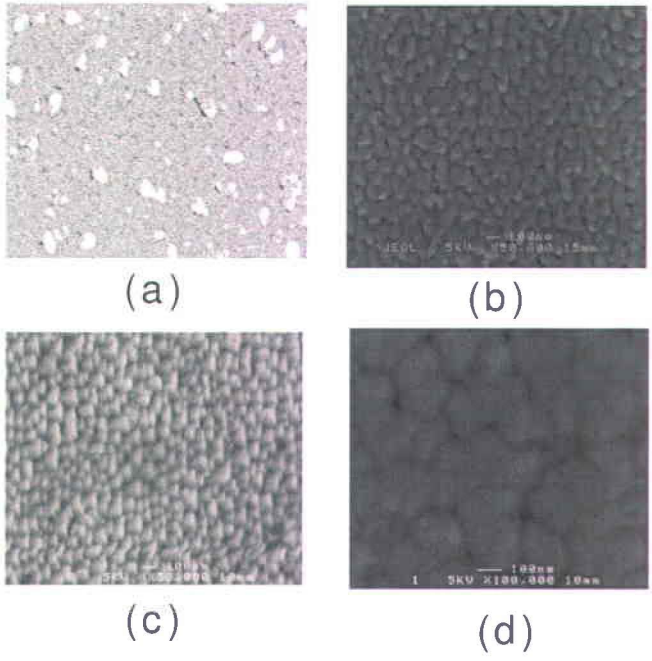

Figure 4.6. SEM images of CeBiIG films deposited at a) 250, b) 300, c) & d) 350 mTorr of argon.

The charging effect, caused by a large secondary electron decay time (with respect to the scanning time) [83], can be observed in the Figure 4.6 (a) as black and white spots. Further, the charging effect can be reduced by using a low-acceleration potential and a thin carbon coating as shown in Figures 4.6(b)-(d). The images show smooth and homogeneous surface without any cracks and lumps.

The SEM pictures of these films indicate that higher argon pressure produces a smoother film grown at 350 mTorr with a slightly larger grain size as compared to lower argon pressures.

Using X-ray diffraction in all its fundamental configurations (θ-2θ scan, ϕ-scan, and ω-scan), an in-depth structural investigation was performed. Figure 4.7-a shows on XRD, θ-2θ scan (using CuK_α 1.541Å radiation) for a 1μm thick CeBiIG thin film grown on a 0.5 mm thick GGG (111) substrate.

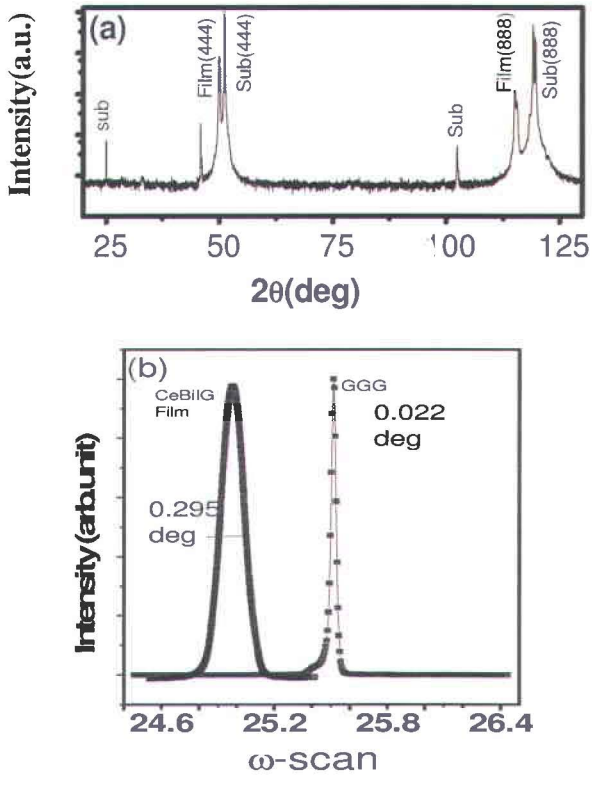

Figure 4.7 (a) Out of plane texture- XRD spectrum of a CeBiIG epitaxial film deposited on a (111) oriented GGG substrate in an argon atmosphere of 350 mTorr. (b) Mosaicity (FWHM) of the CeBiIG 444 reflection and GGG 444 reflection.

The θ-2θ scan (see Figure 4.7-a) shows only reflections from the (*h h h*) planes (*h* being an integer), proving that the film is (111) oriented in the growth direction. By comparing the experimental diffractogram with the theoretical one for the garnet structure (not reported in the image), it is found that CeBiIG reflections broaden and

shift towards lower angles. This is caused by the strain induced by the single crystalline substrate, as commonly observed in epitaxial thin films with small lattice mismatch between the substrate and the film perpendicular to growth direction. The lattice parameters were found to be 12.47 ± 0.005Å. From the Scherer's formula the grain size found to be 117-160 nm with increase in argon pressure.

In Figure 4.7-b, it is seen that the ω-scan (FWHM-rocking curve) of both the 444 peak of the CeBiIG films and the GGG substrate are well resolved. The width of the peak Δ(2θ) in radians, at half of its maximum intensity is a measure of the size of the crystal grains. This is because a larger stack of planes contributing to destructive interference at off Bragg angles results in a sharper Bragg peak as described by the Scherer formula. The full widths at half maximum, for the substrate and the film, were evaluated to be 0.022 and 0.295 arc-sec respectively. In the present case the width of the rocking curve exceeds the instrumental broadening by a factor of ten showing that the film possesses small angle grain boundaries and indicated a good growth direction of (111).

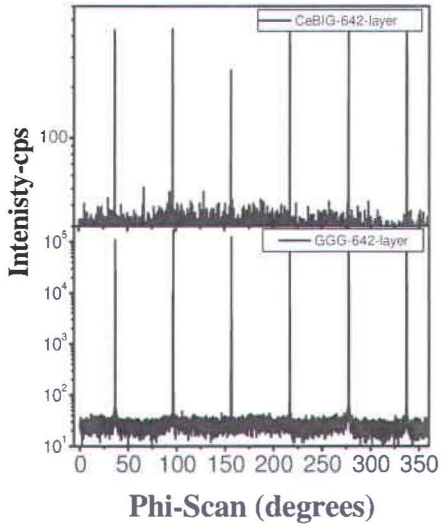

Figure 4.8 In plane texture (φ-scans) of both CeBiIG 642 and GGG 642 reflections for an epitaxial CeBiIG (111)/GGG (111) film deposited in an argon atmosphere at 350 mTorr.

Figure 4.8 shows the φ-scans of the 642 reflections of both CeBiIG and GGG for a (111) oriented CeBiIG/GGG (111) epitaxial thin film. This analysis provides information on the azimuthal orientation of the grains in the film plane. In our experiment, the φ-scan of the CeBiIG (642) reflection displays six equally spaced peaks (six-fold symmetry) at

the same angles for the film and the substrate, suggesting that the film is epitaxial and well oriented in the substrate plane.

The XRD analysis therefore proves the epitaxial nature of our CeBiIG films. Though CeBiIG layers are strained because of the lattice mismatch as well as the different thermal expansion coefficients associated with CeBiIG and GGG, we did not observe any cracks in the SEM as reported in Figures 4.9-a. This result is not uncommon for PLD films where the high kinetic energy of the vaporized materials increases the mobility of the deposited atoms on the film surface resulting in more homogeneous film morphology. Here the lattice constant of the garnet film is larger than that of the substrate, the film is under compressive stress and this induces a negative uniaxial anisotropy that favors the in plane magnetization state as found with the magnetic characterization presented in the following.

Magnetic force microscopy characterization is performed to show the presence of magnetic domains. In a typical experiment, both sample surface morphology (Figure 4.9-b) and magnetic field gradient (Figure 4.9-c) are detected and the local microstructure and the magnetic domains can be correlated.

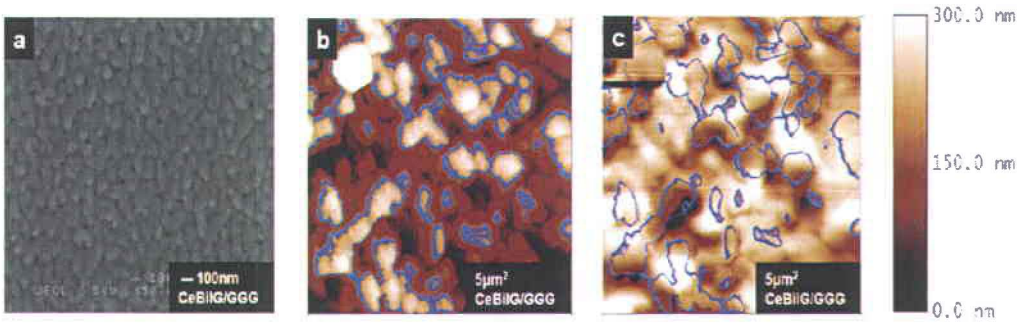

Figure 4.9 SEM image of a CeBiIG film deposited on GGG (111), showing a high-quality film displaying a smooth surface without cracks (a), AFM topographic profile (b) and magnetic force gradient (or MFM) contrast (c) images of the same thin film where the blue contours identify the magnetic domains. It is clear that the magnetic domains are somewhat correlated with the topographic features.

The topography (Figure 4.9-b) shows a relatively rough surface (40 nm rms measured over an area of 5 μm^2) with grains having a lateral dimension of 200 nm. The MFM contrast of the same area is revealed in Figure 4.9-c. Specific topographic features are marked with contour lines to better describe the two images. Although, the magnetic domains are strongly influenced by topography due to high-surface roughness, a careful analysis of the MFM contrast reveals a clear dipolar fingerprint, proving the existence of magnetic domains in the investigated samples. Also, the characteristic size of the features in the MFM images is about 150-200 nm suggesting that the magnetic domains extend over several grains as expected for soft magnetic materials.

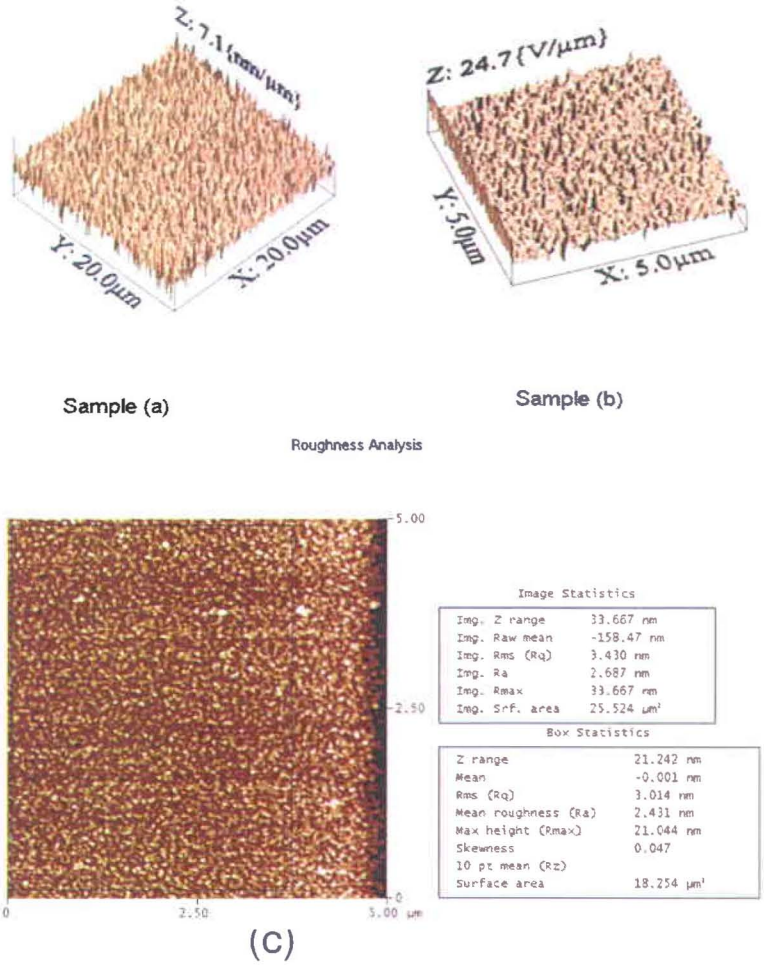

Figure 4.10. AFM images of CeBiIG films treated with a) 350 mTorr Ar exhibiting a mean roughness of 2.531 nm and b) 300 mTorr Ar exhibiting a mean roughness of 2.653 nm; c) Image statistics of the former film.

All the results reported in this chapter are promising features to develop a new, high quality magneto-optic material, and we believe there is still room for further improvement in the fabrication process that can increase the crystal quality while reducing surface roughness.

The AFM measurements conducted on CeBiIG samples grown at different Ar pressures are shown in Figures 4.10(a)-4.10(b).

The AFM image matches well with the SEM image of the CeBiIG sample deposited under Ar at a pressure of 350 mTorr. The morphology of the CeBiIG films reveals a loose structure of faceted grains with an elongated shape and voids in between. The roughness of these films is in the range 2.5-2.6 nm as shown in Figure 4.10 (c). The lateral grain size is found to be 110-200 nm (AFM) for the films deposited at 680 ± 20°C.

Table 4.3 Grain size estimation of CeBiIG epitaxial films

Samples Ar-Pressure (mTorr)	XRD Grain-Size(nm)	SEM Grain-Size(nm)	AFM Grain-Size(nm)	Roughness (nm)
200	100	117	150	1.89
250	117	122	110	1.23
300	120	140	200	2.64
350	140	160	200	10.36

To conclude this section, the grain size was measured using SEM, XRD, AFM and observed a variation in the measured grain size (table 4.3). The SEM, AFM grain sizes are measured by the distances between the visible grain boundaries, and XRD gives the extension of the crystallites that diffracts the x- rays coherently. The observed variation is a common factor when we measure the grain size with different instruments for the analysis of thin films. Furthermore, a graphic summary of the processing parameters explored gives rise to the following phase diagram:

4.5 Phase Diagram

In an effort to understand the mechanism of the crystallization process and to produce the highest quality of the CeBiIG films, we have studied the effects of different

pressure conditions and annealing procedures. It can be seen from the phase diagram (Figure 4.11), depositing above the optimized temperature (750°C) results in an excessive vaporization of the volatile constituents, especially Bi, which is the element substituting for Yttrium in iron garnet materials. After, optimization in argon we reached a near stoichiometry of the elements present in the target. The optimized window for several physical properties associated with achieving a giant Faraday rotation is presented in this phase diagram. The phase diagram clearly explains the efforts in producing excellent epitaxial CeBiIG films with a narrow window (rectangle-region) of deposition parameters. It was also, confirmed that argon pressure between 200 and 375 mTorr and the temperature 680±20°C are the main influencing parameters in depositing the CeBiIG epitaxial films on GGG substrates. In conclusion, the combined effect of the growth rate and substrate temperature on the crystallinity of the as deposited films can be explained by following processes: Atom ordering, tending to reach a state of minimum energy promoted by the substrate temperature and disordering of atoms caused by high pulsed material flux ablated from the target that impinges on the growing film. Therefore, competition between these two processes determines the structure and morphology of the as deposited films.

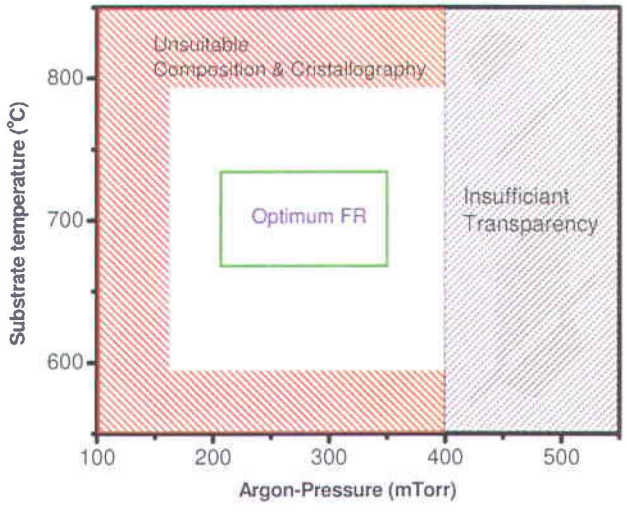

Figure 4.11 Phase diagram of epitaxial CeBiIG films (Transmittance, Faraday rotation and optimized regions along with unsuitable crystallography are clearly marked).

4.6 Chemical composition of CeBiIG films

XPS is measured using a VG-Scientific-ESCALAB 220 iXL spectrometer with an Aluminum twin source of 400W (polychromatic source) using AlK_α (1486.6 eV) radiation. The spectrometer is calibrated to the position of the Au $4f_{7/2}$ orbital (binding energy of 84.0 eV). The vacuum pressure in the chamber is maintained below 2 x 10^{-10} Torr. The spot size for the XPS study is about 0.5 x 1.0 mm. The pass energy for the survey is set at 100 eV, while it is set at 20 eV for the high-resolution spectrum.

The XPS deconvolution process consists of an analysis of the spectrum for a given compound. By recording a highly resolved spectrum in a stipulated energy range, it is possible to identify the chemical environment of the element. The chemical environment gives information about the oxidation state and the way the specific atom is bonded to other elements. Each spectrum is composed of the sum of all the peaks coming from the chemical state of the individual atoms in their specific environments. The XPS spectrum is analyzed using Casa-XPS software with the Shirley algorithm [84, 85].

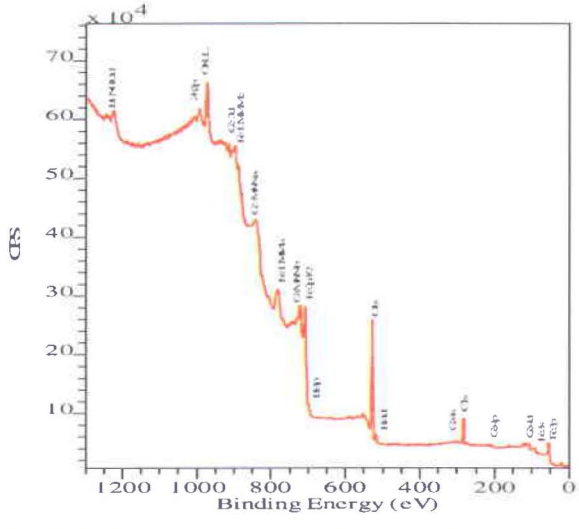

Figure 4.12 XPS-Survey spectrum of CeBiIG/GGG (Ar-350 mTorr).

A typical overall XPS survey spectrum is presented in Figure 4.12 for a global view of the primary species contained in a CeBiIG sample obtained with the deposition and annealing parameters optimized. A more detailed analysis can be performed, by making

the XPS spectrum of these films, into four distinct parts: i) the bismuth related spectrum, ii) the oxygen spectrum, iii) the iron spectrum, and iv) the cerium spectrum.

In the bismuth spectra, the doublet related to $Bi4f_{7/2}$ and $Bi4f_{5/2}$ peaks of bismuth oxide [86] appears at 159.09 eV and 164.4 eV, respectively as shown in the Figure 4.13.

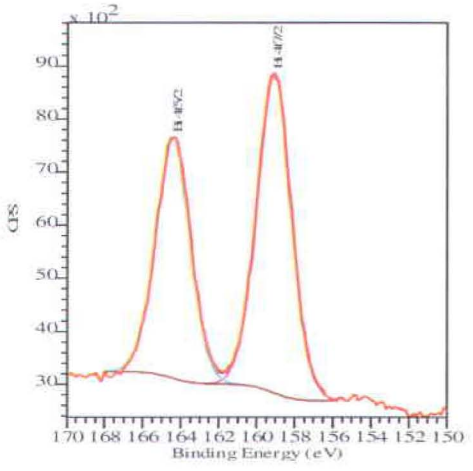

Figure 4.13 XPS core-level Bi-spectrum with curve fitting with bismuth doublets.

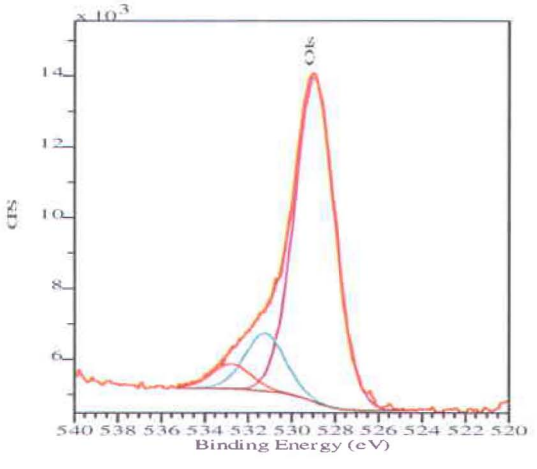

Figure 4.14 XPS core-level Oxygen-spectrum with curve fitting.

For the O_{1s} spectrum, the two main binding energy peaks are found at 532.4 eV and 528.95 eV, shown in Figure 4.14 which is in agreement with the literature reports [86-90].

Regarding the Iron spectrum, the Fe 2p response confirms the literature reports with two binding energy peaks at 709.4 and 717.3 eV that can be assigned to $Fe_{2p3/2}$ and $Fe_{2p1/2}$ of the pure Fe spectrum [87] (Figure 4.15).

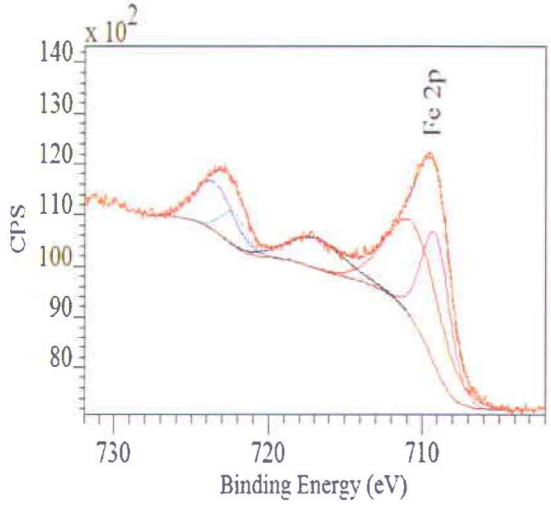

Figure 4.15 XPS core-level Fe-spectrum with its components after curve fitting.

The area of the $Fe2p_{3/2}$ peak was constrained to be twice the area of the $2p_{1/2}$ peak as suggested by quantum theory [88, 89]. Additional constraints on the fitting parameters were that the tail parameters of G/L ratio of the $2p_{1/2}$ main peak had to be equal to those of $2p_{3/2}$ and that the satellites had to be purely Gaussian. However, the iron spectrum appeared to be shifted down with respect to the standard one. This observation also agrees with the literature on the subject [88, 89].

Finally, for the Ce spectrum, 6 well-defined peaks related to the Ce-3d orbital positions are detected. The Ce-3d peak measured for CeO_2 contains three main $3d_{5/2}$ features at 882.9 (v), 889.2 (v″) and 898.5 eV (v‴) and three main $3d_{3/2}$ features at 901.3 (u), 907.6 (u″), and 916.8 eV (u‴) respectively (Figure 4.16).

The high binding energy doublet v‴ and u‴ are assigned to the $4f_0$ final state. Also, the v″, v and u″, u doublets are referred to final states with strong mixing of $4f_1$ and $4f_2$ orbital arrangements for the Ce3d spectrum [90-92]. The doublets splitting of 18.1 eV is in reasonable agreement with standard data [86].

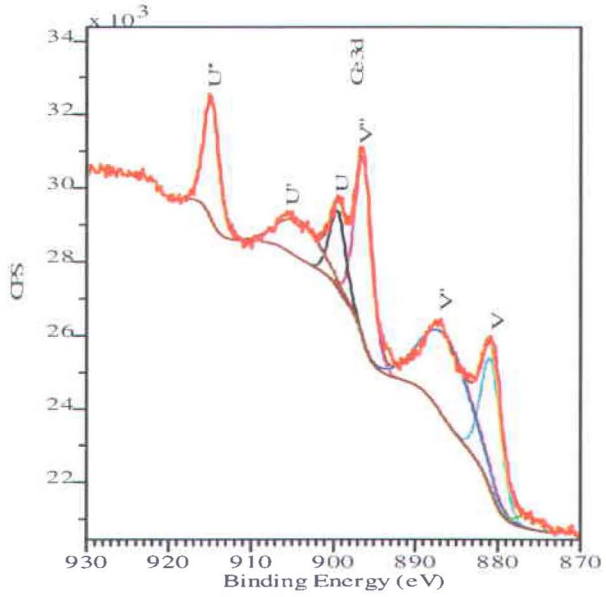

Figure 4.16 XPS core-level Ce-spectrum and its multiplets with curve fitting (for details please refer to the text).

From the measured Ce Spectrum, (Figure 4.16) the v and v″ peaks are related to Ce^{+4} valence states while the v′ peak is characteristic of Ce^{+3}. The presence of features related to Ce^{+4} and Ce^{+3} are found to be consistent with several reports [90-92].

In conclusion, the XPS study established the Cerium and Bismuth valence states. We have showed that the CeBiIG films are not contaminated by other atomic species, and that Cerium valence exists in two states of Ce^{3+} and Ce^{4+}. Iron and bismuth states (3+, 5+) are confirmed and consistent with the existing literature on the subject [86, 88, 90-92]. The atomic constituent's ratio of CeBiIG films is equal to that of the target within ±10% error limit. However, from the EDX analysis, the stoichiometry (composition) is found to be close to that of the target.

4.7 Magneto-optical analysis of CeBiIG epitaxial films

All the magneto-optic measurements reported in this work neglect circular dichroism. Circular dichroism corresponds to the tendency of certain materials to absorb in a different way right-handed and left-handed polarized light [93]. Because of circular

dichroism, the beam at the output of the sample is not linearly but rather elliptically polarized, thus inducing an error in the magneto-optic measurement. Ellipticity is negligible due to off diagonal elements in the matrix (defined earlier) are near to zero, when we consider the transmission geometry. Hence, it is negligible for CeBiIG thin films.

The plots (a), (b), and (c) shown in Figure 4.17 are the curves of the Faraday rotation per unit length as a function of the applied magnetic field amplitude "H" in Tesla. These plots are obtained from a series of CeBiIG epitaxial films deposited under different argon pressure conditions, where the (small) magneto-optic contribution from the GGG substrate (Figure 4.17-d) is removed after fitting. The Faraday rotation spectrums have been measured at 1.55μm with a sample thickness of ~ 1μm. As observed in Fig. 4.17, the Faraday Rotation is measured to be 0.55°/μm, a reasonably high value, while a saturation field of ≈ 0.3 Tesla and a Verdet constant (that correspond to the slope in the linear region) of 2072°/T*mm [6].

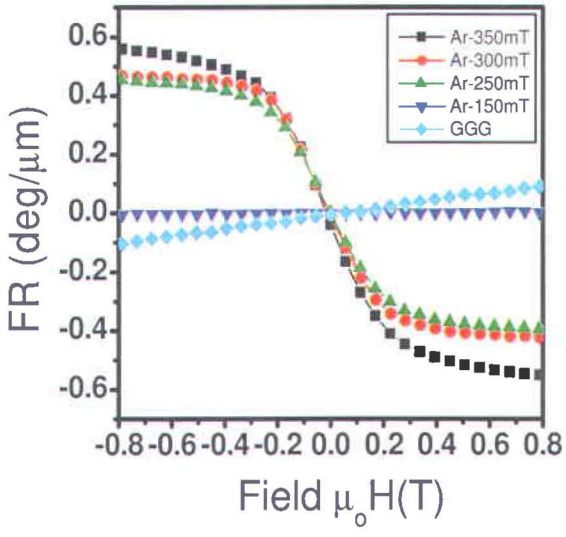

Figure 4.17 Faraday rotation per unit length @ 1550 nm as a function of the applied magnetic field for epitaxial CeBiIG films deposited on (111)-oriented GGG substrates for different argon pressures: (a) 350 mTorr, (b) 300 mTorr, (c) 250 mTorr (thickness 1 μm), and (d) for the GGG substrate (thickness 0.5 mm).

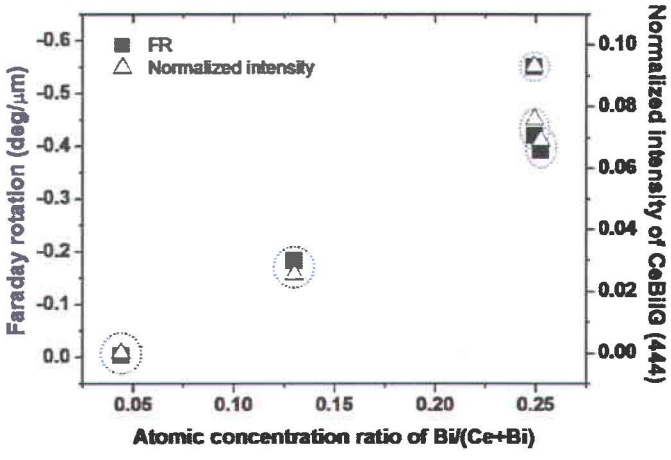

Figure 4.18 Absolute value of the Faraday rotation (■) and crystallinity (Δ) for CeBiIG films as a function of the atomic concentration (EDX-stoichiometric) ratio of Bi/ (Ce+Bi). The degree of crystallinity (Δ) is estimated from the normalized intensity (after fitting) of the CeBiIG (444) XRD peak $I_{CeBiIG\,(444)}/I_{GGG\,(444)}$. The target Bi composition is x = 0.8.

The remarkable Faraday rotation with the low value for the saturation field, and the possibility to integrate this material on a silicon-platform [94], led us to believe that this new garnet could be a material with high enough Faraday rotation to be a suitable magneto-active material for realizing future integrated optical isolators.

In Figure 4.18, both the Faraday rotation and the degree of crystallinity of CeBiIG films are shown for four different argon pressures, leading to different Bi and Ce film compositions, although the target Bi concentration is fixed at x = 0.8. The magnitude of the crystallinity is determined by the peak intensity $I_{CeBiIG(444)}$ of the (444) diffraction plane of CeBiIG, normalized with respect to the peak intensity $I_{GGG(444)}$ of the gadolinium gallium garnet substrate for the same diffraction plane. Figure 4.18 shows a correlation among the crystallinity, the magneto-optic activity, and the concentration of Bi ions measured in the epitaxial CeBiIG films.

A Bi concentration x = 0.8 for the target stoichiometry is established to be optimal both in the improvement of the magneto-optic activity of the material and the crystal structure. We believe that the addition of the Bi^{3+} ions into the dodecahedral sites of Ce-substituted iron garnet favours the formation of the magneto-optical active Ce^{3+} ions due

to charge compensation [94, 95] and enhances the Faraday Effect. On the other hand, the improved crystallinity of the material can be related to minimizing the lattice strain because of the differences in the ionic radii of Bi^{3+} (1.03 Å) and Ce^{3+} (1.01 Å) in the CeBiIG film. The site preference for the different cations in the lattice is essentially determined by their ionic radius [96].

Further studies are in progress to interpret these effects in depth and establish their respective contribution to the MO properties of the thin films under investigation. In the literature giant MO response in garnets was interpreted using the electronic structure and properties of materials in terms of possible vacancy-induced effects, electron correlations, spin orbital contributions for the enhancement of the FR at IR wavelengths [97]. Although these theoretical studies represent very important contributions towards an understanding of the electronic correlations in these Ce and Bi systems, they still do not give definitive answers to a number of issues like: the mechanism responsible for the stabilization and enhancement of MO response at IR wavelengths and how it is related with the Cerium and Bismuth dopants. Generally a perturbation of the spin systems and actual effect of substitutions on the electronic structures in these materials are reported to be the major issues [97]. It is speculated [97] that the MO effect originates from ionic electric dipole (ED) transition between the 4f and 5d configurations of the Ce^{3+} ions, which are split by the crystal field (CF) and the super exchange interaction [98]. This is also confirmed by X-ray photoemission and MO spectroscopy in rare earth garnets [99]. These charge transfer mechanism is almost common to all rare earth iron garnets [97].

4.8 Conclusions and prospective future plans

CeBiIG thin films have various applications in integrated magneto-optics. It was successfully grown them in an epitaxial form on (111)-oriented GGG substrates by PLD under a low-pressure argon atmosphere. A very strong FR rotation of 0.55 deg/μm at 1550 nm as well as a saturation field of 0.3 Tesla has been measured. We believe that the Faraday rotation enhancement is caused by the presence of Bi^{3+} ions and it appears to be proportional to its concentration. In addition, Bi relaxes the strain on the system, leading to a better crystallinity. Because of the outstanding magneto-optic properties of the current material, as well as its transparency, and although it is not easy to synthesize, we

believe that CeBiIG is a very promising candidate for next-generation integrated optical isolators as well as for other magneto-optic device applications at telecommunication wavelengths.

However, it should be noted that simple magneto-optical garnet waveguide directly employed as an isolator has some disadvantages. Magneto-optical garnets with large Verdet constant are commonly found to have relatively low refractive indices when compared to III-V semiconductors, such as GaAs. The refractive index of the core layer should be greater than that of the cladding layers, to effectively guide light. This property precludes incorporating traditional magneto-optic garnet materials as waveguide core layers in III-V structures. This drawback may be circumvented through integrating the magneto-optic media as an upper cladding layer [100]. Thus, only the evanescent tail of the guided mode interacts with the magneto-optic media, enabling the integration of a laser and a Faraday isolator using a III-V semiconductor planar technology. The overlap integral reduces the magneto-optical interaction to typically a few percent of that recorded in the bulk of the magneto-optic media, which can be compensated by a commensurate increase in the devices' length.

Structural birefringence associated with conventional waveguide geometries results in induced polarization rotation with an oscillatory behavior, which limits the degree of rotation obtainable.

The choices of a quasi-phase-matching (QPM) approach, which may be implemented through a periodic reversal of the applied magnetic field every beat length, can remove this inherent restriction in the attainable polarization rotation [100]. However, this solution may complicate the fabrication process. Recently, this concept was demonstrated on monolithic integration of isolators with a foot length of 290 μm fabricated on a cerium doped yttrium iron garnet material using YIG buffer layer on SOI platform [21]. Some of these films exhibit strong magnetic anisotropy and strong coercive field along the axis normal to the film plane [101-104]. It is desirable that the MO films have a magnetization and low coercive fields in plane properties essential for applications in integrated waveguides such as optical isolators [21].

For these reasons, a recent study focused on the Cotton-Mouton effect is going to develop a different isolator scheme. The Cotton-Mouton effect, different from the

Faraday Effect, is observed when the magnetic field is directed perpendicular to the propagation direction of an electromagnetic wave, and is responsible of a magnetically induced birefringence.

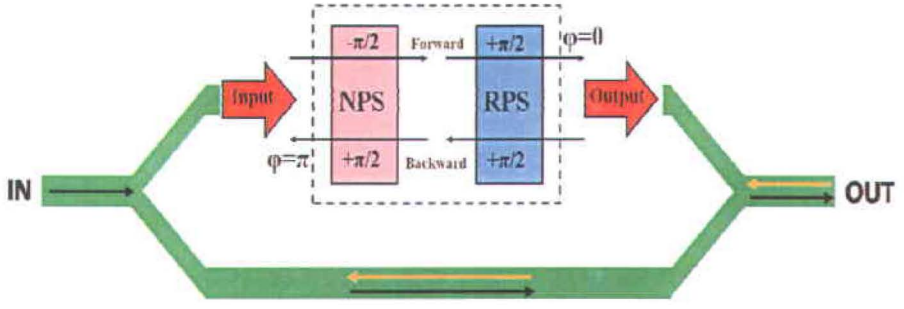

Figure 4.19 Working principle of a Mach-Zehnder isolator. The depicted configuration exploits a cascade of a nonreciprocal phase shifter (NPS) in series with a reciprocal phase shifter (RPS).

The induced birefringence (Δn) is defined for an active medium as the difference between the refractive indices parallel ($n_{\parallel}$) and perpendicular ($n_{\perp}$) to the direction of the applied magnetic field, where $\Delta n = (n_{\parallel} - n_{\perp})$. Over an optical path length L, for a vacuum wavelength λ, the optical retardation of the light when passing through such a medium corresponds to an optical phase difference φ such that:

$$\varphi = 2\pi \frac{\Delta nL}{\lambda} = C2\pi LB^2 \qquad (4\text{-}2)$$

Where "B" is a uniform magnetic field and "C" is the Cotton-Mouton constant. The coefficient of birefringence, or Cotton-Mouton constant, is wavelength dependent, and characteristic of each substance. By using the Cotton-Mouton effect, waveguide-isolators, which involve nonreciprocal phase shifts as "blocking" mechanisms, have been intensively explored in a Mach-Zehnder interferometer (MZI) arrangement with nonreciprocal and reciprocal phase shifters [105-109]. This arrangement is appealing because it is less sensitive to fabrication errors and there is no need for phase matching between orthogonally polarized modes. A simplified scheme for a Mach-Zehnder isolator is given in Figure 4.19. One arm of the MZI is composed of a nonreciprocal phase shifter

(NPS) and a reciprocal phase shifter (RPS) as shown in Figure 4.19. An external magnetic field (not shown in the picture) is applied to the arms with the NPS to obtain a nonreciprocal phase variation in a push-pull manner.

The reciprocal phase difference can be provided by an optical path difference between two or more arms internal to the reciprocal phase shifter. In the conventional design, the reciprocal phase difference required to cancel the nonreciprocal phase variation in the forward direction is found to be $+\pi/2$, which results in constructive interference. Similarly, destructive interference occurs in the reverse direction, blocking the undesired back reflection. In our lab, an effort to improve the current magneto-optical experimental setup for the estimation of the Cotton-Mouton result is in progress.

Chapter 5
Résumé en français

Croissance optimisée et caractérisation de couches épitaxiées de grenat de fer-yttrium avec co-substitution totale de cérium et de bismuth sur le site de l'yttrium (CeBiIG) pour applications à la magnéto-optique intégrée.

Dans ce chapitre, les résultats prometteurs obtenus pour le nouveau matériau magnéto-optique CeBiIG sous forme de couches minces épitaxiées sont présentés et discutés.

L'objectif principal de cette thèse était d'optimiser les paramètres de la synthèse de couches minces épitaxiées de CeBiIG, de comprendre les mécanismes impliqués lors de leur croissance épitaxiale et d'étudier les effets de la substitution de l'yttrium par le cérium et le bismuth sur la microstructure et les propriétés magnéto-optiques (MO) des films de CeBiIG.

Les films épitaxiés de grenat magnétiquesont utilisés dans plusieurs dispositifs technologiques réels. Le choix d'étudier les films de grenat d'yttrium fer a été motivé par les récentes découvertes liées à l'amélioration de leurs propriétés magnéto-optiques, notamment la rotation Faraday, aux longueurs d'ondes utilisées dans le domaine des télécommunications. La fabrication de dispositifs fonctionnels intégrés pour les télécommunications à base de ces matériaux, tels que des isolateurs optiques, nécessite la réalisation de films épitaxiés de haute qualité cristalline. Le sujet de cette thèse est la croissance, l'optimisation et la caractérisation de de couches épitaxiées de grenat de fer-yttrium avec co-substitution totale de cérium et de bismuth sur le site de l'yttrium (CeBiIG) pour applications à la magnéto-optique et elle s'organise de la manière suivante:

Chapitre 1: Synthèse, caractérisation et propriétés magnéto-optiques de couches épitaxiées de CeBiIG.

Chapitre 2: Croissance de de couches minces épitaxiées de CeBiIG seminconducteur.

Chapitre 3 : Techniques de caractérisation utilisées pour étudier les couches minces épitaxiées de CeBiIG

Chapitre 4: Couches minces épitaxiées de CeBiIG magnéto-optique - Résultats et discussions.

Chapitre 5 : Résumé en français.

Ce travail de recherche consiste en l'étude de plusieurs propriétés physiques du système «oxyde de cérium-bismuth-fer » à structure de grenat de formule chimique $Ce_{2.2}Bi_{0.8}Fe_5O_{12}$ obtenue par la substitution complète de l'yttrium par Ce et Bi dans la structure de base du grenat d'yttrium-fer YIG.

Les propriétés magnéto-optiques (MO) dans des systèmes de grenat d'yttrium-fer où l'yttrium a été substitué par un seul dopant, soit cérium ou bien bismuth, ont été récemment explorées [9, 11-16, 21]. De même, le grenat d'yttrium-fer YIG a été utilisé dans la fabrication de composants magnéto-optiques discrètes comme les isolateurs optiques [9, 11, 13, 21]. Pour l'intégration de tels dispositifs magnéto-optiques la croissance épitaxiale de films de haute qualité avec une cristallinité parfaite est requise. C'est ce que nous avons réussi à obtenir durant ce travail avec la réalisation de dépôts de couches minces épitaxiées de CeBiIG par ablation laser pulsée (PLD) sous une atmosphère d'argon. Il est à noter ici que les dépôts effectués sous d'autres atmosphères, telles qu'une atmosphère d'oxygène ou une atmosphère réductrice $Ar + H_2$ ont été également étudiés et qu'ils sont caractérisés par la formation de phases secondaires en proportion importante dans les films. Les conditions de croissance des films ont donc été optimisées en utilisant une atmosphère d'argon, pour laquelle une meilleure qualité cristalline est obtenue comme indiqué par les spectres de diffraction de rayons X (DRX). La morphologie, les analyses structurales, la composition chimique, la rugosité, la transmittance et la réponse magnéto-optique des ces couches minces ont été caractérisés en utilisant les différents outils disponibles dans nos laboratoires. Des recuits *insitu* à de basses températures (600°C – 750 °C) et hautes pressions d'argon sont des conditions nécessaires pour obtenir des films de CeBiIG de haute qualité. La diffraction de RX a démontré que ces films sont fortement orientés selon la direction cristalline [111] et que la qualité de l'épitaxie devient meilleure au fur est à mesure que l'on augmente la

température de dépôt. Cette thèse est une contribution originale qui décrit un matériau pour lequel la réponse magnéto-optique à des longueurs d'ondes utilisées dans le domaine des télécommunications a été fortement améliorée, ce qui est une nécessité pour permettre la fabrication de dispositifs intégrés réels.

Pour cette étude, nous avons choisi le GGG (grenat de gadolinium gallium) comme substrat pour son paramètre de maille proche, mais cependant un peu plus faible que celui des films, permettant ainsi à ces derniers de croître épitaxialement et sous des contraintes compressives. Sur la Figure 5.1, le processus détaillé pour la fabrication de couches minces de CeBiIG est illustré.

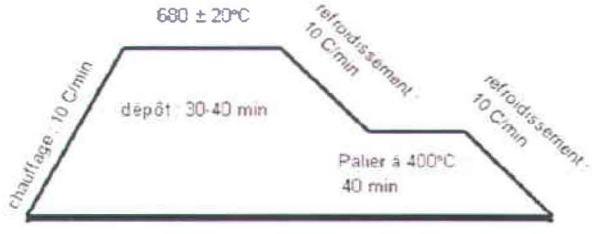

Figure 5.1 Représentation schématique des traitements thermiques utilisés durant la croissance des couches minces de CeBiIG ainsi que pour le recuit insitu.

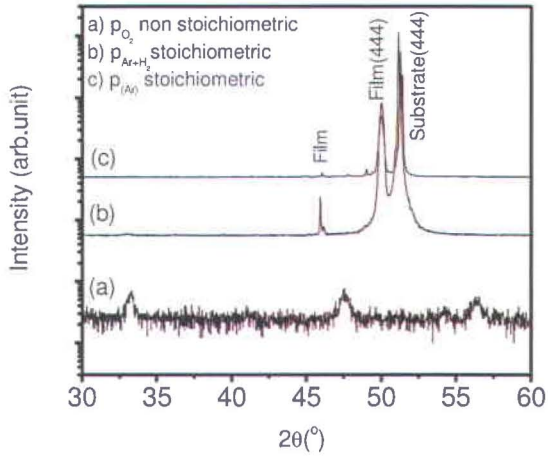

Figure 5.2 Spectres de diffraction de RX obtenus pour des films minces de CeBiIG déposés sous une atmosphère a) de 200 mTorr d'oxygène, (les films de CeBiIG déposés sous oxygène contiennent plusieurs phases et sont parfois même amorphes). Les spectres ne peuvent donc pas être indexés b) de 200 mTorr Ar+H_2, et c) de 200 mTorr d'Argon).

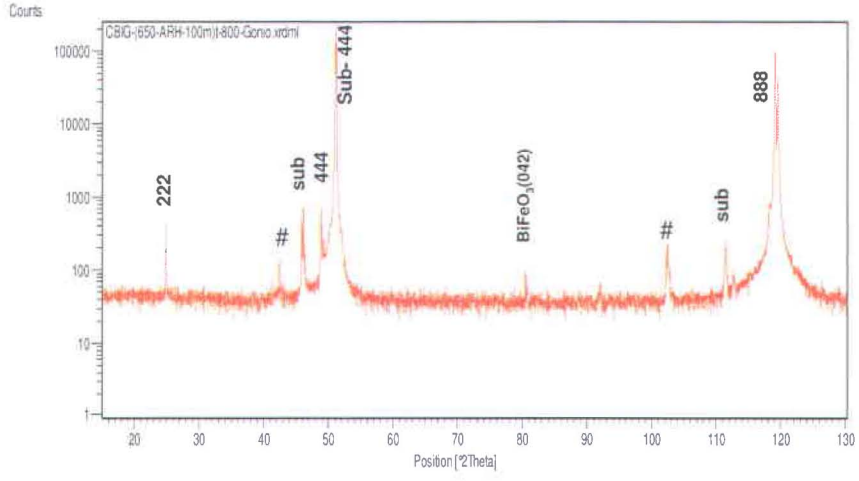

Figure 5.3 Spectre de diffraction θ/2θ d'un film mince de CeBiIG (111) de 1μm d'épaisseur, déposé sur un substrat de GGG orienté (111) et sous une atmosphère réduite Ar+H_2 (# désignent- GGG-Cu kβ).

En comparant les spectres DRX des films déposés sous une atmosphère d'oxygène à ceux obtenus sous atmosphèred'argon, on remarque que les réflexions caractéristiques de la phase de CeBiIG ont des intensités très faibles et certaines sont même masquées par la contribution du substrat aux alentours de 2θ = 51°. De plus, lors de la croissance sous une atmosphère d'oxygène, des phases secondaires se forment au détriment de celle de CeBiIG (cf. Figure 5.2). Les films déposés sous une atmosphère réduite Ar+H_2 montrent des faibles valeurs en transmittance malgré une très bonne qualité cristalline (cf. Figure. 5.3), dû essentiellement à l'oxydation préférentielle du cérium.

Cette étude nous mène à se poser deux questions principales :

- Est-il possible de synthétiser un film mince épitaxié de CeBiIG de haute qualité?
- Si oui, est-il possible d'obtenir pour ces films de bonnes performances magnéto-optique à des longueurs d'onde IR, les rendant intéressants pour la fabrication d'isolateurs optiques intégrés?

En général, les paramètres les plus déterminants dans la croissance de différentes phases sont les suivants : la température de dépôt et la pression d'argon. La meilleure

qualité pour les films (en terme de rugosité, cristallinité et pureté) a été obtenue à (680±20)°C. L'utilisation de l'argon comme atmosphère a été démontrée comme étant importante pour la croissance d'une phase pure de CeBiIG. Le rôle exact joué par l'argon dans ce cas-ci reste néanmoins à éclaircir. Par conséquent, il est important d'avoir un

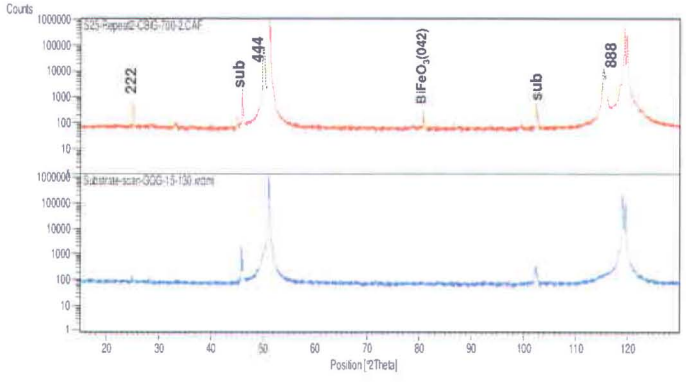

Figure 5.4 Spectres de diffraction X obtenus pour les couches de CeBiIG déposés (sous 300 m.Torr d'Ar) sur des substrats de GGG (111) (en rouge) et pour le substrat GGG seul (en bleu).

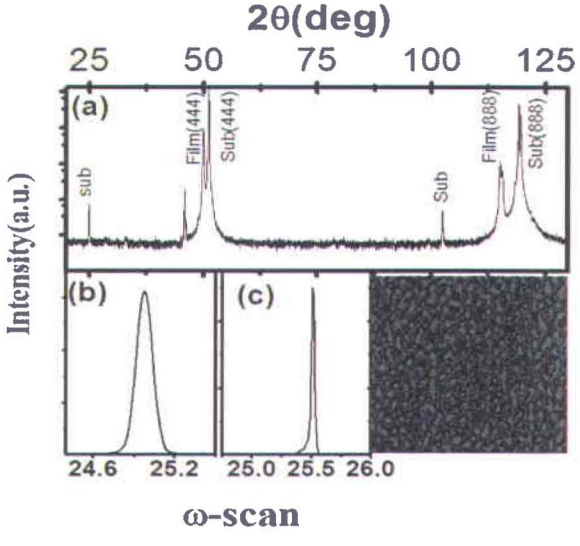

Figure 5.5 (a) Spectre DRX pour un film mince de CeBiIG déposé sur un substrat de GGG orienté (111) et sous une atmosphère de 350 mTorr d'Ar. (b)Balayage en oméga (Rocking curve) de la réflexion (444) de CeBiIG et (c) de GGG, et balayage d'image micrscope électrons de CeBiIG.

contrôle sur tous ces paramètres afin de contrôler la croissance, la stoechiométrie ainsi que d'autres propriétés physiques du matériau. Pour distinguer les pics liés au film de CeBiIG par rapport à ceux du substrat de GGG, le spectre DRX de ce dernier est présenté à la Figure 5.4. L'épitaxie des couches minces de CeBiIG est aussi confirmée par des observations par diffraction de RX comme on peut le constater à la Figure 5.5. Pour les films déposés à une température de 750°C, une déviation notable de la stœchiométrie est révélée par la Figure 5.6. Un même constat est observé pour les films déposés à des

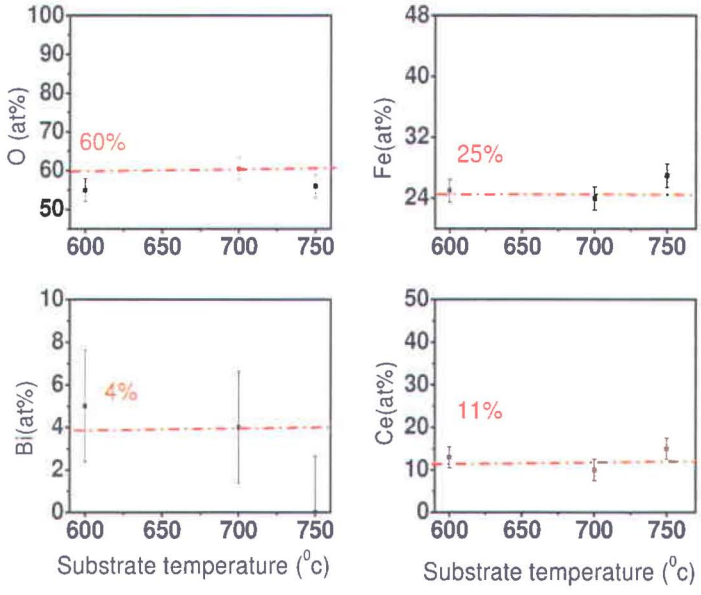

Figure 5.6 Concentrations atomiques des éléments constituant le CeBiIG en fonction de la température du substrat lors de la croissance des couches minces.

pressions d'argon excédant les 350 mTorr. Ceci suggère donc que le choix des paramètres est important pour obtenir une bonne stœchiométrie pour les films comme illustré sur la Figure 5.7 (la line rouge indique la stçchiométrie attendue pour la cible CeBiIG).

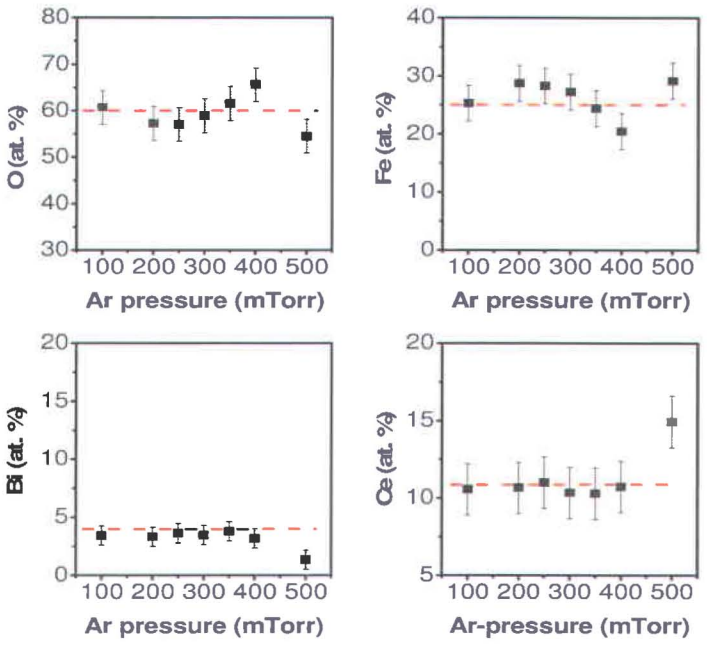

Figure 5.7 Concentrations atomiques des éléments constituant le CeBiIG en fonction de la pression d'Ar lors de la croissance des couches minces.

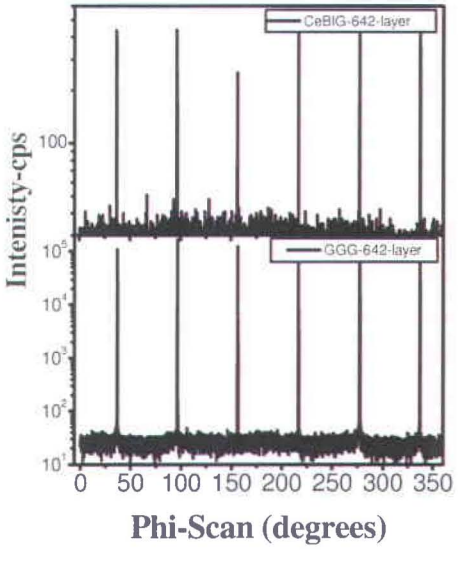

Figure 5.8. Balayages en ϕ des réflexions a) 642 d'une couche épitaxiée de CeBiIG b) 642 du substrat GGG obtenus pour un films épitaxié de CeBiIG déposé sur un substrat de GGG (111), sous une atmosphère d'argon de 350 mTorr.

En ce qui concerne la structure cristalline des films, le phi-scan des plans (642) obtenus par DRX illustré à la Figure 5.8, suggère qu'une relation d'épitaxie de type cubique sur cubique existe entre le substrat et le film CeBiIG.

Les différents aspects de la croissance, de la structure cristalline, des propriétés magnétiques et magnéto-optiques du matériau CeBiIG ont été étudiés par une variété de techniques in-situ et ex-situ.

Tous les films montrent de bonnes valeurs de transmittance et une forte rotation Faraday (FR), ce qui est intéressant du point de vue des applications. Ces excellents résultats de FR ont été obtenus par des mesures à des longueurs d'onde de 1550 nm (usuelle dans le domaine des télécommunications) au moyen d'un équipement spécifiquement dédié à cette mesure et construit sur mesure dans nos laboratoires. Le principe de fonctionnement de cet équipement dédié à la mesure de la rotation Faraday est présenté à la Figure 5.9a. Ceci constitue une contribution majeure pour la communauté scientifique traitant le sujet, dans la mesure où nos films de CeBiIG montrent une très forte rotation de Faraday (0.55 μm) (Figure 5.9b).

En effet, une telle valeur record de la rotation Faraday à des longueurs d'ondes utilisées dans le domaine des télécommunications n'avait jamais encore été enregistrée dans les familles des grenats d'yttrium-fer. Les résultats obtenus dans le cadre de ce travail de maîtrise sont donc très prometteurs et vont certainement contribuer à l'identification et à l'élaboration de nouveaux matériaux pour des applications dans le domaine magnéto-optique intégrée.

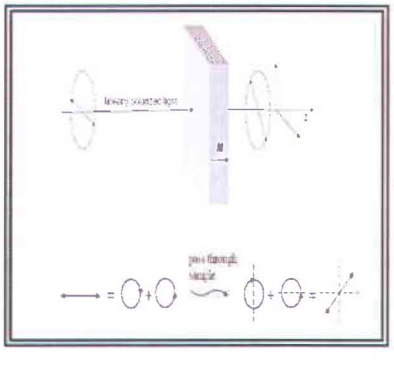

(a)

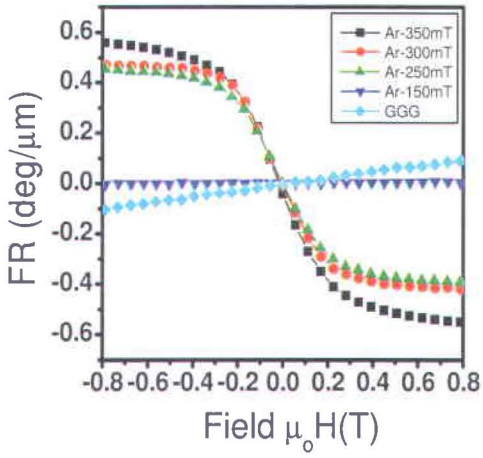

(b)

Figure 5.9 a) Représentation schématique de la mesure de la rotation Faraday effectuée lors de ce travail. b) Rotations de Faraday, à la longueur d'onde de 1550 nm représentée en fonction du champ magnétique appliqué, obtenues pour des films de CeBiIG déposés sous différentes pression d'argon i) 350 mTorr ii) 300 mTorr iii) 250 mTorr iv) 150 mTorr. v) La contribution du substrat de GGG seul est aussi montrée.

Une investigation détaillée sur les propriétés physiques de grenat d'yttrium-fer avec substitution de l'yttrium par du cérium et du bismuth a été réalisée au début des années 90 à la fois sous forme massive ou en couches minces [9, 11, 13, 21]. Les propriétés physiques mesurées à des longueurs d'onde utilisées en télécommunications ont révélé qu'en dépit de la similitude au niveau de leurs structures, les propriétés magnétiques et magnéto-optiques des ces oxydes sont très différentes. Dans la structure type des grenats d'yttrium-fer $Ce_xY_{1-x}Fe_5O_{12}$, le Ce montre une stabilité pour des valeurs n'excédant pas x = 0.6 alors que pour ceux à base de bismuth, $Bi_xY_{1-x}Fe_5O_{12}$, la stabilité est obtenue sur toute la gamme de substitution, jusqu'à une valeur de x = 3 pour le composé entièrement substitué $Bi_3Fe_5O_{12}$. L'origine de cette différence entre les propriétés de ces différents dopants a été mise en évidence par des études antérieures disponibles dans la littérature. Ces études ont démontré que la structure électronique et les propriétés de ces deux matériaux sont gouvernés par de possibles effets induits par la présence de lacunes et de corrélations électroniques, des contributions de type spin-orbite permettant de fortes réponses magnéto-optiques à des longueurs d'onde IR [4,5]. Bien que ces études théoriques représentent une contribution non négligeable pour une

meilleure compréhension des corrélations électroniques dans ces systèmes à base de Ce et Bi, elles ne répondent cependant pas complètement à certaines interrogations telles que : quel est le mécanisme responsable de la stabilisation et de l'amélioration de la réponse magnéto-optique dans l'infrarouge (IR) dans les systèmes conjointement dopés au Ce et Bi; quelle est la perturbation induite sur les spins ainsi que l'effet exact de la substitution sur la structure électronique de ces composés.

Durant ce travail de recherche, la déposition par ablation laser nous a permis de bien contrôler la stœchiométrie des couches de CeBiIG réalisées. Les mesures des propriétés physiques pour ce matériau ont été réalisées pour la première fois et avec succès dans le cadre de ce travail. En particulier, on peut citer la croissance épitaxiale sous une atmosphère d'argon, ainsi que la mesure dans les couches de CeBiIG de la transmittance sur un intervalle assez large de longueur d'ondes.

Dans le chapitre 1, la structure cristalline du nouveau composé $Ce_{2.2}Bi_{0.8}Fe_5O_{12}$ (CeBiIG), ainsi que ses propriétés magnéto-optiques sont décrites. Ces dernières sont ce qui motive notre intérêt pour la synthèse de films minces des CeBiIG et l'étude de ses propriétés magnéto optiques du nouveau composé $Ce_{2.2}Bi_{0.8}Fe_5O_{12}$ (CeBiIG). En effet la rotation Faraday des couches minces épitaxiées du nouveau composé CeBiIG synthétisées dans le cadre de ce travail s'est avérée être la plus élevée jamais rapportée dans la classe de matériaux des grenat d'yttrium-fer. La dernière partie de ce chapitre se concentre sur l'effet Faraday et son utilisation dans la fabrication d'un dispositif particulier : l'isolateur optique.

Dans le chapitre 2, les différents modes de croissance des couches minces sont brièvement présentés, ainsi que la technique de dépôt par ablation laser pulsée (PLD), la technique de dépôt utilisée pour la synthèse des couches épitaxiées de CeBiIG, en prêtant attention aux paramètres clés qui contrôlent le dépôt par PLD. L'importance de la température à laquelle le substrat se trouve durant le dépôt y est également discutée ainsi que la manière de mesurer et de calibrer celle-ci. Finalement, le traitement thermique auquel la couche déposée doit être soumise après son dépôt est présenté, ainsi que le dispositif expérimental permettant ce traitement. Ce recuit thermique permet d'obtenir la phase désirée, dans la qualité et la pureté désirée.

Dans le Chapitre 3, les techniques de caractérisation des matériaux utilisées dans ce travail ainsi que l'importance pratique de chaque technique sont présentées en détail. Pour décrire la microstructure des couches minces de CeBiIG, nous avons utilisé microscopie électronique à balayage (SEM/EDX), la diffraction de rayons X (XRD), la microscopie à force atomique (AFM) et la spectroscopie de photoélectrons X (XPS).

Dans le chapitre 4, nous présentons les résultats expérimentaux et une discussion sur la morphologie, les propriétés structurales et magnéto-optiques des couches minces de CeBiIG déposées épitaxialement sur des substrats de GGG. Les couches minces épitaxiées du nouveau matériau magnéto optique CeBiIG ont été synthétisé par ablation laser et sont caractérisées par une co-substitution complète de l'yttrium par du bismuth et du cérium dans le grenat d'yttrium-fer original. Après une optimisation minutieuse des conditions de croissance, plusieurs séries de couches minces de CeBiIG ont été préparées en variant le flux d'argon et en maintenant une stœchiométrie en Ce et Bi quasi-constante. Certains échantillons ont fait l'objet de recuits ex-situ, mais la composition et la structure de ces derniers ne sont pas meilleurs comparés aux échantillons recuits in-situ. Nous avons aussi essayé de faire croître des films minces sous une atmosphère d'oxygène et dans une atmosphère réductrice ($Ar+H_2$), mais là non plus nous n'avons pas pu obtenir de meilleurs résultats que sous Ar. Par conséquent, nous avons restreint nos dépôts à ceux obtenus sous une atmosphère d'argon dont les résultats semblent être supérieurs.

La rotation de Faraday par unité d'épaisseur mesurée sur les couches optimisées de CeBiIG est la plus élevée de sa catégorie. En outre, les mesures magnéto-optiques ont été réalisées avec un montage de fabrication artisanale avec un aimant fourni par GMW (USA).

À partir des résultats en transmittance, nous avons estimé les constantes optiques et l'indice de réfraction des couches de CeBiIG. Ces films présentent de bonnes valeurs de transmittance.

L'origine des excellentes propriétés magnéto-optiques de CeBiIG est présentée et discutée dans ce travail, mais celles-ci restent encore à expliquer théoriquement. Le diagramme de phase (Figure 5.10) indique clairement l'effort déployé pour la réalisation

des films minces épitaxiés de CeBiIG de bonne qualité dont les paramètres de croissances optimaux pour une bonne transmittance et une rotation Faraday maximale se concentrent dans une fenêtre assez étroite.

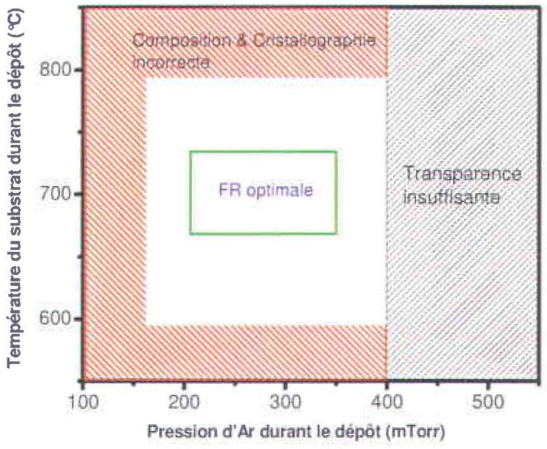

Figure 5.10. Diagramme de phase des films épitaxiés de CeBiIG (Transmittance, rotation Faraday optimisée et cristallographie non souhaitée sont clairement indiquées).

À la Figure 5.10, l'optimisation des paramètres de dépôt des couches minces de CeBiIG est illustrée. Comme on le constate, une meilleure qualité des films et une forte rotation de Faraday sont obtenus dans la région de paramètres indiquée par un ovale de couleur verte. Une faible transmittance (non –souhaitée dans notre cas) est observée pour les films préparés dans une atmosphère d'Ar dont la pression excède 400 mTorr. De même, pour des températures de dépôts au-delà de 750°C et après les différents traitements de recuit, des phases parasites de compositions et des structures cristallines indésirables apparaissent dans les films. Dans cette étude, les mesures répétées sont très importantes afin de connaître la réponse magnéto optique globale des films et de déterminer la fenêtre optimale pour plusieurs propriétés physiques associées à la réalisation d'une rotation de Faraday géante. Le diagramme de phase avec la fenêtre étroite de températures et de pressions de dépôt résultants en des films de CeBiIG pur explique clairement les efforts qu'a nécessité la production de films épitaxiés de CeBiIG

d'excellente qualité. Nous avons également confirmé que la pression d'argon entre 200-375 mTorr et la température 680-720°C sont les principaux paramètres influençant le dépôt de ces films sur des substrats épitaxiés GGG.

Les transitions responsables de la réponse optique et des propriétés magnéto-optiques des films restent à étudier plus en détail. Des explications théoriques et des études complémentaires sont nécessaires pour mieux comprendre la physique à l'origine de ces phénomènes.

Le chapitre 4 présente aussi des analyses XPS détaillées effectuées sur plusieurs échantillons de films minces de CeBiIG. Sur les spectres XPS, à de hautes énergies de liaisons, des structures additionnelles sont souvent observées qui sont des pics satellites à des énergies de liaison légèrement inférieures à celles des pics principaux correspondants. Ces pics satellites sont généralement reliés à l'hybridation entre les électrons de conduction et les électrons de l'orbitale 4f responsables des propriétés magnétiques. L'intensité de ces pics satellites est particulièrement forte pour les premiers éléments du groupe des terre-rares [21].

Finalement, le chapitre 5 est le résumé des travaux en français.

Conclusions sur les films épitaxiés de CeBiIG réalisé durant ce travail de maîtrise

Tous les films CeBiIG ont été déposés par PLD. Les paramètres de dépôt optimisés sont une température du substrat Ts = 680±20°C, une pression d'Ar de 200-350 mTorr durant le dépôt et une densité énergie du laser de 3J/cm^2. Ces paramètres permettent d'obtenir des films homogènes de bonne qualité cristalline.

- Des recuits in-situ après les dépôts des films minces de CeBiIG ont donné de meilleurs résultats au niveau de la qualité cristalline que des recuits ex-situ.
- Les interfaces entre les films et le substrat GGG sont de bonne qualité et lisses.
- Les films de CeBiIG (d'épaisseur de 0.9-1μm) croissent épitaxialement selon la direction cristalline 111 sur les substrats de GGG orientés (111). La longueur de cohérence estimée à partir des spectres DRX (formule Scherrer) est de 100 nm et décroît avec l'augmentation de l'épaisseur des couches.

- Des films stœchiométriques de CeBiIG ont été déposés sur des substrats de GGG, avec une stœchiométrie proche de celle de la cible, CCe+CBi/CFe ~ 0.51-0.56. Cette stœchiométrie est mesurée et confirmée par des analyses élémentaires aux moyens des spectroscopies XPS, et EDX.
- Les mesures expérimentales de la transmittance sont correctement reproduites par des calculs et simulations théoriques.
- L'indice de réfraction des films de CeBiIG est de l'ordre de 2.52 à 2.65.
- Les mesures magnétiques ont révélé le comportement paramagnétique des films de CeBiIG déposés sur des substrats de GGG.

Des mesures de la rotation de Faraday dans les films à 1.55μm révèle une rotation record de l'ordre 0.55 μm, jamais observée auparavant dans les grenat d'yttrium-fer et à cette longueur d'onde utilisable pour les télécommunications optiques.

Il faut souligner que tous les résultats obtenus dans le cadre de ce travail de recherche sont reproductibles et très prometteurs.

Perspectives : Intégration dans des dispositifs sur puce (ou système mono-puce)

L'intégration des couches magnéto-optiques dans un système mono-puce n'en est actuellement qu'à ces débuts et des études sur les techniques d'élaboration des dispositifs magnéto-optiques intégrés, leurs applications ainsi que leur potentiel industriel sont donc nécessaires. Cependant, l'application industrielle de ces matériaux a besoin de fortes réponses magnéto-optiques et cela à des longueurs d'onde utilisée dans le domaine des télécommunications, c'est-à-dire le proche IR. Il a été également mis en exergue dans la littérature que les dopants Bi et le Ce, se substituant au Y, sont les principaux éléments amenant à une forte augmentation de la réponse magnéto-optique des grenats d'yttrium-fer. Pour des considérations pratiques, il est souhaité que l'intégration de dispositifs optiques, donc en particulier des composés magnéto-optiques, se fasse sur une seule puce (Si, SiO_2 ou polymère). Des méthodes nouvelles doivent donc être développées pour réaliser des films de ces matériaux caractérisés par de fortes réponses magnéto-optiques. La technique de pulvérisation cathodique des grenats d'yttrium-fer sur des supports

comme le verre et le silicium a notamment été développée et la réponse magnéto-optique des films obtenus caractérisée. Ces films exhibent une forte anisotropie magnétique et de larges champs coercitifs selon l'axe normal au film [17, 86, 102-104]. Ces films possèdent une magnétisation et de faibles champs coercitifs dans le plan, propriétés indispensables pour des applications intégrées dans des guides d'ondes, comme par exemple des isolateurs optiques intégrés à rotation de Faraday [21].

Il reste encore beaucoup de travail à réaliser pour permettre l'intégration de grenats de fer magnéto-optiques dans des dispositifs réels, en utilisant la technologie utilisée pour la fabrication des dispositifs microélectroniques semi-conducteurs intégrés. Le succès de cette intégration devrait favoriser une réduction des coûts et susciter un intérêt plus marqué pour les films des matériaux magnéto-optiques. Pour la suite, une investigation plus détaillée de l'effet de l'augmentation de la concentration en Ce, au lieu de celle de Bi dans les composés $Ce_{1-x}Fe_5O_{12}$ et $Ce_{1-x}Y_xFe_5O_{12}$ pourrait apporter des informations intéressantes qui permettraient peut-être de de mieux comprendre les excellentes propriétés du CeBiIG, et notamment sa rotation Faraday record.

Une meilleure compréhension des effets physiques exacts en jeu lors de la substitution de l'Y par du Ce ou du Bi, ainsi que lors de la substitution conjointe par Ce et Bi, sur l'amélioration des propriétés magnéto optiques des films pourrait permettre d'élaborer de nouveaux matériaux encore plus performants pour des applications dans l'isolation optique.

Bibliography

[1] G. E. Moore, *Cramming more components onto integrated circuits,* Electronics, Vol. 38, 8, (1965).

[2] A. Aviram and M. A. Ratner, *Annals of the New York Academy of Sciences,* Molecular Electronics III, Vol. 1006, (2003).

[3] G. P. Agrawal, *Fiber-Optic Communication Systems,* Kai Chang Series Editor. Introduction, (2002).

[4] H. Nishihara, M. Haruna and T. Suhara, *Optical integrated circuits,* McGraw-Hill Optical and electro-Optical Engineering series, Chapter 1, (1989).

[5] K. H. Brenner, A. Huang, *Logic and architectures for digital optical computers (A)*, J. Opt. Soc. Am., A3, 62, (1986).

[6] M. Chandra Sekhar, J.Y. Hwang, M. Ferrera, M. Zaezjev, L. Razzari, Y. Linzon, A. Pignolet, R. Morandotti, *Strong enhancement of the Faraday rotation in Ce and Bi co-modified epitaxial iron garnet thin films,* Appl. Phys. Lett. 94, 181916-3 (2009).

[7] J. Y. Hwang, R. Morandotti and A. Pignolet, "Strong Faraday rotation in Ce and Bi comodified epitaxial iron garnet films: valence control through strain engineering," Appl. Phys. Lett. 99(5), 051916-3 (2011).

[8] M. Chandra Sekhar, Mahi. R. Singh, Shantanu Basu and Sai Pinnepalli, Giant Faraday rotation in $Bi_xCe_{3-x}Fe_5O_{12}$ thin films, Optics Express 20 (9), 9624 (2012).

[9] S. Higuchi, Y. Furukawa, S. Takekawa, O. Kamada, K. Kitamura, and K Ueda, *Magneto-optical properties of cerium-substituted yttrium iron garnet single crystals for magnetic-field sensors*, Sens. Actuators-A Phys. A. 105, 293 (2003).

[10] K. Matsuda, H. Minemoto, O. Kamada, S. Ishizuka, Bi-*Substituted Rare-Earth Iron Garnet Composite Film with Temperature Independent Faraday rotation for optical Isolators*, IEEE Trans. Magn. Mag. 23, 3479 (1987).

[11] S. Kahl, S. I. Khartsev, A. M. Grishin, K. Kawano, G. Kong, R. A. Chakalov and J .S. Abell, *Structure, microstructure, and magneto-optical properties of laser deposited $Bi_3Fe_5O_{12}/Gd_3Ga_5O_{12}$ (111) films*, J. Appl. Phys. 91(12), 9556-9560 (2002).

[12] L. E. Helseth, A. G. Solovyev, R.W. Hansen, E.I. llyashenko, M. Baziljevich, T. H. Johansen, Faraday *rotation and sensitivity of (100) bismuth-substituted ferrite garnet films*, Phys. Rev. B 66, 064405 (2002).

[13] M. Gomi, H. Furuyama and M. Abe, *Strong magneto-optical enhancement in highly Ce-substituted iron garnets films prepared by sputtering,* J. Appl. Phys. 70(11), 7065-7068(1991).

[14] G. Menzer. *Die K Kristallstruktur von Garnat*. Centralbl. Min [A], p 344ff, (1925).

[15] G. Menzer. *Die Kristallstruktur der Garnate*. Z. Kristallogr, 69: 300ff, (1928).

[16] S. Geller and M. A Gilleo, *The crystal structurere and ferrimagnetism of yttrium iron garnet,* $Y_3Fe_2(FeO_4)_3$, J. Phys.Chem.Solids. 3, 30-36 (1957).

[17] S. Geller, *The statistics of super exchange interaction and ionic distribution in substituted ferrimagnetic rare earth iron garnets*, J. Phys.Chem.Solids. 16(1-2), 21-29(1960).

[18] Nishihara, M. Haruna, T. Suhara, *Optical integrated circuits*, McGraw-Hill optical and electro-optical Engineering series, Chapter 5, (1989).

[19] A. B. Villaverde and D. A. Donatti, Verdet *constant of liquids: measurements with a pulsed magnetic field,* J. Chem. Phys. 71, 4021–4024 (1979).

[20] T. Yoshino, *Theory for the Faraday effect in optical fiber,* J. Opt. Soc. Am. B, 22(9), 1856-1860 (2005).

[21] L. Bi, J. Hu, P. Jiang, D. H. Kim, G. F. Dionne, L. C. Kimerling and C. A. Ross, *"On chip optical isolation in monolithically integrated non-reciprocal optical resonators"*, Nature. Photon. 5(13), 758-762 (2011).

[22] C. S. Chern, J. S. Martens, Y. Q. Li, B. M. Gallois, P. Lu and B. H. Kear, *Metal organic chemical deposition of large area high quality* $YBa_2Cu_3O_7$ *films in a high speed rotating disc reactor,* Supercond. Sci. Technol. 6, 460-463, (1993).

[23] B. Vukasinovic, S. Sundell, M. Oljaca, closed *loop controlled* $Ba_xSr_{1-x}TiO_3$ *thin films in spray flames*, Surface Engineering, Volume 19, No 3, 179-184(6), (2003).

[24] R. P. Howson, *The plasma reflection edge in thin films of semiconductors,* J. Phys. D: Appl. Phys. 1, 15-23, (1968).

[25] D. Y. Wang, C. L. Mak, K. H. Wong, H. L. W. Chang, C. L. Choy, *Optical properties of $Ba_{0.5}Sr_{0.5}TiO_3$ thin films grown on MgO substrates by pulsed laser deposition,* Ceramic International. 30, 1745-1748, (2004).

[26] D. B. Chrisey and G. K. Hubler, Pulsed Laser deposition of thin films, Eds, John Wiley & Sons, New York (1994).

[27] R. Eason, Pulsed laser deposition of thin films: Applications-led Growth of Functional Materials, John Wiley & Sons, Inc, chapter 1 (2007).

[28] P. R. Wilmott and J. R. Hubler, Pulsed laser vaporization and deposition, Rev. Mod. Phys. 72, 315-328 (2000).

[29] D. Dijkamp, T. Venkatesan, X. D. Wu, S. A. Shaheen, N. Jisrawi, Y. H. Min-Lee, W. L. McLean, M. Croft, *Preparation of Y-Ba-Cu-oxide superconductor thin films using pulsed laser evaporation from high Tc bulk material*, Appl. Phys. Lett. 51, 619-621 (1987).

[30] F. Breech, L. Cross, *Optical micro emission stimulated by a ruby MASER*, Appl. Spectroscopy. 16, 59 (1962).

[31] H. M. Smith, A.F. Turner, *Vacuum deposited thin films using a Ruby laser*, Appl. Opt. 14(1), 147-148 (1965).

[32] H. Adachi, K. Wasa, *Sputtering preparation of ferroelectric PLZT thin films and their optical application,* IEEE Trans. Ultrasonic, Ferroelectrics, Frequency control. 38 (6), 645-655 (1991).

[33] P. B. Mozhaev, P. V. Komissinski, N. P. Kukhta, A. Kiihle, G. A. Ovsyannikov, and J. L. Skov, *Deposition of superconducting $YBa_2Cu_3O_{7-\delta}$ thin Films*, J. of superconductivity. Vol. 10, 3 (1997).

[34] H. U. Krebs, M. Weisheit, J. Faupel, E. Suske, T. Scharf, C. Fuhse, M. Stormer, K. Sturm, M. Seibt, H. Kijewski, D. Nelke, E. Panchenko, and M. Buback. *Pulsed Laser Deposition (PLD); a versatile thin film technique,* Available on web.

[35] W. Wu, K. H. Wong, and C. L. Choy, *The role of energetic plasma in pulsed laser deposition of epitaxial manganite films*, J. Phys. D: Appl. Phys. 32, L57–L60, (1999).

[36] K. Kinoshita, H. Ishibashi, and T. Kobayashi, *Improved surface smoothness of YBa_2Cu_3Oy films and related multilayers by ArF excimer laser deposition with shadow mask Eclipse method,* Jap. J. Appl. Phys. 33, L417, (1994).

[37] Z. Trajanovic, S. Choopun, R. P. Sharma and T. Venkatesan, *Stoichiometry and thickness variation of $YBa_2Cu_3O_{7-x}$ in pulsed laser deposition with a shadow mask,* Appl. Phys. Lett. 70, 3461 (1997).

[38] M. N. R. Ashfold, F. Claeyssens, G. M. Fuge and S. J. Henley, *Pulsed laser deposition of thin films,* Chem. Soc. Rev, 33, 23-31 (2004).

[39] P. Alberto, J. Villain, Physics of crystal growth. Cambridge, Cambridge University Press, Eaglesham (1998).

[40] D. J. M. Cerullo, Phys. Rev. Lett. 64 (16), 1943 (1990).

[41] H. S. Kim and H. S. Kwok, *Correlation between target substrate distance & oxygen pressure in pulsed laser deposition of $YBa_2Cu_3O_{7-x}$, Appl.* Phys. Lett. 61, 2234 -2236(1992).

[42] S. V. Pietambaram, D. Kumar, C. B Lee, V. Craciun, *Laser solid interactions for Materials processing,* Mat. Res. Soc. Symp. Vol. 617 (2000).

[43] N. Adachi, V. P. Denysenkov, S. I. Khartsev, A. M. Grishin, and T. Okuda, *Epitaxial $Bi_3Fe_5O_{12}(001)$ films grown by pulsed laser deposition and reactive ion beam sputtering techniques*, J. Appl. Phys. 88, 2734-2740 (2000).

[44] H. Dötsch, N. Bahlmann, O. Zhuromskyy, M. Hammer, L. Wilkens, R. Gerhardt, P. Hertel, *Application of magneto-optical waveguides in integrated optics: review*, J. Opt. Soc. Am. B. 22, 240-253 (2005).

[45] S. Fahler, M. Stormer, and H. U. Krebs, *Origin and avoidance of droplets during laser ablation of metals,* Appl. Surf. Sci. 109/110, 433-436 (1997).

[46] A. A. Gorbunov, W. Pompe, A. Sewing, S. V. Gaponov, A. D. Akhsakhalyan, I. G. Zabrodin, I. A. Kaskov, E. B. Klyenkov, A. P. Morozov, N. N. Salaschenko, R. Dietsch, H. Mai and S. Vollmar, *Ultrathin film deposition by pulsed laser ablation using crossed beams*, Appl. Surf. Sci. 96-98, 649-655 (1996).

[47] A. Tong, *Improving the accuracy of temperature measurement,* Sensor Review, 21, 3 (2001).

[48] J. F. Schooley, Thermometry, New York: CRC Press, 172 (1986).

[49] Stephen A. Dyer, 'Survey of instrumentation and measurement', John Wiley & Sons, (2001).

[50] V. Craciun, D. Craciun, Z. Chen, J. Hwang, R. K. Singh, *Room temperature growth of indium tin oxide thin films by ultraviolet assisted pulsed laser deposition,* Appl. Surf. Sci, 168, (1-4), 118-122 (2000).

[51] M. Chandra Sekhar, *Simple and cost effective fabrication of ZnO thin films on hydrogen terminated silicon substrates by nebulised spray pyrolysis*, Int. Journal of Mod. Phy. B (IJMPB). 22 (3), 219-229 (2008).

[52] S. T. Tay, X. H. Jiang, C. H. A. Huan, A. T. S. Wee and R. Liu, *Influence of annealing temperature on ferroelectric properties of* $SrBi_2Ta_2O_9$ *thin films prepared by off axis radio frequency magnetron sputtering,* J. Appl. Phys, 88, 5928-5934 (2000).

[53] M. Chandra Sekhar, *Structural and dielectric properties of* $Ba_{0.5}Sr_{0.5}TiO_3$ *thin films grown on LAO with homo-epitaxial layer for tunable applications,* Int. Journal of Mod. Phy. B (IJMPB). 18(15), 2153-2168 (2004).

[54] C. Fu, C. Yang, H. Chen, Y. Wang, L. Hu, *Microstructure and dielectric properties of* $Ba_{1-x}Sr_{1-x}TiO_3$ *ceramics,* Mater. Sci. Eng. B. 119 (2), 185-188, (2005).

[55] Z. Zhao, V. Buscaglia, M. Viviani, M.T. Buscaglia, L. Mitoseriu, A. Testino, M. Nygren, M. Johnsson and P. Nanni, *Grain size effects on the ferroelectric behavior of dense nano crystalline* $BaTiO_3$ *ceramics*, Phy. Rev. B. 70, 024107-8 (2004).

[56] M. Vasiliev, K. E. Alameh, V. A. Kotov, and Y. T. Lee, "Nanostructured engineered materials with high magneto-optic performance for integrated photonics applications,'' in Proceedings. IEEE Photonics Global @Singapore, (IPGC 2008).

[57] Nizar Hamden. *A Dynamic Approach to De Broglie's Theory*, Apeiron, Vol. 12, No. 3, 274 (2005).

[58] *A guide to Scanning microscope observation*, JEOL, available on the web.

[59] C. W. Oatley, *The early history of scanning electron microscope*, J. Appl. Phys. 53, R1-R13 (1982).

[60] H. Ahmed, *Studies on high current density thermionic cathodes*, PhD Dissertation, Cambridge University (1962).

[61] K. C. A. Smith and C .W. Oatley, *The scanning electron microscope and its field of application,* Brit. J. Appl. Phys. 6(11), 391-399 (1955)

[62] http://www.mse.iastate.edu/microscopy/prep2.html

[63] B. D. Cullity, S. R. Stock, Elements of X-ray Diffraction, Prentice Hall, NJ (2001).

[64] O. Carnal and J. Mlynek, *Young's double-slit experiment with atoms: a simple atom interferometer,* Phys. Rev. Lett. 66, 2689-2692 (1991).

[65] G. Rhodes, *Crystallography Made Crystal Clear*, 3rd edition, Academic Press. CA, (2000).

[66] http://www.tishreen.shern.net/new

[67] L. Marton, *Electron interferometer,* Phys. Rev. 85, 1057-1058, (1952).

[68] C. Jönsson, *Electron diffraction at multiple slits*, American. J. of Physics, 42(1), 4-11 (1974).

[69] XRD-Xpert- software-http://www.panalytical.com

[70] http://users.du.se/~h05imdar/afm2006.pdf

[71] G. Binnig, C. F. Quate, C. H. Giber, *Atomic Force Microscope*, Phys. Rev. Lett. 56(9), 930-933(1986).

[72] J. H. Hoh and P. K. Hansma, *Atomic force microscopy for high-resolution imaging in cell biology. Source*: Trends Cell Bio. 2, 208-213, (1992).

[73] C. Sones, S. Mailis, V. Apostolopoulos, I. E. Barry, C. Gawith, P.G. R. Smith and Robert. W. Eason, *Fabrication of Piezoelectric micro cantilevers in domain engineered $LiNbO_3$ single crystals*, J. Micromech. Microeng. 12, 53, (2002).

[74] G. Binnig and H. Rohrer, *Scanning Tunneling Microscopy—From Birth to Adolescence,* Rev. of Mod. Phys. 59(3), 615 (1987).

[75] C. Harnagea and A. Pignolet, *Challenges in the analysis of the piezoelectric response* (Chapter 2), In A. Gruverman and M. Alexe (eds.) *Nanoscale characterization of ferroelectric materials; Scanning probe microscopy approach*, Springer - Verlag, 45-85 (2004).

[76] G. Meyer, N. M. Amer, *Novel optical approach to atomic force microscopy*, Appl. Phys. Lett. 53(12), 1045-1047(1988).

[77] T. R. Albrecht, S. Akamine, T. E. Carver, and C. F. Quate, *Microfabrication of cantilever styli for the atomic force microscope,* J. Vac. Sci. Technol. A 8(4), 3386-3396 (1990).

[78] C. A. J. Putman, B. G. De Grooth, N. F. Van Hulst, and J. Greve, *A detailed analysis of the optical beam deflection technique for use in atomic force microscopy,* J. App. Phys. 72(1), 6-12(1992).

[79] J. A. Gallego-Juarez, Piezoelectric ceramics and ultrasonic transducers, J. Phys. E: Sci. Instrum, 22, 804-816 (1989).

[80] U. Hartman, Annu.Rev.Mater.Sci. **29**, 53 (1999).

[81] Y. Martin and H .K.Wickramasinghe, Appl. phys. Lett. **50**, 1455 (1987).

[82] M. John C. Vickerman, *Surface analysis-The principal Techniques*, John Wiley & Sons (1997).

[83] T. J. Shaffner and R.D. van veld, *charging effects in the scanning electron microscope,* J. Phs. E: Sci. Instrum 4(9), 633-637(1971).

[84] D. A. Shirley, *High resolution X-ray photoemission spectrum of the valence bands of gold, Phys.* Rev. B 5, 4709-4714(1972).

[85] B. S. Norgren, M. A. J Somers, J. H. W de Wit, *Application of Tougaard background subtraction to XPS spectra of passivated Fe-17Cr*, Surf. Interface Anal. 21(6-7), 378-381(1994).

[86] J. F. Moulder, W. F. Stickle, P. E. Cobol, and K. D. Bomben, *in Handbook of X-ray photoelectric spectroscopy*, edited by J. Chatain, Perkin-Elmer, Eden Prairie, MN, (1992).

[87] M. Aronniemi, J. Lahtinen, P. Hautojarvi, *characterization of iron oxide thin films,* Surf. Interface. Anal. 36(8)1004-1006 (2004).

[88] C. D. Wagner, W. M. Riggs, L. E. Davis, J. F. Moulder, and G. Muilenberg, *In Handbook of X ray photoelectron Spectrosc, Perkin-Elmer Corporation:* Physical Electronics Division, Eden Prairie, MN, 76, 55344 (1979).

[89] E. Paparazzo, *XPS analysis of iron aluminum oxide systems*, Appl. Surf. Sci. 25(1-2), 1-12(1986).

[90] A. Fujimori, *Mixed valent ground state of CeO_2*, Phys. Rev. B. 28, 2281-2283 (1983).

[91] A. Kotani, H. Mizuta, T. Jo, J. C. Parlebas, *Theory of core photoemission spectra in CeO_2*, Solid state. Commun. 53(9), 805-810(1985).

[92] E. Wuilloud, B. Delley, W. D. Schneider and Y. Baer, *Spectroscopic evidence for localized and extended f-symmetry states in CeO_2,* Phys. Rev. Lett. 53(2), 202-205 (1984).

[93] Y. Linzon, M. Ferrera, L. Razzari, A. Pignolet and R.Morandotti, *Polarization proximity effect in isolator crystal pairs,* Opt. Lett. 33(23), 2871-2873(2008).

[94] T. Körner, A. Heinrich, M. Weckerle, P. Roocks, and B. Strizker, *Integration of magneto-optical active bismuth iron garnet on nongarnet substrates,* J. Appl. Phys.103 (7), 07B337- 3(2008).

[95] G. Y. Zhang, X.Wu and T.C. Chong, *Faraday rotation spectra of bismuth-substituted rare-earth iron garnet crystals in optical communication band*, J. Appl. Phys. 95, 5267-5271(2004).

[96] David R. Lide, ed., *CRC handbook of chemistry and physics*, 90th Edition (Internet Version 2010), CRC Press/Taylor and Francis, Boca Raton, FL.

[97] G.B.Scott and J. L. Page, Phys. Stat. Sol. (b) 79, 203 (1977).

[98] Y. Xu, J.H. Yang and X.J. Zhang, Phys. Rev. B 50, 13428 (1994).

[99] D. Weller, W. Reim and P. Schrijner, IEEEE Trans. Magn. 24, 2554 (1988).

[100] B. M. Holmes and D. C. Hutchings, *Demonstration of quasi-phase-matched nonreciprocal polarization rotation in III-V semiconductor waveguides incorporating magneto-optic upper claddings*, Appl. Phys. Lett. 88, 061116-3 (2006).

[101] S. Geller, *The statistics of superexchange interaction and ionic distribution in substituted ferrimagnetic rare earth iron garnets*, J. Phys. Chem. Solids. 16, 21 (1960).

[102] Z. Simsa, R. Gerber, T. Reid, R. Tesar, R. Atkinson, and P. Papakonstantinou, *Optical absorption and faraday rotation of barium hexaferrite films prepared by laser ablation deposition*, J. Phys. Chem. Solids. 59(1), 111-119(1998).

[103] O. Heczko, R. Gerber and Z. Simsa, *Structural, magnetic and magnetooptical properties of $SrFe_{12-x}Al_xO_{19}$ hexa ferrite thin films prepared by laser ablation deposition,* Thin solid films. 358(1-2), 206-214(2000).

[104] S. A. Oliver, M. L. Chen, I. Kozulin, S. D. Yoon, X. Zuo and C. Vittoria, *Growth and characterization of thick oriented barium hexaferrite films on MgO(111) substrates*, Appl. Phys. Lett. 76, 3612 (2000).

[105] F. Auracher and H. H. Witte, *A new design for an integrated optical isolator*, Opt. Commun. 13, 435-438 (1975).

[106] T. Mizumoto, K. Oochi, T. Harada and Y. Naito, *Measurement of optical nonreciprocal phase shift in a Bi-substituted $Gd_3Fe_5O_{12}$ film and application to waveguide-type optical circulator*, J. Lightwave Technol. LT-4(3), 347-352 (1986).

[107] J. Fujita, M. Levy, R. M. Osgood Jr., L. Wilkens and H. Dotsch, *Waveguide optical isolator based on Mach-Zehnder interferometer*, Appl. Phys. Lett. 76(16), 2158-2160 (2000).

[108] H. Dötsch, N. Bahlmann, O. Zhuromskyy, M. Hammer, L. Wilkens, R. Gerhardt, P. Hertel, *Application of magneto-optical waveguides in integrated optics: review*, J. Opt. Soc. Am. B 22, 240-253 (2005).

[109] H. Yokoi, T. Mizumoto, N. Shinjo, N. Futakuchi and Y. Nakano, *Demonstration of an optical isolator, with a semiconductor guiding layer that was obtained by use of a nonreciprocal phase shift*, Appl. Opt. 39(33), 6158-6164 (2000).